GEOMAGNETIC INFLUENCES ON THERMOSPHERIC WINDS OBSERVED IN THE AURORAL ZONE

A

DISSERTATION

Presented to the Faculty of the

University of Alaska in Partial Fulfillment

of the Requirements

for the Degree of

DOCTOR OF PHILOSOPHY

By

Donald Douglas James Herbert Wallis B.Sc., M.Sc.

Fairbanks, Alaska

May 1974

GEOMAGNETIC INFLUENCES ON THERMOSPHERIC WINDS

OBSERVED IN THE AURORAL ZONE

RECOMMENDED:

Gerald J. Romick
G. J. Romick

David W. Swift
D. W. Swift

T. Neil Davis
T. N. Davis

C. D. Anger
C. Anger

APPROVED:

Keith B Mather by PMD
Director, Geophysical Institute

May 6, 1979
Date

C Dae
Vice President for Research

10 May 74
Date

ABSTRACT

A large body of observations of the wind field in the high-latitude thermosphere (140 to 350 km) is examined to characterize the winds and to determine their probable source. Theories and existing models of these winds are first reviewed. The morphologies of auroral particle precipitation, electric fields, and current systems are discussed to elucidate the effects of these factors upon the wind field. Existing models suggest that the effects of auroral electric fields and heating can be separated in a geomagnetic coordinate frame. It is shown, in this study, that the mean temporal dependence of the (geomagnetic) meridional component is similar to that predicted by tidal models except the magnitudes of the observed winds are smaller than predicted (observed peak speeds - 150 m sec^{-1}). Deviations (up to 200 m sec^{-1}) of the observed meridional winds from this mean behavior are probably caused by heating of the thermosphere by Joule dissipation in the auroral electrojets. Zonal winds are shown to be principally driven by collisions of the neutrals with ions drifting under the action of the auroral zone electric field. Zonal speeds from 200 to 400 m sec^{-1} are typical. The observed zonal winds are correlated with the direction of the auroral electric fields as inferred from magnetometer records. The response time of the observed winds to changes in direction of the electric field (northward to southward) is found to be $\simeq$ 1½ hours. Tidal winds are of secondary importance for the zonal component (peak speeds $\simeq$ 150 m sec^{-1}). Electric fields and Joule dissipation in the high-latitude thermosphere are concluded to be responsible for the principal observed characteristics of auroral-zone thermospheric winds.

ACKNOWLEDGEMENTS

This study has been made possible by the co-operation of other investigators who have kindly provided their unpublished data. Most especially, I would like to thank Drs. A. Nagy, P. Hays, and J. Meriwether of the University of Michigan for permission to make use of their interferometric observations. I would also like to thank Dr. J. Bedinger for providing two unpublished TMA wind profiles, which together with his published profiles have contributed substantially to the understanding of the wind field.

I am deeply indebted to Dr. G. J. Romick, committee chairman, for his continued support, inspiring insight, and untiring leadership throughout the course of this work. The manifold resources of the Geophysical Institute have contributed materially to this study and speeded its completion. Stimulating and informative discussions with Drs. C. Deehr, and V. Degen and with Mssrs. T. Hallinan, B. Watkins and A. E. Belon are gratefully appreciated.

The efficiency, accuracy, and cheerfulness of Mrs. Genevieve Edsall, who completed most of the figures, some typing, and much of the proof reading, is gratefully appreciated. Helpful suggestions concerning the manuscript have been made by Dr. D. R. Packer as well as members of the advisory committee: these suggestions were greatly appreciated.

Funding of this research was provided by the State of Alaska, and National Science foundation grants: GA-31876 and 6A-32119. Some of the barium release data used in this study was acquired under Air Force Contract F 30602-C-0063 and Defense Atomic Support Agency Contract DASA 01-69-C-0047.

The author would like to express his thanks to the people of the United States and the State of Alaska for allowing him to carry out his studies at the Geophysical Institute while holding a student visa.

TABLE OF CONTENTS

	Page
ABSTRACT	iii
ACKNOWLEDGEMENTS	iv
TABLE OF CONTENTS	vi
LIST OF ILLUSTRATIONS	viii
LIST OF TABLES	xv
CHAPTER 1 NEUTRAL WIND IN THE THERMOSPHERE	1
1.3 INTRODUCTION	1
1.2 HIGH-LATITUDE THERMOSPHERIC WINDS	4
1.3 FORMAT OF THIS STUDY	7
1.4 CONVENTIONS USED IN THIS STUDY	9
CHAPTER 2 REVIEW OF THE EQUATIONS OF MOTION AND THE FACTORS WHICH GOVERN THE WIND FIELD IN THE THERMOSPHERE	11
2.1 THE EQUATION OF MOTION FOR THE NEUTRAL THERMOSPHERE	12
The Inertial Term	13
The Coriolis Term	14
The Pressure-Gradient Term	14
The Viscous-Drag Term	15
The Ion-Drag Term	15
Other Equations of Importance for Thermospheric Winds	20
2.2 COMPARISON OF THE MAGNITUDE OF THE TERMS IN THE EQUATION OF MOTION	20
2.3 RESPONSE OF THE THERMOSPHERE TO A HEAT SOURCE	25
2.4 RESPONSE OF THE NEUTRAL THERMOSPHERE TO CROSSED ELECTRIC AND MAGNETIC FIELDS	27
2.5 MORPHOLOGY AND EFFECTS OF AURORAL PARTICLE PRECIPITATION	30
2.6 MORPHOLOGY OF AURORAL ELECTRIC FIELDS	40
2.7 MORPHOLOGY OF HIGH-LATITUDE CURRENTS	47
CHAPTER 3 MODELS OF THERMOSPHERIC WINDS	60
3.1 TIDAL WIND MODELS	60
Challinor's Model	61
Kohl's Model	62
Vest's Model	62
3.2 COMPARISON OF TIDAL WIND MODELS WITH OBSERVATIONS	65
Winds Deduced from the S_q Magnetic variation	65
Low- and Middle-Latitude Winds Deduced from Trail Releases	68
3.3 MODELS OF THE HIGH-LATITUDE WIND FIELD PERTURBATION DUE TO ION-DRAG	69
Fedder and Banks' Model of Ion-Drag Winds	70
Heaps' Model of Ion-Drag Winds	73

		Page
3.4	MODELS OF THERMOSPHERIC WINDS GENERATED BY AURORAL HEATING	77
	Vest's Model of Meridional Winds	77
	Heaps' Model of Meridional Wind Perturbations	79
3.5	SUMMARY OF THERMOSPHERIC WIND MODELS	83
CHAPTER 4	OBSERVATIONS OF THE MERIDIONAL WIND COMPONENT	86
4.1	METHODS AND ERRORS OF OBSERVATION	87
4.2	MEAN TEMPORAL BEHAVIOR OF MERIDIONAL WINDS	88
4.3	CORRELATION OF MERIDIONAL WINDS WITH VARIOUS INDICES	101
4.4	DEVIATIONS OF THE MERIDIONAL WINDS FROM THEIR MEAN BEHAVIOR	105
4.5	THE SOURCES OF MERIDIONAL WINDS	114
CHAPTER 5	OBSERVATIONS OF THE ZONAL WIND COMPONENT	119
5.1	METHODS AND ERRORS OF OBSERVATION	119
5.2	OBSERVATIONS OF ZONAL THERMOSPHERIC WINDS FROM BARIUM RELEASES	122
5.3	OBSERVATIONS OF ZONAL WINDS BY 6300A INTERFEROMETRY	141
5.4	TRAIL RELEASE WIND OBSERVATIONS AT FORT CHURCHILL, CANADA	163
CHAPTER 6	CONCLUSIONS	178
APPENDIX A	LIST OF SYMBOLS	188
APPENDIX B	APPROXIMATE LOCATIONS OF STATIONS MENTIONED IN THIS STUDY	192
APPENDIX C	INTERFEROMETER WIND MEASUREMENTS	193
APPENDIX D	RELEASE TECHNIQUES	202
APPENDIX E	TRIANGULATION ERRORS	208
REFERENCES		218

LIST OF ILLUSTRATIONS

Page

Figure 2.1 The configuration of the auroral oval as a function of magnetic latitude and corrected geomagnetic time for various levels of geomagnetic activity (Q index). Compiled from the figures of Whalen (1970). 32

Figure 2.2 Idealized pattern of auroral and magnetic disturbance. After Heppner (1954). 34

Figure 2.3 Observed relationship between precipitating protons and electrons derived from ground based optical and satellite particle measurements in the evening auroral oval. After Romick and Sharp (1967). 34

Figure 2.4 Measured ion-drift velocities from barium releases in a geomagnetic latitude-magnetic time coordinate frame. Vectors are drawn with base at the release point and are measured positive through east from north. Note that the magnitude scale changes at 53° latitude for release. Numbers refer to table in Davis and Wallis (1972). 41

Figure 2.5 Configuration of the auroral oval and polar cap electric fields and the local time-latitude variation of the Harang discontinuity (dashed line A-B) based upon barium releases and magnetometer data. After Heppner (1972b). 44

Figure 2.6 Ion-drift vectors obtained in a 24 hour period by the Chatinika, Alaska, incoherent scatter radar beginning 1930 LT 10 February 1972, at 220 ± 30 km, in geomagnetic azimuth and local time. From Doupnik et al. (1972). 48

Figure 2.7 A configuration of the auroral electrojets. After Sugiura and Heppner (1965). 49

Figure 2.8 Altitude dependence of Joule dissipation of a model electrojet (dashed curve) and the average rate at which kinetic energy must be supplied to the thermosphere to produce a 100 m/sec wind (solid curve). See text for details of the parameters. 56

Figure 3.1 Model tidal wind field at 250 km. After Challinor (1970a). 63

Figure 3.2 Model tidal wind field at 400 km. After Kohl (1970). 63

Page

Figure 3.3 Plots of tidal winds at 140 km. 180 km, and 300 km altitudes as a function of latitude and local time (a) without auroral heating and (b) with auroral heating. After Vest (1973). 64

Figure 3.4 The dynamo region wind field deduced from the magnetic S_q variation. After Kato (1956). 67

Figure 3.5 Theoretical ion drag winds as a function of height for (a) 1 hour (b) 2 hours (c) 3 hours and (d) 6 hours after turning on of an electric field of 40 mv/m. After Fedder and Banks (1972). 72

Figure 3.6 Heaps' (1972) model of ion-drag winds at 18 hours magnetic time for 0 and 250 km distance north or south of the assumed electric field distribution. U_{MAX} is the peak wind speed. 75

Figure 3.7 Heaps' (1972) model of ion-drag winds at 23 hours magnetic time for four distances north or south of the center of the assumed electric field distribution: (a) 0 km, (b) 100 km, (c) 250 km, and (d) 500 km. 76

Figure 3.8 Meridional, zonal and vertical winds and the temperature/pressure perturbations at 23 hours magnetic time predicted by Heaps (1972) for auroral heating. The ordinate is the distance from the center of the assumed electric field distribution. 81

Figure 3.9 Combined heating and ion-drag wind field at 23 hours magnetic time. After Heaps (1972). 82

Figure 4.1a Observed magnitudes of the meridional wind component obtained at Ester Dome Observatory by 6300A interferometry. The curve is the tidal component predicted by Challinor (1970a) with amplitude halved. Values of the K_p, D_{st} (provisional), and K (College) indices are given. 89

Figure 4.1b Observed magnitudes of the meridional wind component obtained at Ester Dome Observatory by 6300A interferometry. The curve is the tidal component predicted by Challinor (1970a) with amplitude halved. Values of the K_p, D_{st} (provisional), and K (College) indices are given. 90

Figure 4.1c Observed magnitudes of the meridional wind component obtained at Ester Dome Observatory by 6300A interferometry. The curve is the tidal component predicted by Challinor (1970a) with amplitude halved. Values of the K_p, D_{st} (provisional), and K (College) indices are given. 91

Figure 4.1d Observed magnitudes of the meridional wind component obtained at Ester Dome Observatory by 6300A interferometry. The curve is the tidal component predicted by Challinor (1970a) with amplitude halved. Values of the K_p, D_{st} (provisional), and K (College) indices are given. 92

Figure 4.1e Observed magnitudes of the meridional wind component obtained at Ester Dome Observatory by 6300A interferometry. The curve is the tidal component predicted by Challinor (1970a) with amplitude halved. Values of the K_p, D_{st} (provisional), and K (College) indices are given. 93

Figure 4.2 Zonal and meridional components of Challinor's tidal model in a geomagnetic frame for (a) College and (b) Kiruna. 94

Figure 4.3 Zonal and meridional (geomagnetic) components of the tidal wind field predicted by Vest (1973) without auroral heating for (a) College and (b) Kiruna. The solid, dashed and dotted curves represent the components at 300, 180 and 140km, respectively. 96

Figure 4.4 Mean and standard deviation of the meridional wind component observations at Ester Dome Observatory as a function of local time. The dashed curve is Challinor's meridional component with amplitude halved. 97

Figure 4.5 Meridional wind components derived from the motions of several barium releases from Esrange and Andenes. The curve is Challinor's predicted meridional component of the tidal wind field with amplitude halved. 98

Figure 4.6 (a) The latitude-local time distribution of aurora during the night of February 17, 1972(UT). (b) Observed meridional wind component with curve representing the modified tidal model. (c) The magnitude of the H component magnetic perturbation measured at Barrow, Fort Yukon, Poker Flat and Anchorage. 106

Figure 4.7 (a) The latitude-local time distribution of aurora during the night of February 18, 1972 (UT). (b) Observed meridional wind component with curve representing the modified tidal model. (c) The magnitude of the H component magnetic perturbation measured at Barrow, Fort Yukon, Poker Flat and Anchorage. 107

Figure 4.8 (a) The latitude-local time distribution of aurora during the night of March 7, 1972, (UT). (b) Observed meridional wind component with curve representing the modified tidal model. (c) The magnitude of

Page

The H component magnetic perturbation measured at Barrow, Fort Yukon, Poker Flat, and Anchorage. 108

Figure 4.9 (a) The latitude-local time distribution of aurora during the night of April 1, 1972 (UT). (b) Observed meridional wind component with curve representing the modified tidal model. (c) the magnitude of the H component magnetic perturbation measured at Barrow, Fort Yukon, Poker Flat, and Anchorage. 109

Figure 4.10 Polar cap neutral and ion motions reported by Meriwether et al. (1973) and the predicted tidal winds of Challinor (1970a). Geographic coordinates are used. 117

Figure 5.1 Distribution of observed barium neutral cloud velocities (•) and the barium ion cloud velocities (end of line connected to dot) for the releases listed in Table 5.1 in a geomagnetic coordinate frame. 125

Figure 5.2 Distribution of the velocity difference vector $(\vec{V}_I - \vec{U}_I)$ for the barium releases listed in Table 5.1 in a geomagnetic frame. 127

Figure 5.3 Distribution of the velocity difference vector $(\vec{V}_I - \vec{U}_I)$ for the barium releases listed in Table 5.1 in a frame aligned with the statistical orientation of auroral arcs. 128

Figure 5.4 Histogram of the velocity difference $|\vec{V}_I - \vec{U}_I|$ for the barium releases listed in Table 5.1. 130

Figure 5.5 Plot of barium neutral cloud zonal speeds against the two hour average of the ΔX magnetic perturbation. From Rees (1971). 132

Figure 5.6 Ion-drift speed versus the recorded magnetic perturbation $\sqrt{(\Delta X)^2 + (\Delta Y)^2}$ at the launch site and time of launch for the barium releases listed in Table 5.1. The straight lines indicate the values of the effective transverse conductivity Σ_t which would give the measured magnetic perturbation when an infinite plane current is tangent to the dynamo layer at the station and induced ground currents are not present. 134

Figure 5.7 Plot of the observed (geomagnetic) zonal speeds of the barium clouds listed in Table 5.1 against the 1 1/2 and 2 hour averages of the ΔH magnetic perturbation measured at the launch site. The Alaska releases are circled. The dashed line shows the mean relation-

Page

ship between the average magnetic perturbations and the zonal speeds of the Alaskan releases. The solid line indicates the relationship found by Rees (1971). 135

Figure 5.8a Observed magnitudes of the zonal wind component obtained at Ester Dome Observatory by 6300A interferometry with the College ΔH magnetic perturbations. 142

Figure 5.8b Observed magnitudes of the zonal wind component obtained at Ester Dome Observatory by 6300A interferometry with the College ΔH magnetic perturbations. 143

Figure 5.8c Observed magnitudes of the zonal wind component obtained at Ester Dome Observatory by 6300A interferometry with the College magnetic perturbation. 144

Figure 5.8d Observed magnitudes of the zonal wind component obtained at Ester Dome Observatory by 6300A interferometry with the College magnetic perturbation. 145

Figure 5.8e Observed magnitudes of the zonal wind component obtained at Ester Dome Observatory by 6300A interferometry with the College magnetic perturbation. 146

Figure 5.9 Mean and standard deviation of College 6300A interferometer measurements of the zonal winds. Dashed curve is Challinor's (1970a) predicted zonal component with amplitude halved. 151

Figure 5.10 Computed ion-drag winds obtained from the mean observed winds and Challinor's tidal model. The light curve represents the ion-drag winds computed using Challinor's model. The heavy curve results from using Challinor's model with amplitude halved. See text for details. 154

Figure 5.11a Computed zonal ion-drag winds. 155

Figure 5.11b Computed zonal ion-drag winds. 156

Figure 5.11c Computed zonal ion-drag winds. 157

Figure 5.11d Computed zonal ion-drag winds. 158

Figure 5.11e Computed zonal ion-drag winds. 159

Figure 5.12 Mean and standard deviation of the observed zonal winds at Ester Dome Observatory by the 6300A interferometer

Page

ordered with respect to the beginning of the first negative bay recorded by the College magnetometer. 161

Figure 5.13 Mean and standard deviation of the computed ion-drag winds ordered with respect to the beginning of the first negative bay recorded on the College magnetometer. 162

Figure 5.14 Vector neutral wind profile observed above Fort Churchill, Canada, from a TMA release at 1922 CST 15 September 1966, showing (a) the geographic direction of motion as a function of altitude, and (b) the wind speed as a function of altitude. Crosses (+) are theoretical speeds computed by Fedder and Banks (1972) normalized at 155 km. Dots are theoretical speeds from Heaps (1972) normalized at 150 km. 164

Figure 5.15 Vector neutral wind profile observed above Fort Churchill, Canada, from a TMA release at 2200 CST 21 May 1963. Refer to Figure 5.14 for other details. 165

Figure 5.16 Vector neutral wind profile observed above Fort Churchill, Canada, from a TMA release at 0131 CST 22 May 1963. Refer to Figure 5.14 for other details. 166

Figure 5.17 Vector neutral wind profile observed above Fort Churchill, Canada, form a TMA release at 1740 CST 21 February 1965. Refer to Figure 5.14 for other details. 167

Figure 5.18 Vector neutral wind profile observed above Fort Churchill, Canada, from a TMA release at 1470 CST 27 February 1965. Refer to Figure 5.14 for other details. 168

Figure 5.19 Vector neutral wind profile observed above Fort Churchill, Canada, from a TMA release at 1935 CST 13 September 1966. Refer to Figure 5.14 for other details. 169

Figure 5.20 Vector neutral wind profile observed above Fort Churchill, Canada, from a TMA release at 0000CST 1 November 1964. Refer to Figure 5.14 for other details. 170

Figure C.1 Theoretical profiles of 6300A emission (solid curve) and $O(^1D)$ excitation (crosses). After Rees (1970). 197

Figure D.1 Barium releases Fir and Hemlock. 205

Figure E.1 Typical triangulation situation for a finite spherical release. The release need not necessarily be in the vertical plane of the triangulation stations. 211

Page

Figure E.2 Schematic temporal development of an initially spherical barium neutral cloud to an ellipsoidal shape by a wind shear. The spherical cloud (a) is acted upon by the sheared wind field (b) to produce the ellipsoidal cloud (c). As time progresses the ellipsoidal cloud becomes more elongated. 214

Figure E.3 Neutral barium cloud at late time illustrating exceptional shear. Release is the same as shown in the upper portion of Figure D.1. 216

LIST OF TABLES

		Page
Table 2.1	Thermospheric parameters as a function of altitude	21
Table 2.2	Magnitudes of the force terms in the neutral equation of motion	24
Table 2.3	Altitude dependence of the Pedersen conductivity and Joule dissipation of the Pedersen current when the electric field has a value of 20 mv/m	55
Table 3.1	Summary of Tidal and High-Latitude Wind Models	84
Table 4.1a	The number of three-hour intervals in which the net deviation of the meridional winds observed at Ester Dome Observatory were in excess of, or slower than, or approximately equal to the modified tidal model (Challinor, 1970a, with the amplitude halved) versus the change in K_p from the preceding interval	104
Table 4.1b	The number of three-hour intervals in which the net deviation of the meridional winds observed at Ester Dome Observatory were in excess of, or slower than, or approximately equal to the modified tidal model (Challinor, 1970a, with the amplitude halved) versus the change in College K index from the preceding interval	104
Table 5.1	Ion and neutral cloud velocities from a number of barium releases	123
Table 5.2	Neutral barium cloud velocities from releases made simultaneously from two launch sites in Alaska	139
Table 6.1	Comparison of wind observations and models	179
Table 6.2	Principal results of this study	183
Appendix A	List of symbols	188
Appendix B	Approximate locations of stations mentioned in this study	192

CHAPTER 1

NEUTRAL WINDS IN THE THERMOSPHERE

1.1 INTRODUCTION

The development of rockets and satellites during the last two decades has made possible investigations of the constituents and dynamics of the thermosphere. The thermosphere is that region of the earth's atmosphere, above the mesopause (approximate altitude 85 km), in which temperature increases monotonically with increasing height. Other properties (e.g., density and mean molecular weight) vary markedly with altitude above the mesopause. Present-day models of the properties of the thermosphere are based primarily on satellite drag and mass spectrometric measurements. Measurements of the motions of the neutral (electrically uncharged) gases are made primarily by releasing chemical contaminants from rockets. Bulk motions of these neutral gases, when they take place in a region larger than one atmospheric scale height, are considered to be a wind for the purposes of this study. The winds of the thermosphere have considerable consequences for the ionization present at these altitudes as well as perturbing the orbits of artificial satellites.

It is now known that the global dynamics of the thermosphere are controlled by heating resulting from the absorption of solar extreme ultra-violet (EUV) radiation, 40-1000A, in the daytime and cooling by conduction and radiation at night. Density and pressure perturbations, resulting from the heating and cooling, drive horizontal winds. Several models (Challinor, 1970a; Kohl, 1970; Vest, 1973) of these winds at different altitudes have been published in the literature and predict low- and middle-latitude thermospheric winds with fair accuracy when

compared with observations. It is the purpose of this study to investigate the winds at high latitudes and to effect a comparison between theory and observations.

The distribution of ionization can be greatly altered by winds, which are in turn affected by the redistributed ionization (Challinor, 1970b; Rishbeth, 1972). The configuration of the terrestrial magnetic field is such that poleward winds drive ionization downward where recombination proceeds more rapidly, and equatorward winds drive ionization upward, where losses through recombination are reduced. The electromotive force and the resulting charge separation, induced by the winds, drives currents in the dynamo region (90-130 km) which are observed on the earth's surface as the solar quiet (S_q) magnetic variation. In these processes, the ionization acts as a source of friction slowing the movement of the neutral thermosphere.

The release technique for measuring thermospheric winds was first suggested by Bates (1950) as a means of studying the photochemistry of atmospheric sodium. The motions of the first sodium releases (Edwards et al., 1955; Bedinger et al., 1957) were readily recognized as wind effects. Subsequent experimenters (Manring et al., 1959; Groves, 1960; Jarrett et al., 1963) developed analysis techniques and began the first extensive investigations of thermospheric winds. Ragsdale and Wasko (1963) produced the first seasonal maps of the zonal and meridional wind components in the 80 to 400 km height range between 30° and 40°N using data from acoustic grenades, sodium trails, chaff releases, meteor trails and radio fading measurements. Kockanski (1964, 1966) analysed some 54 sodium and trimethyl aluminum (TMA) releases, some of which yielded data up to altitudes of

170 km, and noted the presence of periodic variations in the wind speed profile as a function of altitude. These oscillations were identified as effects of internal atmospheric gravity waves (see Hines, 1960). Since the mid 1960's many papers describing the results of low- and middle-latitude releases have been published. Some of these are briefly reviewed in Chapter 3 as they provide a test of the model calculations of the thermospheric winds based upon the pressure distribution generated by solar heating.

Although release techniques have received the greatest use in measuring neutral motions, perturbations of satellite orbits have also been related to thermospheric winds (King-Hele, 1964). The component of the wind perpendicular to the orbital plane of the satellite causes acceleration of the satellite perpendicular to its motion. From studies of these orbital perturbations, it has been found that the low- and middle-latitude thermosphere has a net eastward motion with respect to the earth, which has been termed super-rotation.

Thermospheric winds are of interest for many reasons not only because of their influence on satellite orbits and the need for predicting the changes in the ionized layers and associated high-frequency radio propagation conditions. Knowledge of the dynamics and energetics of the earth's upper atmosphere is, in part, directly revealed by wind measurements. At high latitudes, auroral particle precipitation produces substantial ionization in the nighttime thermosphere and auroral electric fields can, in theory, together produce marked differences in the wind field from that observed at low and middle latitudes. However, little is known of the characteristics of the winds at high latitudes.

1.2 HIGH-LATITUDE THERMOSPHERIC WINDS

A number of sodium and TMA releases were made at high latitudes prior to 1965, but the small number of releases and anomalous speeds discouraged attempts to interpret the data. The introduction of the barium release technique by Lust and coworkers (Foppl et al., 1965) provoked strong interest in high-latitude thermospheric winds. The barium technique provides a means of measuring ionospheric electric fields. The discovery of large electric fields in the auroral-zone ionosphere stimulated much interest and consequently a large number of releases have been made in this region. In order to accurately interpret barium ion motions in terms of electric fields it is necessary that the neutral wind be measured as well: the advantage of the barium technique is that neutral winds can be simultaneously measured.

The first examinations of this large body of neutral wind data were published just recently. Rees (1971) examined the motions of several barium releases and concluded that the zonal (east-west) wind was directly proportional to the magnitude of the north-south component of the magnetic perturbation averaged over a two hour interval. (This analysis will be discussed in the light of more recent data in Chapter 5.) Meriwether et al. (1971) found evidence for increasing neutral wind speeds as a function of altitude in polar-cap latitudes. The general direction of neutral motion in the polar-cap was reported to be from day to night. In the auroral zone, Meriwether et al. reported westward motions in the evening. Romick and Davis (1971) noted a tendency for increasing westward zonal motion with increasing positive magnetic activity. They also examined one release which showed evidence of remarkable shear in the

horizontal wind speed with altitude. Romick and Davis suggest that near 170 km "...geomagnetic activity can exert a large influence on the direction and magnitude of neutral atmospheric motions...in the auroral zone."

Stoffregen et al. (1971) examined the motions of several barium clouds in relation to models of thermospheric winds predicted from the observed global pressure distribution generated by EUV absorption. Large discrepancies from predicted winds were found between the altitudes of 150 and 250 km. Stoffregen (1972) advanced an hypothesis, based upon an auroral-zone pressure bulge caused by auroral heating, to explain these discrepancies. Recent satellite measurements (DeVries, 1972; Taeusch et al., 1971) confirm the presence of significant variations in thermospheric densities at polar and auroral latitudes in response to geomagnetic activity.

The pressure-gradient force associated with these density variations, however, is not the only force which can drive neutral thermospheric motions. Rees (1971) suggested from examination of auroral-zone barium cloud data that the neutral thermosphere may be driven by collisions with ions drifting under the influence of the ionospheric electric field. This result has long been predicted theoretically (Piddington, 1954). Fedder and Banks (1972) have investigated this mechanism and have found it to be of theoretical importance in the polar-cap regions where a dawn-to-dusk electric field is known to exist. Apparently, electric fields of magnitude 10-50 mv m^{-1} can accelerate the neutral thermosphere if present for an hour or more. Electric fields of these magnitudes are known to be present in the auroral-zone thermosphere. Meriwether et al.

(1972) have demonstrated that, at least in the evening hours, auroral-zone winds are dominated by collisions with ions drifting under the influence of crossed electric and magnetic fields. This process is usually referred to as ion-drag.

Recently a number of theoretical papers concerning Joule heating of the auroral thermosphere have been presented (Heaps, 1972: Richmond, 1973: and Wu et al., 1973); these discuss the effects of this heating upon thermospheric motions. An additional thesis (Vest, 1973) considers thermospheric heating by primary auroral particles and the effects of this heating source on the winds. These papers and Fedder and Banks' (1972) work on ion-drag will be reviewed in Chapter 3. All of these papers suggest that significant alteration of the thermospheric wind field, at least in high latitudes, can occur in response to auroral- or geomagnetic-activity.

It is of interest, and the basic subject of this study, to examine high-latitude thermospheric winds and to determine their relationship, if any, to geomagnetic activity and auroral-zone electric fields. A composite of the available experimental data is used for this examination. These data include observations of artificial releases of sodium, TMA, and barium, both as points and as trails, as well as interferometric observations of the Doppler shift of atmospheric emissions. No systematic investigation of these data in relationship to any existing model has yet been made. The primary aim of this study is to characterize the motions of the high-latitude thermosphere and to determine, if possible, the processes responsible for these motions.

1.3 FORMAT OF THIS STUDY

The availability of a large body of wind observations and several published models of the response of the high-latitude thermosphere to auroral heating and auroral-zone electric fields suggests that theory and observations may be profitably compared. As most of the available observations were made at altitudes above 150 km, this study concentrates on the altitude range 150 to 350 km. This upper altitude restriction is again imposed by the measurement techniques. Restriction to high-latitude observations is made so that the effects of geomagnetic activity can be most easily detected. The polar-cap region will only be briefly considered because the small number of observations there do not permit a complete investigation of the winds.

Prior to examining the wind observations and comparing these observations to models, a brief discussion of the equations governing neutral motions of the thermosphere and the energy sources for these motions is presented in Chapter 2. The response of a partially ionized thermosphere to a heat source and to crossed electric and magnetic fields and to a heat source is examined. Reviews of auroral particle, electric field, and auroral electrojet current morphologies are also presented in relation to their effects on the thermosphere and neutral winds. Models of thermospheric winds are reviewed in Chapter 3. First, the model of Challinor (1968, 1969, 1970a) for the diurnal tidal wind field is discussed. This discussion is supplemented by Vest's (1973) calculations for three different altitudes. These models are compared with the wind field deduced by Kato (1956) from the S_q variation and with Bedinger's (1970) wind observations at middle latitudes. Two models for ion-drag acceleration of the neutral

thermosphere are examined next: Fedder and Banks' (1972) model which is local in nature, and Heaps' (1972) model which includes a specified global model of the electric field and treats the time-dependent problem. Finally, Vest's (1973) and Heaps' (1972) models of the thermospheric response to auroral heating are reviewed.

Consideration of these models suggests that the effect of auroral heating is primarily meridional in nature, while the ion-drag mechanism is predicted to produce zonal winds. Accordingly, analysis of high-latitude wind observations is divided into these two components. In Chapter 4, the meridional component is examined. Data are taken from 6300A Doppler shift observations primarily, and secondarily from a number of barium releases. These data are compared to the models of the tidal and auroral heating winds and also to a number of geophysical parameters with which the meridional wind might be expected to correlate.

Three different bodies of data are examined to determine the dependence of the zonal winds upon geomagnetic activity in Chapter 5. Barium cloud motions are studied to examine the importance of ion-drag as a means of acceleration of the neutral thermosphere. Interferometric Doppler shift observations of auroral 6300A emission are then examined. These Doppler shift wind measurements are related to the auroral-zone electric field through their temporal dependencies. Finally, trail release data are compared to Fedder and Banks' and Heaps' models.

Complete discussions of the physical basis of the barium cloud and interferometric Doppler wind observations are included in appendices. The appendices also include discussions of the errors of these measurements.

Other appendices provide a list of the symbols used consistently throughout the text and a list of the geographic and geomagnetic coordinates of the locations used in this study.

Chapter 6 presents a summary of the major features of the observed high-latitude neutral thermospheric wind field. The major driving forces causing these winds are identified and a brief statement is made of the importance of high-latitude processes in driving global thermospheric motions. Also included are specific experiments designed to test areas that are not presently well understood.

1.4 CONVENTIONS USED IN THIS STUDY

Throughout this study, certain conventions are used to eliminate unnecessary and possibly confusing words. These conventions are stated below.

First and most importantly, the upper atmosphere convention for wind direction is used. That is a drawn vector or a direction reference in the text refers to the direction in which air (or other substance) is moving with respect to the frame of reference. Lower atmospheric meteorologists frequently refer to the direction from which the air comes.

Unless a specific reference is made in the text, or noted by subscript in equations, it should be assumed that the horizontal component of a vector is implied. Thus the statement "the vertical gradient of the wind" refers to the vertical derivative of the horizontal wind component(s). In referring to charged particle motion, the subscript $_{\perp}$ meaning perpendicular to the magnetic field is frequently used. Because at the high latitudes relevant to this study the magnetic inclination is greater than 75° the difference between horizontal and perpendicular to the

magnetic field is small, this distinction is not always made. Where this distinction is important, specific mention is made.

Coordinate frames will be adequately explained where they are introduced. In general, wind components are referred to a cartesian frame with x north and y west. Data taken from other authors are converted to this frame when necessary. Universal time (UT) and local standard time (LT) are both used. Appendix B lists the time difference between UT and LT for the stations referred to in this study. Rationalized MKS units are employed throughout the text except for measured values of the magnetic field perturbations which are expressed in gammas. One gamma (γ) is one nTesla.

The observed winds, which are discussed in Chapters 4 and 5, are resolved into zonal (east-west) and meridional (north-south) components effectively in the 1965 Corrected Geomagnetic Coordinate system (Hakura, 1965). In general, references to geomagnetic coordinates should be referred to the 1965 Corrected Geomagnetic Coordinate system. The azimuths of (1965 Corrected) geomagnetic north at College and Kiruna used were 28° and 343°, respectively.

CHAPTER 2

REVIEW OF THE EQUATIONS OF MOTION AND THE FACTORS WHICH GOVERN THE WIND FIELD IN THE THERMOSPHERE

The response of a fluid to perturbing forces is complex and, in general, depends upon the nature of the perturbation. For example, if there is a pressure difference between two regions of a fluid, the fluid responds by moving so as to reduce the pressure difference. The application of heat to a fluid produces density (and pressure) changes according to the equation of state. Uneven heating results in pressure-gradients causing motion of part of the fluid relative to the remainder. When a fluid is composed of two or more constituents, bulk motion of one of the constituents relative to the rest of the fluid is retarded by collisions which transfer momentum from one constituent to the others. This momentum transfer, of course, results in a acceleration of the initially stationary or slower moving component(s) of the fluid.

The thermosphere is a multi-component fluid pervaded by a magnetic field. The magnetic field, through the Lorentz force, modifies the motion of charged particles (electrons and ions) and allows motion of the charged particles relative to the neutral constituents. If there is no electric field the positive ions are constrained by the magnetic field. Thus momentum transfer from neutrals to ions acts to slow the neutrals. This process, known as ion-drag, is a frictional force for neutral motion. The reverse process can also be important. When the horizontal component of the electric field is large (say 50 mv m^{-1}) the charged particle drift speed is large (1 km sec^{-1}) in the direction mutually perpendicular to the magnetic and electric fields. Momentum is then

transferred from the ions to the neutrals causing neutral acceleration.

The properties of the thermosphere vary greatly as a function of altitude. Above approximately 110 km turbulence ceases to be an important process and diffusion becomes dominant. The mean molecular weight of the thermosphere decreases steadily above 110 km. The thermal properties are constantly changing with altitude because the partial fractions of the constituent gases are changing. The thermosphere becomes very close to isothermal above 350-400 km because the mean free paths become large and the thermal conductivity is correspondingly large. The relative density of positive ions to neutrals changes with both altitude and time and at high latitudes can vary abruptly both spatially and temporally.

In this chapter, the equations which govern the motion of the neutral thermospheric constituents are reviewed. The response of the thermosphere to a heat source is discussed and the theoretical response of a partially ionized thermosphere to a horizontal electric field in the presence of a mechanical force is developed. In order to understand their influence upon the high-latitude thermosphere, which is the main topic of this study, a comprehensive review of the energy inputs and morphologies of auroral particle precipitation, ionospheric electric fields and current systems is also presented.

2.1 THE EQUATION OF MOTION FOR THE NEUTRAL THERMOSPHERE

In the altitudes considered in this study, the thermosphere may be regarded as a single fluid subject to the hydrodynamic equation of motion (Rishbeth, 1972):

$$\frac{d\vec{U}}{dt} = -2\vec{\Omega} \times \vec{U} + \vec{g} - \frac{1}{\rho}\nabla P + \frac{\mu}{\rho}\nabla^2 \vec{U} - \nu_{ni}(\vec{U} - \vec{V}) \qquad 2.1$$

where $\vec{U}$ is the neutral (wind) velocity (m sec^{-1}),

$\vec{V}$ is the ion (drift) velocity (m sec^{-1}),

$\vec{g}$ is the gravitational acceleration of the earth (m sec^{-2}),

$\vec{\Omega}$ is the earth's angular velocity (sec^{-1}),

ρ is the neutral density (kgm m^{-3}),

P is the pressure (kgm m^{-1} sec^{-2}),

ν_{ni} is the effective collision frequency for momentum transfer to ions,

and $\frac{\mu}{\rho}$ is the kinematic viscosity (m^2 sec^{-1}).

A short discussion of each of the terms in the equation of motion is in order.

The Inertial Term

The term $d\vec{U}/dt$ can be written as

$$\frac{d\vec{U}}{dt} = \frac{\partial \vec{U}}{\partial t} + (\vec{U} \cdot \nabla)\ \vec{U}.$$

The second term on the right side is known as the nonlinear or advective term. The total derivative, $d\vec{U}/dt$, is the rate of change of the fluid velocity at a point which is moving with the fluid. The partial derivative, $\partial\vec{U}/\partial t$, is the acceleration of the fluid at a point fixed in space. The nonlinear term accounts for momentum transported by the fluid. The nonlinear term has been shown by several authors (Geisler, 1967; and Kohl, 1970, among others) to be an important term for thermospheric motions, however it is frequently ignored as its presence complicates solution of the equation.

The Coriolis Term

The frame from which thermospheric motions are usually viewed rotates with the earth. In order to accurately describe motions in such a frame, the Coriolis acceleration, $-2\vec{\Omega} \times \vec{U}$, must be included in the equation of motion. The Coriolis force acts at right angles to the direction of motion of the fluid and, therefore, does no work, but does act to change the direction of motion of the fluid. The angular speed of the earth's rotation, $\vec{\Omega}$, has magnitude 7.29×10^{-5} sec^{-1} and points upward through the north, geographic, pole.

The Pressure-Gradient Term

If a pressure-gradient exists in a fluid then a force acts upon the fluid causing it to move in a direction opposite to the gradient (or down gradient). This motion tends to result in the removal of the pressure-gradient and, in the absence of other forces, fluid motion is exactly down gradient. However, as soon as the fluid acquires some velocity $\vec{U}$ as a result of the pressure-gradient, the Coriolis force $(-2\vec{\Omega} \times \vec{U})$ causes a component of motion perpendicular to the pressure-gradient. In the lower atmosphere, but high enough that surface friction is unimportant, the ion-drag and viscous forces are negligible so the equation of motion for the horizontal components reduces in equilibrium to

$$-2\vec{\Omega} \times \vec{U} = \frac{-1}{\rho} \nabla P, \qquad 2.2$$

which is called the geostrophic approximation. The Coriolis force balances the pressure-gradient force and the wind vector $\vec{U}$ is perpendicular to both forces. Better approximations to the real wind field

are obtained when the inertial terms are retained. In the thermosphere, the ion-drag and viscous terms dominate the Coriolis term so the geostrophic approximation cannot hold there and the winds are more nearly down gradient.

The Viscous-Drag Term

The viscosity of a fluid acts to remove velocity gradients. In the thermosphere, viscosity becomes increasingly important with altitude as the mean free path of the gas molecules increases. The coefficient of viscosity, μ, depends upon the relative fractions of the atmospheric constituents and is not simply a mass-weighted average. Methods of computing μ are reviewed by Vest (1973). At high altitudes where atomic oxygen is the dominant constituent, the formula

$$\mu = 3.34 \times 10^{-7} \; T^{0.71} \quad \text{Kgm m}^{-1} \text{ sec}^{-1}$$

given by Dalgarno and Smith (1962) may be used. The viscous-drag term is more properly written as $\frac{1}{\rho} \nabla \cdot (\mu \nabla) \vec{U}$, which can be expanded to

$$\frac{1}{\rho} \nabla \cdot (\mu \nabla) \vec{U} = \frac{1}{\rho} \left[\frac{\partial}{\partial x} \left(\mu \frac{\partial}{\partial x} \right) + \frac{\partial}{\partial y} \left(\mu \frac{\partial}{\partial y} \right) + \frac{\partial}{\partial z} \left(\mu \frac{\partial}{\partial z} \right) \right] \vec{U}. \qquad 2.3$$

The horizontal gradients of the coefficient of viscosity are small so that equation 2.3 is rewritten

$$\frac{1}{\rho} \nabla \cdot (\mu \nabla) \vec{U} \simeq \frac{1}{\rho} \left[\mu \nabla^2 \vec{U} + \frac{\partial \mu}{\partial z} \frac{\partial \vec{U}}{\partial z} \right] . \qquad 2.4$$

Many authors drop the second term so that the viscous-drag term is as given in equation 2.1.

The Ion-Drag Term

The ion-drag term $\nu_{ni}(\vec{V} - \vec{U})$ acts to bring the neutral thermospheric motion into correspondence with the ion motion. For small ion

drift speeds, the term is obviously a momentum-loss term for the neutrals. When $\vec{V}_i$ is large, the neutrals are accelerated. Momentum gained or lost by neutrals in ion-neutral collisions must, by Newton's third law, be provided by or taken up by the ions. Thus, there must be a similar term in the equation of ion motion. The ion velocity is governed by the ion equation of motion given by Rishbeth (1972):

$$\frac{d\vec{V}}{dt} = \vec{g} + \frac{\nabla(P_i + P_e)}{Nm_i} - \nu_{in}(\vec{V} - \vec{U}) + \frac{e}{m_i}(\vec{E}' + \vec{V} \times \vec{B}), \qquad 2.5$$

where N is the electron (ion member density) (m^{-3}),

m_i is the ion mass (kgm),

P_i is the ion partial pressure (NkT_i) (kgm m^{-1} sec^{-2}),

P_e is the electron partial pressure (NkT_e) (kgm m^{-1} sec^{-2}),

ν_{in} is the effective collision frequency for momentum transfer to neutrals (sec^{-1}),

$\vec{E}'$ is the electric field strength (V m^{-1}),

$\vec{B}$ is the magnetic induction field (Webers m^{-2}),

k is Boltzmann's constant (1.380 x 10^{-23} Joules $°K^{-1}$),

T_e is the electron temperature (°K),

and T_i is the ion temperature (°K).

Because ν_{in} is large, the Coriolis term ($-2\vec{\Omega} \times \vec{V}$) is normally neglected. The presence of the electron partial pressure in the pressure-gradient term is required because ions and neutrals are bound electrostatically. The final term $e(\vec{E}' + \vec{V} \times \vec{B})/m_i$ is the Lorentz force (per unit mass). An analagous equation applies to the motion of electrons (with e replaced by -e and m_i by m_e). If more than one species of ion is present, equation 2.5 must be written for each species;

however, for the present purpose it is sufficient to assume only one species of ion is present with average properties.

At the altitudes and time scales of interest here, $d\vec{V}/dt$ may be assumed to be zero, as the time required for the ions to attain a steady state drift velocity must be shorter than interval between collisions with neutrals, ν_{in}^{-1}. In applying equation 2.5 one must be careful to use quantities referred to the same frame. When the horizontal component equations of motion (2.5) are solved for charged particle motion in the presence of crossed electric and magnetic fields (pressure-gradients are ignored), it is found that ions (electrons) execute a time-averaged drift motion perpendicular to both fields, which is equal to $\vec{E} \times \vec{B} / B^2$ when collisions are unimportant ($\nu_{in} << \omega_i$). When collisions become important (for ions below approximately 150 km, and for electrons below 90 km) the magnitude of the ion speed decreases and acquires a component in the direction of the electric field. When the ion and electron velocities are different, a net current results. The equations of electron and ion motion can be solved for the conductivity tensor elements which relate the current density $\vec{J}$ to the electric field $\vec{E}'$

$$\vec{J} = \begin{pmatrix} \sigma_1 & \sigma_2 & 0 \\ -\sigma_2 & \sigma_1 & 0 \\ 0 & 0 & \sigma_{\parallel} \end{pmatrix} \vec{E}' , \qquad 2.6$$

where $\vec{E}' = \vec{E} + \vec{U} \times \vec{B}$. The elements $\sigma_{\parallel}$, the parallel conductivity, σ_1, the Pedersen conductivity, and σ_2, the Hall conductivity, are given by

$$\sigma_H = \frac{e}{B}\left(\frac{N_e \omega_e}{\nu_e} + \sum_i \frac{N_i \omega_i}{\nu_i}\right), \qquad 2.7a$$

$$\sigma_1 = \frac{e}{B}\left(\frac{N_e \nu_e \omega_e}{\nu_e^2 + \omega_e^2} + \sum_i \frac{N_i \nu_i \omega_i}{\nu_i^2 + \omega_i^2}\right), \qquad 2.7b$$

and $$\sigma_2 = \frac{e}{B}\left(\frac{N_e \omega_e^2}{\nu_e^2 + \omega_e^2} + \sum_i \frac{N_i \omega_i^2}{\nu_i^2 + \omega_i^2}\right), \qquad 2.7c$$

where $\omega_e = eB/m_e$, $\omega_i = eB/m_i$ are the electron- and ion-gyrofrequencies. The summation is over the various ion species. In deriving these conductivities, the neutral velocity $\vec{U}$ is assumed to be zero.

Consider now the horizontal component equation derived from equation 2.5 for both electrons and ions. In steady-state

$$0 = e N_i (\vec{E}' + \vec{V} \times \vec{B}) - \rho_i \nu_{in} (\vec{V} - \vec{U}) \qquad 2.8a$$

and $$0 = -e N_e (\vec{E}' + \vec{V}_e \times \vec{B}) - \rho_i \nu_{en} (\vec{V}_e - \vec{U}) \qquad 2.8b$$

where ρ_i and ρ_e are the ion- and electron-mass densities and ν_{en} is the effective collision frequency for momentum transfer from electrons. Adding these equations and assuming charge neutrality

$$0 = e N_i(\vec{V} \times \vec{B}) - e N_e(\vec{V}_e \times \vec{B}) - \rho_i \nu_{in}(\vec{V} - \vec{U}) - \rho_e \nu_{en}(\vec{V}_e - \vec{U}). \qquad 2.9$$

Substituting $\vec{J} = e N_i \vec{V} - e N_e \vec{V}_e$ for the current density,

$$0 = \vec{J} \times \vec{B} - \rho_i \nu_{in} (\vec{V} - \vec{U}) - \rho_e \nu_{en} (\vec{V}_e - \vec{U}), \qquad 2.10$$

which can be rearranged into the form

$$\nu_{in} (\vec{V} - \vec{U}) = \frac{\vec{J} \times \vec{B}}{\rho_i} - \frac{\rho_e}{\rho_i} \nu_{en} (\vec{V}_e - \vec{U}). \qquad 2.11$$

Since by Newton's Third Law, $\rho \nu_{ni} = \rho_i \nu_{in}$, the ion-drag term in the neutral equation of motion (equation 2.1) becomes

$$-\nu_{ni}(\vec{U} - \vec{V}) = \frac{\vec{J} \times \vec{B}}{\rho} - \frac{\rho_e}{\rho} \nu_{en}(\vec{V}_e - \vec{U}). \qquad 2.12$$

The last term may be dropped because $\rho_e << \rho$. Thus the neutral equation of motion may be rewritten with the ion-drag term replaced by the Lorentz body force, $\vec{J} \times \vec{B}$. This avoids explicit dependence upon the ion velocity, as $\vec{J}$ can be calculated from equation 2.6. If this is not done the equation of ion motion must be solved in conjunction with the neutral equation of motion. These equations are coupled by the ion-drag term.

The steady-state ion motion in crossed electric and magnetic fields when the neutral velocity is maintained constant is given by

$$V_x = \frac{1}{\nu_{in}^2 + \omega_i^2}(\nu_{in}\omega_i E_x/B - \omega_i^2 E_y/B + \nu_{in}^2 U_x - \nu_{in}\omega_i U_y) \qquad 2.13a$$

$$V_y = \frac{1}{\nu_{in}^2 + \omega_i^2}(\omega_i^2 E_x/B + \nu_{in}\omega_i E_y/B + \nu_{in}\omega_i U_x + \nu_{in}^2 U_y), \qquad 2.13b$$

which is a solution of equation 2.5. Here U_x and U_y are the components of the neutral velocity in a plane normal to the magnetic field which is taken to be in the $-\hat{z}$ direction. V_x and V_y are the ion velocity components in the same plane. In the F-region where the ions are gyrofree, $\omega_i^2 > \omega_i\nu_{in} > \nu_{in}^2$ so that the dominant terms for the x-component of the ion motion are the y-components of the electric field and neutral velocity. Similarly, the dominant terms for the y-component of ion motion are the x-components of the electric field and neutral velocity. In the absence of neutral motion, the ion velocity vector makes an angle given by $\tan^{-1}\omega_i/\nu_{in}$ with the direction of the electric field. As the ratio of the collision frequency to the gyrofrequency

increases with decreasing altitude, the angle of the ion motion to the electric field decreases.

Other Equations of Importance for Thermospheric Winds

Numerical calculations of the thermospheric wind field, such as those to be examined in the next chapter, are solutions to the neutral equation of motion. However, there are too many variables; generally the three components of the wind velocity and the temperature and density perturbations. Other relations are used to make solution of the equation of motion possible. The perfect gas law, $P = \rho RT = N_n kT$, where N_n is the neutral number density and k is Boltzmann's constant, relates pressure, density and temperature. The equation of continuity

$$\frac{\partial \rho}{\partial t} + \nabla \cdot (\rho \vec{U}) = 0 \qquad 2.14$$

relates the velocity components and density changes. In reality this is just an expression of mass conservation. Another relation, the equation of total energy or the thermodynamic equation (Schlichting, 1968), is used to relate heating and vertical motions.

2.2 COMPARISON OF THE MAGNITUDE OF THE TERMS IN THE EQUATION OF MOTION

Representative values for the parameters ρ, ν_{in}, ν_{ni}, $|\vec{g}|$, and μ/ρ derived from a model atmosphere are presented in Table 2.1. The CIRA 1965 reference atmosphere, model 5 was chosen as the basis for these parameters. The values of the collision frequencies were calculated according to the formulas of Hanson (1965) assuming a constant electron density profile of 2×10^{11} electrons m^{-3}. The kinematic viscosity (the coefficient of viscosity divided by the density) was calculated according to the formula of Dalgarno and Smith (1962). The conditions

TABLE 2.1

ATMOSPHERIC PARAMETERS AS A FUNCTION OF ALTITUDE

Altitude (km)	Density (kgm m^{-3})	g (m sec^{-2})	ν_{in} (sec^{-1})	ν_{ni} (sec^{-1})	Kinematic viscosity μ/g (m^2 sec^{-1})
120	2.49-8*	9.45	2.8+2	1.00-4	8.68+2
140	4.00-9	9.39	4.8+1	1.02-4	7.88+3
160	1.34-9	9.33	1.7+1	1.05-4	2.74+4
180	5.85-10	9.27	7.9	1.07-4	6.78+4
200	2.90-10	9.22	4.2	1.09-4	1.43+5
250	6.78-11	9.08	1.2	1.15-4	6.44+5
300	2.04-11	8.94	4.0-1	1.21-4	2.18+6
350	7.10-12	8.81	1.5-1	1.25-4	6.32+6
400	2.77-12	8.68	6.5-2	1.28-4	1.62+7

* notation: 2.48-8 = 2.48×10^{-8}

assumed in the calculation of these parameters correspond to moderate auroral disturbance at high latitudes at night. They also correspond approximately to midday thermospheric conditions at middle and low latitudes.

The effective collision frequency for momentum transfer from ions to neutrals, ν_{in}, decreases as altitude increases, while the neutral to ion collision frequency, ν_{ni}, is approximately constant. The kinematic viscosity increases greatly with altitude. It should be noted that the ion density used is smaller than is generally observed under conditions of major auroral activity. Values can be as much as 4 times larger. In contrast, nighttime ion densities at low and middle latitudes may be a factor of 3 smaller. While other parameters upon which ν_{in} depends may vary under the conditions found in the thermosphere, ν_{in} is approximately proportional to the ion density.

Assuming $|\vec{U}| = 100 \text{ sec}^{-1}$ and $|\vec{V}| = 250 \text{ m sec}^{-1}$, in a direction opposite to $\vec{U}$, the magnitudes of the Coriolis and ion-drag terms may be evaluated. To obtain an order of magnitude of the pressure-gradient, the pressure difference at fixed altitude is taken from the CIRA (1965) model atmosphere (model 5 at 00 and 02 hours) and divided by $\frac{\pi}{6}$ R sin 15°, which is a distance corresponding to two hours of time at 65° geographic latitude (R is the radius from the center of the earth). This is a slight overestimate of the pressure-gradient. The viscous accelerations are estimated from the shearing rate of the neutral barium cloud examined by Romick and Davis (1971). The neutral cloud grew in apparent length at a rate of 140 m sec^{-1}. The triangulated heights of the ends of this release differed by approximately 20 km.

Thus, $\partial|\vec{U}_\perp|/\partial z = 7 \times 10^{-3}$ sec^{-1} at 160 km, which is the approximate height of the release. This cloud was highly elongated, so this shear is taken as an upper limit for the vertical gradient of the horizontal velocity. If this shear is assumed to be present at all altitudes (that is, it is not a function of z), then the viscous term for vertical transport of horizontal momentum becomes $(\partial|\vec{U}_\perp|/\rho\partial z)(\partial\mu/\partial z)$. Values for this viscous-drag as well as the Coriolis, ion-drag, and pressure-gradient accelerations are given in Table 2.2. It is apparent that the ion-drag and pressure-gradient terms dominate. Viscosity becomes increasingly important with altitude.

The viscosity term computed for Table 2.2 must be considered as an upper limit because of the large shear used in computing the values. Sustained shears, existing over vertical distances of the order of an atmospheric scale height or more, typically found in the thermosphere, are a factor of 2 smaller. Results supporting this statement are presented in Chapter 5. The viscous accelerations given, however, may be inaccurate (and overestimated) below 200 km because of the approximation used in the calculation of μ. The component calculated for the table (vertical transport of horizontal momentum) is the largest component of viscous-drag.

In contrast to the upper limit calculation for the viscous-drag term, the parameters used in computing the magnitude of the ion-drag term are conservative. In the high-latitude thermosphere, the magnitude of the ion drift vector, $|\vec{V}|$, can easily exceed the 250 m sec^{-1} value used, by more than a factor of five. Coupling with this is the

TABLE 2.2

MAGNITUDES OF THE FORCE TERMS IN THE

NEUTRAL EQUATION OF MOTION

(HORIZONTAL COMPONENT ONLY)

ALTITUDE (km)	CORIOLIS ACCELERATION	PRESSURE-GRADIENT ACCELERATION	ION-DRAG ACCELERATION	VISCOUS-DRAG ACCELERATION
120	7.29 - 3	0	3.50 - 2	1.65 - 5
140	7.29 - 3	3.15 - 3	3.57 - 2	5.21 - 5
160	7.29 - 3	9.46 - 3	3.68 - 2	8.82 - 4
180	7.29 - 3	1.72 - 2	3.75 - 2	1.20 - 3
200	7.29 - 3	2.50 - 2	3.82 - 2	1.51 - 3
250	7.29 - 3	4.21 - 2	4.02 - 2	2.34 - 3
300	7.29 - 3	5.59 - 2	4.24 - 2	4.45 - 3
350	7.29 - 3	5.89 - 2	4.38 - 2	6.32 - 3
400	7.29 - 3	7.80 - 2	4.48 - 2	8.08 - 3

possibility of an increase in ν_{ni} due to an increase in electron density associated with auroral particle precipitation. Under these circumstances, ion-drag acceleration clearly dominates both the Coriolis and pressure-gradient accelerations.

2.3 RESPONSE OF THE THERMOSPHERE TO A HEAT SOURCE

Under normal conditions, the vertical pressure-gradient force is very nearly balanced by gravitational acceleration. This condition, known as hydrostatic equilibrium, is widely used and assumes that no vertical motions are present. Ion motion along the magnetic field due to forces other than ion-neutral collisions is probably small. Thus ion-drag acceleration of vertical neutral motion can be disregarded. The vertical Coriolis acceleration is $-2\ \Omega\ U_y \sin\theta$, where U_y is the zonal wind speed and θ is the geographic colatitude. Numerically, for a 100 m sec^{-1} zonal wind, this Coriolis term is approximately 4×10^{-3} m sec^{-2} at 65° latitude, or much smaller than g.

In reality, hydrostatic equilibrium does not hold in the thermosphere as heat is continually being added by absorption of solar EUV and removed by conduction and radiation. The thermosphere is therefore not in equilibrium at all, but is continually responding to these heat losses and gains. However, the vertical motions required to accommodate this heating and cooling are small, being approximately 3 m sec^{-1} at 300 km and less at lower altitudes. These vertical motions do provide the mass displacements causing thermospheric pressure bulges and horizontal winds.

Considerable heating may be generated in the high-latitude

thermosphere by dissipation of the auroral electrojet, an ionospheric current found at high latitudes in association with the visible aurora which produces perturbations in the geomagnetic field measurable on the surface of the earth. While examination of the auroral electrojet and Joule dissipation is deferred until later in this chapter, the response of the thermosphere to this heating is examined briefly here. Excellent analytic treatments of this problem have been presented by Roble (1969), Roble and Dickenson (1970), Heaps (1972) and Vest (1973).

A small parcel of air when heated expands and rises to a higher altitude. Expansion is accompanied by adiabatic cooling and the parcel comes to rest in equilibrium with its new surroundings. This is possible because the thermospheric temperature gradient is positive. Were this not so, the parcel would always find its temperature greater and its density less than its surroundings. When a sizeable volume of the thermosphere is heated, and increase in pressure occurs at all heights above the heated region because mass has been displaced upward. Above the heating, horizontal pressure-gradients pointing toward the center of the heated region result and drive horizontal winds outward. A net pressure reduction occurs below the altitude of peak heating resulting in inward horizontal winds. The exponential nature of the thermosphere permits the replacement of mass transported away from the heated region at upper levels by large wind speeds (> 100 m sec^{-1}) by vertical mass transport with modest (< 10 m sec^{-1}) speeds. Very modest motions occur at the base of the heated region.

In relation to the latitudinal variations, auroral heating along

the auroral oval may be considered to be approximately uniform. It is expected that vertical motions can occur above auroral forms or the auroral oval and result in meridional winds both poleward and equatorward of the regions of aurora (Heaps, 1972).

2.4 RESPONSE OF THE NEUTRAL THERMOSPHERE TO CROSSED ELECTRIC AND MAGNETIC FIELDS

The general solution of the neutral equation of motion with all terms retained has not yet been found. The usual method of solution is the elimination of some of the terms and the use of numerical integration on a high speed computer. Nevertheless, Piddington (1954) has shown that it is possible to elicit the basic response of the thermosphere analytically when a number of simplifying assumptions are made.

It is assumed that all of the acceleration terms in the equation of motion, except the ion-drag term, can be consolidated into a single mechanical force $\vec{F}$ which is taken to be directed along the positive x-axis. The magnetic field is assumed to be directed along the positive z-axis. The electric field is assumed to be perpendicular to the magnetic field and no motion along the z-axis is permitted. With the neglect of the nonlinear term, the neutral equation of motion can be written,

$$\rho \frac{\partial \vec{U}}{\partial t} = \vec{J} \times \vec{B} + \vec{F} \qquad 2.15$$

where the current density $\vec{J}$ is given by

$$\vec{J} = \sigma_1 \vec{E}' + \sigma_2 \frac{\vec{B} \times \vec{E}'}{B} .$$

Since $\vec{E}' = \vec{E} + \vec{U} \times \vec{B}$, where $\vec{E}$ is an externally applied electric field,

equation 2.16 can be rewritten

$$J_x = \sigma_1 (E_x + U_y B) - \sigma_2 (E_y - U_x B), \qquad 2.17a$$

$$J_y = \sigma_1 (E_y - U_x B) + \sigma_2 (E_x + U_y B), \qquad 2.17b$$

and equation 2.15 becomes:

$$\rho \frac{\partial U_x}{\partial t} = J_y B + F = B \sigma_1 (E_y - U_x B) + B \sigma_2 (E_x + U_y B) + F \qquad 2.18a$$

$$\rho \frac{\partial U_y}{\partial t} = -J_x B = -B \sigma_1 (E_x + U_y B) + B \sigma_2 (E_y - U_x B). \qquad 2.18b$$

Differentiating both sides of equations 2.18a and b with respect to time and substituting from equations 2.18a and b, equations are found for each velocity component. These can be solved to give

$$U_x = E_y/B + F/(B^2\sigma_3) + \exp(-\alpha t) [R_1 \cos \beta t + S_1 \sin \beta t] \qquad 2.19a$$

$$U_y = -E_x/B - F\sigma_2/(B^2\sigma_1\sigma_3) + \exp(-\alpha t) [R_2 \cos \beta t + S_2 \sin \beta t] \qquad 2.19b$$

where $\alpha = B^2\sigma_1/\rho$, $\beta = B^2\sigma_2/\rho$, and $\sigma_3 = \sigma_1 + \sigma_2^2/\sigma_1$.

Applying the initial condition $U_x = U_y = 0$ when $t = 0$, the constants R_1 and R_2 are found to be $R_1 = -E_y/B - F/(B^2\sigma_3)$ and $R_2 = E_x/B + F\sigma_2/(B^2\sigma_1\sigma_3)$. Differentiation of the solutions (equations 2.19a and b) and comparison with equations 2.17a and b shows that $S_1 = R_2$ and $S_2 = -R_1$. The solutions are therefore:

$$U_x = R (1 - e^{-\alpha t} \cos \beta t) + S e^{-\alpha t} \sin \beta t \qquad 2.20a$$

$$Uy = -S (1 - e^{-\alpha t} \cos \beta t) + R e^{-\alpha t} \sin \beta t \qquad 2.20b$$

where $R = E_y/B + F/(B^2\sigma_3)$ and $S = E_x/B + F\sigma_2/(B^2\sigma_1\sigma_3)$. 2.21

These solutions are lightly damped oscillations when $\beta >> \alpha$, and are non oscillatory when $\beta < \alpha$. Above approximately 130 km $\beta < \alpha$, so that the solutions of interest are non oscillatory.

When $\vec{F} = 0$, the angle between the neutral gas motion and the applied electric field (using the general solutions 2.19a and b) is given by $\tan\theta = (e^{-\alpha t} - \cos\beta t)/\sin\beta t$. In the F-region $\alpha >> \beta$, so that $\tan\theta$ is large and the neutral motion is nearly perpendicular to the applied electric field. However, in the E-region $\alpha \sim \beta$ at some altitude (which still gives damped oscillations) but $\tan\theta$ approaches zero. Thus in the E-region the neutral gas has a sizeable component of motion in the direction of the applied electric field. Thus, it is expected that the direction of neutral motion should rotate from the direction of the applied electric field in the E-region to perpendicular to the electric field in the F-region.

In the steady-state the solutions become

$$U_x = E_y/B + F/(B^2\sigma_3) \text{ and } U_y = -E_x/B - F\sigma_2/(B^2\sigma_1\sigma_3). \qquad 2.22$$

In the absence of a mechanical force, the neutral gas takes on the ion drift velocity $(E_y/B, -E_y/B)$ in a time corresponding to a few multiples of α^{-1}. In the absence of an applied electric field, the steady-state neutral velocity is $F(1, -\sigma_2/\sigma_1)/B^2\sigma_3$ which above approximately 150 km becomes $F(1, 0)/B^2\sigma_3$. That is, the direction of neutral motion at higher thermospheric altitudes is in the direction of the applied mechanical force.

The parameter α plays the role of the time constant of neutral

response to changes in the electric field or the mechanical force and is of the same magnitude as ν_{ni}. No such simple interpretation is possible for the parameter β. It can be seen that if changes in the applied forces are slow relative to β^{-1}, there can be no oscillatory response.

2.5 MORPHOLOGY AND EFFECTS OF AURORAL PARTICLE PRECIPITATION

Primary particle precipitation into the thermosphere is responsible for the production of ionization and most of the other manifestations of the aurora. Most obvious of these manifestations is the bright discrete aurora usually seen at high latitudes. Other direct effects of the precipitation are the production of bremsstrahlung x-radiation and to a minor extent, heating of the thermosphere. The ionization produced by these particles influences the Joule dissipation of the electrojet currents. Both of these heat sources may alter the pressure distribution present in the high-latitude thermosphere.

The instantaneous pattern of particle precipitation is well defined by the luminosity produced by electronic excitation of atmospheric constituents. Thus a series of snapshots taken high above the poles would define the precipitation patterns. Recently this has become possible (Anger and Lui, 1972), but no morphological results are as yet available. Therefore this discussion is based primarily upon all-sky camera data taken at the earth's surface. Much of the definitive work in auroral morphology has been carried out by Y. I. Feldstein and coworkers (see for example Feldstein and Starkov, 1967) and S.-I. Akasofu and coworkers (see for example Akasofu, 1968).

The all-sky camera records luminosity sufficiently intense to be photographed in a circle or radius approximately 700 km surrounding the camera. Light arising from the N_2^+ first negative bands (1NG), the N_2 first positive bands and the 6300A and the 5577A lines of atomic oxygen are the principal emissions recorded. In normal operation, an IBC I aurora (see Chamberlain, 1961, for definition) can be recorded in about 8 sec. Very weak auroral arcs and glows are not photographed by this technique.

Discrete optical auroral emissions are found in a well-defined zone of latitude. Figure 2.1 illustrates in a latitude-magnetic local time frame the average location of aurora recorded on the all-sky camera as a function of magnetic activity. It is clearly seen that the zone of auroral emission is of oval shape, hence the terminology auroral oval, which broadens and expands equatorward with increasing geomagnetic activity. The index of geomagnetic activity used to separate these data is the Q index, a 15-minute index which is explained by Lincoln (1967). Within the oval the aurora appear as discrete arcs which are generally quite narrow. Maggs and Davis (1968) found the median thickness of arc elements observed in the magnetic zenith to be approximately 250 m. Apparently broader arcs and bands are frequently made up of several such thinner arc elements.

Statistically, auroral arcs are aligned along the auroral oval (Gustavfsson, 1967). Between arcs there is usually structureless auroral emission associated with particle precipitation. Bryant et al. (1973) have detected substantial fluxes of precipitating particles

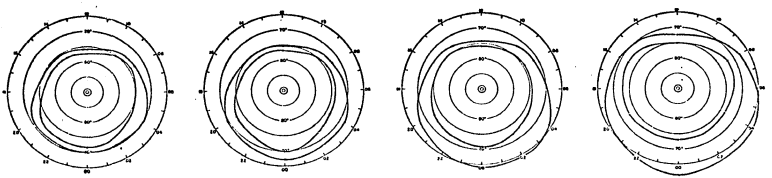

Figure 2.1 The configuration of the auroral oval as a function of magnetic latitude and corrected geomagnetic time for various levels of geomagnetic activity (Q index). Compiled from the figures of Whalen (1970).

between discrete auroral arcs with rocket-borne particle detectors. Similar measurements (Whalen et al., 1971) have been made between pulsating patches which are usually found in the post-midnight hours. The energy precipitated is usually a factor of 10 or more below that observed in the arcs and patches.

The auroral ovals, shown in Figure 2.1, are defined as the regions between the equatorward and poleward mean boundaries of zenithal occurrence of aurora recorded on the all-sky camera (Feldstein and Starkov, 1967). Only fairly bright forms (IBC I or greater) with sharp boundaries or limited extent (less than 300 km) are recorded on the all-sky camera film. There is a systematic change of the types of auroral forms seen as a function of time through the night. Arcs and bands tend to predominate prior to magnetic midnight, while diffuse patchy aurora, often exhibiting pulsations, are most commonly seen after magnetic midnight. An idealized representation of the types of auroral forms present as a function of latitude and local time is presented in Figure 2.2. This picture is drawn from visual observations for occasions when the oval expands to its Q = 6 position at the time of maximum equatorward extent. The glow feature on the equatorward edge in the premidnight sector presumably represents the hydrogen arc, a broad arc feature of 1° to 2° latitude extent (Romick and Sharp, 1967). The normal spatial relationship between proton precipitation and electron precipitation in the evening hours is shown in Figure 2.3. The regimes of luminosity produced by the protons (H-alpha) and electrons (5577A and 6300A) are indicated. Wiens and Vallance Jones (1969) have

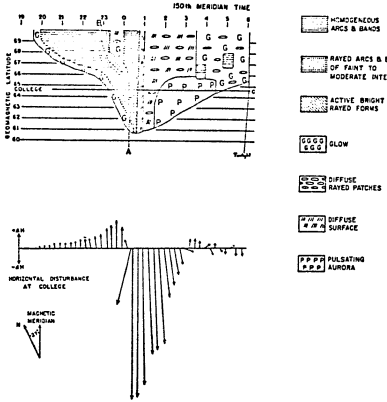

Figure 2.2 Idealized pattern of auroral and magnetic disturbance. After Heppner (1954).

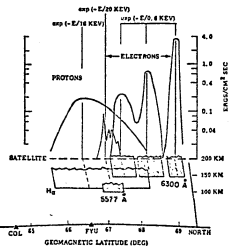

Figure 2.3 Observed relationship between precipitating protons and electrons derived from ground based optical and satellite particle measurements in the evening auroral oval. After Romick and Sharp (1967).

shown that the zone of proton precipitation generally lies equatorward of the electron precipitation before magnetic midnight, the separation being up to 3° of latitude for large Kp (a planetary index of geomagnetic activity; see Lincoln, 1965, for definition). After magnetic midnight, the region of proton precipitation is poleward of the pulsating aurora (Deehr et al., 1971). Proton precipitation produces little luminosity, ionization or heating of the thermosphere.

Boyd et al. (1972) have shown that the height of electron excited aurora decreases as the oval moves equatorward (increasing geomagnetic activity) and with increasing time through the night. These trends imply that the characteristic energies of the precipitating electrons increase as they are able to penetrate further into the atmosphere. The transition from quiet arcs and bands to pulsating and diffuse aurora (the line A-B in Figure 2.2) occurs with a change in sign of the horizontal magnetic perturbation from positive to negative as is illustrated. This transition is accompanied by large enhancements (up to a factor of 100) in the intensity of auroral emissions, rapid ray motions and occasionally Class B auroral arcs (magenta lower borders) (see International Auroral Atlas, 1963). The brightening indicates that there is a substantial increase in the total energy precipitated while Class B aurora indicates a substantial hardening of the primary energy spectrum (Hanna and Anger, 1971). Such phenomona are usually described as an auroral break-up and constitute part of the expansive phase of an auroral substorm. The morphology of an auroral break-up has been well documented by Akasofu (1964). As the morphology of

break-up is generally understood and accepted, only a brief outline emphasizing pertinent details in the present context is presented here.

At a time defined as a substorm, expansive phase, onset time an arc near the equatorward edge of the oval, usually the southernmost (in the northern hemisphere) arc, abruptly brightens and begins to move rapidly poleward. Simultaneous with this brightening nearby magnetometers show an abrupt decrease in the measured H component. The segment of the arc which brightens and moves north is usually centered on or near magnetic midnight. Large folds are observed to appear in the auroral arcs on both sides of the break-up region. These folds propagate away from the break-up with speeds up to 1 km sec^{-1}. The fold on the western (evening) side may become a complex spiral of 100 to 600 km diameter and is called a westward travelling surge. The eastern or morning fold usually takes on the appearance of a letter Ω. Shortly after the poleward expansion of the brightened arc, the midnight region of the oval, just vacated, is filled with arcs and bands which are usually bright (IBC III) and active.

On active nights (large geomagnetic activity) several break-ups may take place, departing from the idealization represented by Figure 2.2. Because of the latitude-time dependence of the auroral ovals, break-up at early local times may be seen only on the northern horizon for a station located equatorward of the oval. Under these circumstances, the passage of the westward travelling surge will be seen. After the surge passes, the auroral arcs reappear in the northern segment of the oval and usually begin to move equatorward again. Nearer the midnight sector pulsations and diffuse patches characteristic of post-

break-up appear after surge passage. If another break-up is to occur the pulsations and patches usually diminish in intensity and are replaced by weak, gradually brightening, arcs which propagate equatorward to the station again.

Few estimates of the energy deposition rates of auroral particles are reported in the literature. O'Brien and Laughlin (1962) reported one case in which the precipitated electron energy flux of 2 Joules m^{-2} sec^{-1} (2000 ergs cm^{-2} sec^{-1}) was observed. More typically, however, fluxes observed onboard Injun 3 and 4 satellites were 4×10^{-3} Joules m^{-2} sec^{-1} (O'Brien and Taylor, 1964). The corresponding global deposition rate was reported to be 4×10^{10} to 10^{11} Joules sec^{-1}. More recently Sharp and Johnson (1968) reported global rates of 3×10^{9}, 2.5×10^{10}, and 6×10^{10} Joules sec^{-1} for values of the Kp index of 1, 3 and 5, respectively. In the same paper, Sharp and Johnson reported an average 5:1 ratio for the night side energy flux (01 hours LT) to the dayside flux. In a subsequent paper, Sharp et al. (1969) give average latitudinal profiles of the precipitated electron energy flux. They report that the nightside oval energy flux peaked near 6×10^{-3} Joules m^{-2} sec^{-1} with a profile full width at half flux of 6 degrees of latitude. Also, dayside oval energy fluxes are reported to be 6×10^{-4} Joules m^{-2} sec^{-1}.

Thus the average flux of particle energy appears to be approximately 6×10^{-4} Joules m^{-2} sec^{-1} in the dayside oval and 4×10^{-3} Joules m^{-2} sec^{-1} in the nightside oval. An order of magnitude increase is reported for the global-integrated flux from quiet geomagnetic conditions to moderately active conditions (Kp 5). Much of the increase may be

attributed to the increase in the size of the auroral oval (and by definition the region into which particles precipitate) as activity increases. This point is established by Feldstein and Starkov (1971), who used the overall image density of all-sky camera photographs to estimate precipitated energy. Their analysis shows only a small variation of local energy flux (a factor of 4) with the geomagnetic Q index, while the estimated global energy received varies by a factor of 40 in the same range of Q. During a break-up, local energy fluxes may be expected to increase by a factor of ten or more in the midnight sector. Such increases only occur for the initial phase of bright active arcs and are or short duration (15 to 30 min). The energy associated with proton precipitation is reported by Sharp et al. (1967) to be small (2×10^{-5} Joules m^{-2} sec^{-1}) under quiet geomagnetic conditions. Again, an order of magnitude or more increase may be expected for periods of increased activity. However, the energy involved is significantly less than the average electron flux and can be ignored for the purposes of estimating thermospheric heating and ionization.

Energetic electrons penetrating the upper thermosphere undergo collisions with thermospheric atoms and molecules. During these collisions an electron may be ejected from the atom or molecule, causing it to become ionized, or the atom or molecule may become excited. Each ionizing collision requires approximately 35 ev of the energetic primary energy. The electron which was ejected, known as a secondary electron, usually carries some kinetic energy. Most excitation is caused by secondary electrons. The rate at which a

primary electron loses energy is a complex function of atmospheric density, and the primaries' energy. Computations of the ionization rates and excitation rates for various primary energy and pitch angle distributions have been performed by Rees (1963, 1968, 1969). Results show that the altitude of peak ionization rate decreases with increasing particle energy, and that for typical auroral primary energy spectra the peak ionization rate is near 120 km.

The total number of ion pairs produced (per m^2 sec) can be estimated from the precipitated energy flux. Approximately 270 kR per Joule m^{-2} sec^{-1} of 4278A (N_2^+ 1NG; 0-1) are produced by incident electrons (Bryant et al., 1970; Deehr et al., 1972). Thus, for an electron energy flux of 4×10^{-3} Joules m^{-2} sec^{-1}, the average nightside auroral flux discussed previously, the zenithal 4278A emission rate is approximately 1 kR and the column rate of ion pair production is 10^{13} m^{-2} sec^{-1}.

Atoms and molecules excited to metastable states may be collisionally deactivated before they radiate. Much of this deactivation energy then appears as heat. Additionally, the energy of degraded secondary electrons and highly degraded primaries is given up as heat (Dalgarno, 1964). Ion recombination results in excitation and provides the bulk of the heating of the thermosphere. Hays et al. (1973) estimate that 30% of the energy of auroral primaries appears as heat in the thermosphere. Using this estimate, the approximate thermospheric heating rate due to auroral primaries is 10^{-3} Joules m^{-2} sec^{-1}. As will be seen later this heating is small relative to the dissipation of the auroral electrojet.

The distribution of ionization in the thermosphere is controlled by production, loss, and transport processes. Each of these processes are complex, involving a number of steps, and a complete discussion of them is unwarranted. The reader is referred to Whitten and Poppoff (1971) for an extensive treatment. The high-latitude thermosphere differs in that large ion-pair production rates are possible at night, and large horizontal electric fields produce large transverse ion- and electron-drifts. Thus, the high-latitude thermosphere is different in its nighttime production and transport processes. Examples of high-latitude ionization profiles have been published by Leadabrand et al. (1972) and Watt (1973). During conditions of auroral precipitation an E layer (110 km) appears with a density of approximately 2×10^{11} electrons m^{-3}. When precipitation is not as strong or vanishes, the E layer density decreases below 10^{11} m^{-3}. Similar behavior and densities are observed in the F region. On occasion, when there is strong precipitation, the F layer density may be as large as 8×10^{11} m^{-3} (Watkins et al., 1973). Marked spatial variations in the ion density at most thermospheric altitudes are observed to correlate with the presence of auroral particle precipitation.

2.6 MORPHOLOGY OF AURORAL ELECTRIC FIELDS

Figure 2.4 shows in an idealized fashion the trajectories of several barium ion clouds with respect to the rotating earth after Davis and Wallis (1972). Geomagnetic latitude and magnetic local time are used as coordinates: only the average velocity vector is plotted. In a few cases where a marked change in ion cloud velocity was measured a broken vector is shown. Similar diagrams incorporating

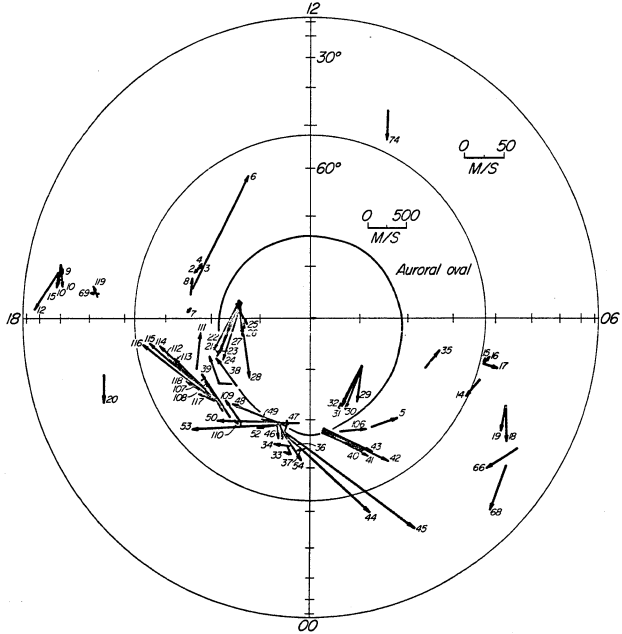

Figure 2.4 Measured ion-drift velocities from barium releases in a geomagnetic latitude-magnetic time coordinate frame. Vectors are drawn with base at the release point and are measured positive through east from north. Note that the magnitude scale changes at 53° latitude for release. Numbers refer to table in Davis and Wallis (1972).

the results from fewer clouds but representing the ion drift vectors more exactly are given by Haerendel and Lust (1970). For the present purposes, Figure 2.4 will serve adequately as it includes substantially more measurements.

In the absence of strong neutral winds, and for small releases where the height-integrated conductivities are not changed significantly by the release, the ionospheric electric field and the ion-drift velocity are related by the equation

$$\vec{E}'_{\perp} = -\vec{V}_{\perp} \times \vec{B}. \qquad 2.23$$

$\vec{V}_{\perp}$ and $\vec{E}'_{\perp}$ are, respectively, the components of the ion-drift velocity and the electric field perpendicular to the magnetic field $\vec{B}$. At high latitudes (latitude 60°, geomagnetic) it is reasonable to assume that $\vec{B}$ is directed vertically downward everywhere and has magnitude $|\vec{B}| = 0.5 \times 10^{-4}$ tesla. Under these assumptions, the electric field vector associated with each barium ion-drift vector is 90° clockwise from the indicated ion-drift vector. The magnitude in mv m^{-1} is given by $|\vec{E}'_{\perp}| \simeq |\vec{V}_{\perp}| / 20$ when $|\vec{V}_{\perp}|$ is expressed in units of m sec^{-1}. Thus at auroral oval locations and somewhat equatorward of the oval, the electric field is predominantly northward prior to 21 hours and predominantly southward between 23 hours and 06 hours. In the polar cap (inside the indicated auroral oval which corresponds to the poleward edge of the Q = 3 oval) the electric field is approximately parallel to the line from 18 to 06 hours and points toward the evening sector. This gross morphology is similar to that described by Axford and Hines (1961). Below 52° geomagnetic latitude, the electric field is quite small (< 3 mv m^{-1} typically) and does not show any really systematic

pattern of direction. An analysis of the electric field at middle and low latitudes is given by Rieger (1970).

In the auroral oval near 23 hours magnetic time, the electric field has no clearly-defined direction. Additionally, the magnitude of the electric field in this region is quite variable. Heppner (1969, 1972a) has identified this region, which he calls the Harang Discontinuity, as corresponding to statistical reversal in the magnetic ΔH perturbation, from positive ΔH to negative ΔH. When suitable analysis procedures are applied to magnetic records it is found that, for any given degree of activity, a line may be drawn which separates the regimes of positive and negative ΔH. This line moves westward (e.g., to earlier magnetic times) as latitude is increased (see Harang, 1946). Heppner (1972b) illustrates this behavior and configuration of electric fields in a diagram reproduced here as Figure 2.5 which is drawn for $Kp \gtrsim 3$. Heppner (1972a) suggests that the location of the discontinuity at any fixed latitude may move as much as three hours in local time and atypically as much as five hours. For example, at 60° geomagnetic latitude the discontinuity is expected to be within the magnetic time range 2130 to 0100 66% of the time, and 96% of the time to fall in the range 2030 to 0300.

The Harang Discontinuity is in reality an average dividing line between zones of predominant positive and negative ΔH. Heppner has extended the concept in order to describe the morphology of individual nights of activity. As such the discontinuity is a convenient reference line to divide zones of positive and negative ΔH. Other phenomena such as the direction of some auroral motions and the character of

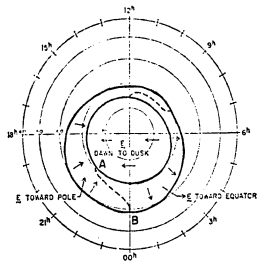

Figure 2.5 Configuration of the auroral oval and polar cap electric fields and the local time-latitude variation of the Harang discontinuity (dashed line A-B) based upon barium releases and magnetometer data. After Heppner (1972b).

particle precipitation change from one side of this line to the other. However, the extension to individual events brings with it some difficulties. For example, a negative bay may occur abnormally early or late, or there may be several negative bays during a night clearly separated by periods of positive disturbance. Not only must the discontinuity move back and forth in local time, but the whole pattern must expand and contract about the geomagnetic pole, in order that such events be made to fit into the pattern. While this motion may be related to changes of the auroral oval size, this description appears artificial on complex nights. However, the concept may have value in describing the average behavior of magnetic perturbation over several nights.

Electrostatic probe measurements of the electric field strength made from polar orbiting satellites have been reported by Heppner (1972b, 1972c), Frank and Gurnett (1971), Cauffman and Gurnett (1971), and Gurnett and Frank (1973). While only one component of the electric field is measured, the results confirm the morphology developed from the barium cloud measurements. Field strengths in the auroral zone are observed to be as large as 125 mv m^{-1} (Maynard, 1972). Heppner (1969) has defined the regions of large north-south electric field strengths in the auroral zone as the "auroral belts". Employing an arbitrary threshold of 5 mv m^{-1} to define the equatorward boundary of the auroral belts, he finds (Heppner, 1972b) that the equatorward boundary in the evening (18 hours magnetic time) is located at 65° and 60° (geomagnetic latitude) for K_p equal 2 and 4, respectively. The equatorward boundary on the morning side (06 hours) is reported to lie at 66° and 62° for

K_p equal 2 and 4, respectively. The polar cap-auroral belt boundary is reported to lie at 73° ± 3° (a diurnal variation), independent of geomagnetic activity. Thus the evening auroral belt is wider than the morning auroral belt.

The electric field in the polar cap is directed from dawn to dusk. The magnitude of this field is observed to vary from 5 to 30 mv m^{-1}. The field can be uniform or can possess a significant gradient. Heppner (1972c) has shown that departures from a uniform polar-cap electric field can be related to the direction of the interplanetary magnetic field. The field strength is observed to increase with magnetic activity, but an analytic relationship has not as yet been demonstrated. Mendillo and Papagiannis (1971) theorize that the field strength is proportional to the square of the solar wind speed. The potential drop across the polar cap ranges from 20 to 100 kv. For K_p = 3, values between 40 and 70 kv are usually observed. The potential drop across the polar cap approximates the sum of the potential drops across the auroral belts in the dawn-dusk plane (Heppner, 1972b).

Wescott et al. (1970), Potter (1970) and Aggson (1969) have demonstrated that the electric field in the auroral belts decreases to small values inside auroral arcs even when the electric field strength is observed to be large immediately adjacent to the arcs. Similarly, depressions of the electric field strength are observed in satellite probe measurements. The cause of these depressions of the electric field strength is not known, but they are consistent with a geometry of enhanced conductivity in the arcs in a current limited situation. The reversal of the sign of the electric field

between the polar cap and auroral belt is reported by Swift (1973) to occur near or poleward of the structured auroral arcs on the poleward side of the oval. Multiple reversals are also observed (Gurnett and Frank, 1973).

So far the morphology of electric fields has been presented in a magnetic latitude-local time coordinate frame. To illustrate the temporal behavior of the electric field at an auroral zone station, ion drift measurements at 220 km by Doupnik et al. (1972) are presented in Figure 2.6. The ion-drift velocity is plotted with respect to north (radially inward). Measurements began at 1930 local time February 19, 1972 and were carried out for 24 hours. These data were acquired by the 23 cm incoherent scatter radar facility at Chatanika, Alaska. The strong tendency for westward ion-drift (northward electric field) in the premidnight hours and eastward drift in the post midnight hours is clearly evident. A negative bay began on the College magnetogram about 2310 LT and continued until 0420 LT except for a brief period 0020-0030 during which a positive (100 γ) excursion was present. The time period from the beginning negative bay until shortly after the positive excursion appears to have first westward then eastward electric fields. Thereafter the regime of southward electric field becomes well established. During the daytime a predominant eastward field is present.

2.7 MORPHOLOGY OF HIGH LATITUDE CURRENTS

Two intense current systems are now thought to exist in the auroral ionosphere in or near the auroral oval. These currents are illustrated in Figure 2.7. This particular configuration was proposed by Suguira and Heppner (1965). The more intense westward current is seen to be in

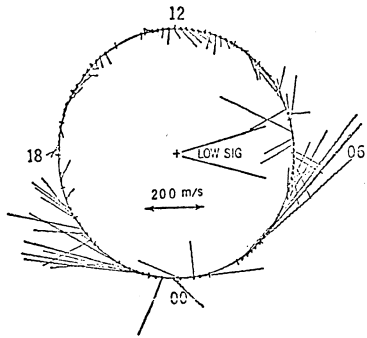

Figure 2.6 Ion-drift vectors obtained in a 24 hour period by the Chatanika, Alaska, incoherent scatter radar beginning 1930 LT 10 February 1972, at 220 ± 30 km, in geomagnetic azimuth and local time. From Doupnik et al. (1972).

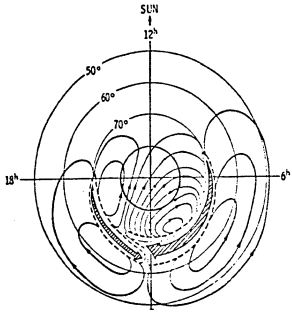

Figure 2.7 A configuration of the auroral electrojets. After Sugiura and Heppner (1965).

the morning auroral belt, the region of equatorward electric field, while the eastward current appears in the evening auroral belt. The westward current system (or electrojet) has long been recognized as an important feature of auroral latitudes (Silsbee and Vestine, 1942). The independent existance of the premidnight eastward current system is now established (Rostocker, 1972a). Previously, magnetic perturbations in the evening sector were thought by some investigators to be due to return currents from a dominant westward electrojet. However, Rostoker and Kisabeth (1972) have shown that intensifications of the eastward electrojet may take place independent of temporal changes in the westward electrojet, thus casting doubt on the return current theory. Presently the existence of return currents across the polar cap is being questioned (Heppner et al., 1971a; Haerendel et al., 1971) because the electron density of the polar cap at times is very low $< 10^{10}\ m^{-3}$, and because of a lack of detailed correlation between polar cap ΔH measurements and electric field variations. Kamide (1973) suggests that the equatorward return currents may be limited to within 10 degrees of the latitude of the electrojets, again because of low conductivity. Further investigations are necessary to define the magnitude and extent of return currents.

There is considerable evidence that high-latitude currents are not completed within the ionosphere so that the current circuits have to be completed in the magnetosphere by way of field-aligned, Birkland, currents. While several models have been proposed (Bostrom, 1964; Heppner et al., 1971b), no solution of this continuity problem has yet been agreed upon. Additional direct measurements of the Birkland currents

are necessary. A recent study by Berko et al. (1973) finds evidence of field-aligned currents in most regions of the auroral belts indicated in Figure 2.5 and finds good correlation between field-aligned currents and the presence of precipitated electrons. This work must be carried out for individual events and correlated with ground-based magnetic and all-sky camera data before the ionospheric circuit of the electrojets can be properly understood.

Surface magnetometers measure the magnetic perturbation due to an average of the ionospheric currents over a considerable region of latitude ($\sim \pm 1°$ of latitude) and they cannot be expected to resolve details smaller than a length equal to the height of the dynamo layer. Appreciable fine structure cannot therefore be seen. However structures larger than approximately 2° are observed and are discussed in the literature. Kisabeth and Rostocker (1971) examine the behavior of these large scale structures within the westward electrojet and find that they behave independently. Apparently the equatorward section of this current structure intensifies and is dominant for the first 10 to 20 minutes after substorm expansive phase onset. Then the northward structure intensifies and may continue to do so quasi-periodically at approximate 15 minute intervals throughout the substorm. These intensifications are reported to be latitudinally confined and short-lived. The main electrojet (the southward structure) exhibits independent variations but is more generally stable in intensity and position after the substorm has begun.

In contrast to surface measurements, rocket and satellite measurements emphasize intense localized currents. This arises because of the

geometry of observation, the rocket being close to the location of the currents. Potter (1970) reports that "the westward electrojet often flows parallel to visible auroral forms and is comprised of a series of thin current filaments of varying intensity". Similar filamentary structure is also reported by Choy et al. (1971). The parallelism between the electrojets and auroral arcs can also be observed from the ground under special circumstances even in complex auroral geometries of loops and spirals (Kisabeth and Rostoker, 1973).

In the auroral oval and slightly equatorward of the oval, premidnight electric fields are directed northward while postmidnight fields are southward. Provided that the magnetic perturbation due to field-aligned currents can be ignored, the time at which the electric field changes sign can be determined from the change in sign of the horizontal magnetic perturbation. This arises because the Harang Discontinuity, which marks the magnetic sign change, also marks the reversal of the electric field. It is established that the auroral electrojet currents are predominantly Hall currents (Wescott et al., 1970; Potter, 1970). As such, the electric field direction is substantially the same as the magnetic perturbation measured at the surface of the earth. Haerendal (1970) concludes "... that the magnetic perturbations on the ground are good indicators of the direction, but not the magnitude of the field." The magnitudes do not bear any relationship because of a strong variability of auroral zone ionization and the corresponding variability of the conductivities, particularly at dynamo heights. The correspondance of directions, however, is important and is employed later in this study.

Estimates of the magnitude of an equivalent line current which would cause an observed magnetic disturbance are easily calculated with assumption of the height of the current. Typical values range from 5×10^3 amps to 10^6 amps for disturbances in the range 10 γ to 2000 γ, respectively (distance assumed to be 150 km). Equivalent infinite sheet currents are of the order of 10^{-2} to 3 amps m^{-1} for the same range. Assuming this sheet to have thickness 20 km, the equivalent uniform sheet current densities are 10^{-6} to 10^{-4} amps m^{-2} for the same range of magnetic disturbance. Park and Cloutier (1971) infer an electrojet current of 6×10^3 amps from their rocket magnetometer data. The ground magnetic disturbance at the time of their flight was 20 to 40 γ, so that their data indicate that a substantial portion of the disturbance seen on the ground was due to the confined electrojet detected. However, it is not possible at this time to determine if all of the electrojet current is carried by thin filaments such as observed by Potter (1970) and Park and Cloutier (1971); or if only part is carried in filaments and part in an extended sheet current. The latter possibility is suggested by the precipitation of particles in the evening sector where discrete arcs are observed to have substantial fluxes between them. If this alternative holds, the ratio of discrete currents to diffuse (sheet) current is likely to vary as a function of time throughout the night corresponding to the variation in the character of precipitation.

In principle, the distribution of ionospheric current can be calculated from the distributions of the electric fields and conductivities. As stated earlier, there is insufficient knowledge of

the spatial fine structure of the electric field within the ionosphere to permit this calculation to be performed with any degree of accuracy. Our knowledge of the conductivity is similar. It is therefore difficult to model the auroral electrojet for a realistic situation.

The Joule dissipation of ionospheric currents may be expressed using equation 2.22 as

$$\vec{J} \cdot \vec{E}' = \sigma_1 (E_\perp')^2 + \sigma_\parallel (E_\parallel')^2 \qquad 2.24$$

where $\vec{E}_\perp'$ and $E_\parallel'$ are the magnitudes of the components of the electric field seen by the ions and electrons, respectively, perpendicular and parallel to the magnetic field. Usually $E_\parallel'$ is assumed to be zero. Due to incomplete knowledge of the fine structure of the electric field and poor knowledge of the distribution of $\vec{J}$, it is not possible to model $\vec{J} \cdot \vec{E}'$ with reasonable assurance of approximating reality. However, it is possible to make some numerical estimates of the Joule dissipation for comparison with precipitated particle energy fluxes.

Values of the Pedersen conductivity were scaled from Swift's (1972) aurorally disturbed model ionosphere graph. The Joule dissipation $\sigma_1 E_\perp'^2$ was computed assuming $E_\perp' = 20$ mv m^{-1}, a typical value derived from auroral zone barium releases. The results are presented in Table 2.3 and in Figure 2.8 (dashed curve). The Joule dissipation for this case is strongly peaked near 120 km where it reaches a value of 1×10^{-7} Joules m^{-3} sec^{-1}. Integrating (approximately) over altitude, the column dissipation rate is 3×10^{-3} Joules m^{-2} sec^{-1}. Since the horizontal electric field often exceeds the 20 mv m^{-1} used here, it is probable that the Joule dissipation is more important for thermospheric

TABLE 2.3

ALTITUDE DEPENDENCE OF THE PEDERSEN CONDUCTIVITY (AFTER SWIFT, 1972) AND JOULE DISSIPATION OF THE PEDERSEN CURRENT WHEN THE ELECTRIC FIELD HAS A VALUE OF 20 mv m^{-1}

Altitude (km)	Pedersen Conductivity (mho m^{-1})	Joule Dissipation (Joules m^{-3} sec^{-1})
90	1.0 - 5	4.0 - 9
100	2.2 - 5	8.8 - 9
110	1.2 - 4	4.8 - 8
120	2.6 - 4	1.0 - 7
130	1.1 - 4	4.4 - 8
140	5.5 - 5	2.2 - 8
150	3.0 - 5	1.2 - 8
175	1.5 - 5	6.0 - 9
200	1.1 - 5	4.4 - 9
250	8.5 - 6	3.4 - 9
300	3.7 - 6	1.5 - 9
350	1.5 - 6	6.0 - 10

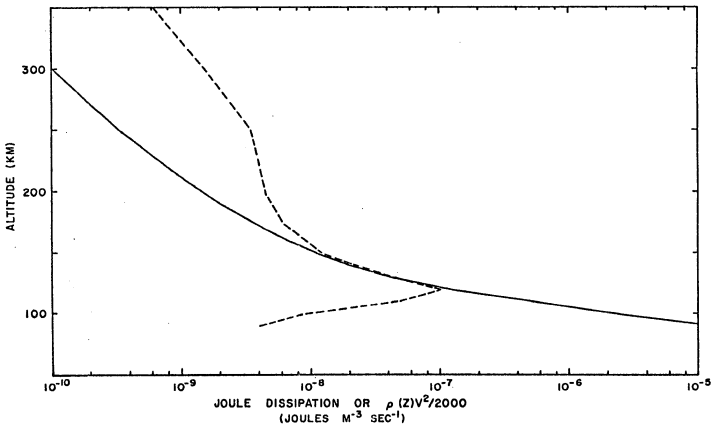

Figure 2.8 Altitude dependence of Joule dissipation of a model electrojet (dashed curve) and the average rate at which kinetic energy must be supplied to the thermosphere to produce a 100 m/sec wind (solid curve). See text for details of the parameters.

heating than particle precipitation when long time scales are considered (> 3 hours).

These estimates of the Joule dissipation can be used to obtain a crude estimate of the lowest altitude at which geomagnetically associated perturbations of the wind field can occur. This estimate is made by comparing the rate at which energy is dissipated in the electrojets to the rate at which kinetic energy must be supplied to drive a wind perturbation. However, not all of the dissipation is available to bulk motion and much of it results in increased thermal and potential energy. Accordingly, an estimate of the rate at which energy must be dissipated in order to produce a wind of speed U(z) is $\rho(z)U^2(z)/2\ k_j\tau$ where τ is the time over which the acceleration takes place and k_j is the fraction of the Joule dissipation which appears as bulk motion. For the purposes of this calculation, it is assumed that α^{-1} (of equation 2.19) can be approximated by 10^4 sec independent of altitude, and that α^{-1} can be used for τ. Values of $\rho(z)\ U(z)^2/\ 2\ k_j\tau$ are plotted as the solid curve in Figure 2.8, under the assumptions U(z) = 100 m sec^{-1} for all z and k_j = 0.1. Values of $\rho(z)$ were taken from the CIRA (1965) model (5) atmosphere (for 00 hours). Comparing the energy rate requirement as a function of altitude with the Joule dissipation curve, it can be seen that sufficient energy is available at all altitudes above approximately 130 km. An increase in the dissipation by a factor of 50, which could result from a 100 mv m^{-1} electric field and a factor of 2 increase in the Pedersen conductivity, lowers the altitude to 110 km. The slope of the curve is such that these altitudes are fairly insensitive to the value of the energy conversion factor k_j.

Under conditions of moderate geomagnetic activity, it is expected that perturbations of the thermospheric wind field will occur above 130 km. During major geomagnetic storms, however, perturbations as low as 110 km may occur.

Large variability can be expected to occur in the Pedersen conductivity, as it is proportional to the electron density. Additionally, the observation that E_I' approaches zero inside auroral arcs indicates that dissipation (as well as the Hall current) is located outside of auroral arcs. This conclusion is also reached by Cole (1971) who required continuity of the Pedersen current across highly conducting strips associated with auroral arcs.

The altitude profile of Joule dissipation is given by the values in Table 2.3. Longitudinally the magnitude of the dissipation should not vary significantly on the nightside but should decrease markedly on the dayside because of the decreased electric field there (see Figure 2.6). Latitudinally, dissipation may be expected to remain near the tabulated values from the polar cap boundary to at least the latitude of the equatorward edge of proton precipitation in the evening. Temporal variations in the dissipation should be marked because both the Pedersen conductivity and the magnitude of the electric field vary with substorm time. The magnitude of the dissipation should vary approximately as the square of the horizontal magnetic perturbation ΔH (Cole, 1971).

Most of the energy produced in the auroral electrojets by Joule dissipation appears directly as heat shared by the constituents of the thermosphere. Neutral- and ion-heating rates are approximately equal

(Rees and Walker, 1968), but the neutral density greatly exceeds the ion density so that the ion temperature is found to be greater than the neutral temperature. Substantially more heat is provided to the ions than the electrons at all altitudes (Omholt, 1959). Low electron temperatures would result, at low altitudes, except that the electron gas is preferentially heated by secondary electrons when precipitation is present. At high altitudes, heat is efficiently transferred between ions and electrons (Walker and Rees, 1968) to maintain an approximate temperature equilibrium. Heat is removed from the neutral gas by electron conduction, vertical mass motion, and radiation from the fine structure levels of the ground state of atomic oxygen.

Computations of the neutral, ion, and electron temperature profiles for typical auroral disturbances are presented by Rees and Walker (1968), and Walker and Rees (1968). In the E-region the ion and electron temperatures increase much faster with altitude than the neutral temperature. Generally, the electron temperature exceeds the ion temperature. Under conditions of moderate to large magnetic activity the ion temperature is greater than the neutral temperature by 600°K to 1000°K at 200 km. Above 200 to 250 km the vertical gradients of all three temperature profiles decrease.

CHAPTER 3

MODELS OF THERMOSPHERIC WINDS

The basic response of the thermosphere to perturbing forces has been briefly reviewed in the last chapter. Attention is now directed to more realistic models of the thermosphere's actual response to the forces present. Several papers reporting solutions of the neutral equation of motion for winds driven by the diurnal (solar) heating and cooling have appeared in the literature. These models are discussed and compared. The winds modelled by these papers are expected to be global in extent and therefore should appear at high latitudes. These (tidal) winds can be perturbed at high latitudes by auroral electric fields and auroral heating. Two models of ion-drag acceleration are reviewed. Lastly, two models of the wind perturbations due to auroral heating are examined.

3.1 TIDAL WIND MODELS

The diurnal heating and cooling of the thermosphere produces a global pattern of pressure disturbance at all thermospheric altitudes which is fixed with respect to the sun. It is observed that a pressure maximum appears at the sub-solar latitude at 14 hours local time. A corresponding pressure minimum is observed at 0330 hours. The horizontal pressure-gradients resulting from this pressure pattern drive horizontal winds. An average pressure disturbance as a function of latitude and local time has been derived from satellite drag measurements by Jacchia and Slowey (1967). This empirical pressure model has been employed by a number of authors to model thermospheric winds. Because the fundamental period associated with the pressure disturbance is one day (associated with the earth's rotation under the fixed pressure pattern) and the wind system

generated is global in extent, the winds generated by this pressure disturbance are referred to here as tidal winds.

A number of authors have employed the observed average pressure distribution of Jacchia and Slowey (1967) to generate the pressure-gradient terms of the equation of motion. After applying suitable assumptions for the ion density, electric field and other parameters, the equation of motion is solved for a network of grid points on a computer. Geisler (1966, 1967), Kohl and King (1967) and King-Hele and Allan (1966) have made preliminary calculations employing a number of approximations. Challinor (1968, 1969, 1970a) and Bailey et al. (1967) have made more detailed calculations which predict the wind field well enough that perturbations of satellite orbital parameters are duplicated. These authors, together with Duncan (1969) and Challinor (1970b) have been successful in explaining some of the observed features of F-region behaviour in terms of their tidal models. Excellent reviews of these calculations are given by Kohl (1970) and Rishbeth (1972). Three models of tidal winds are examined next. These models assume equinoctial conditions and coincidence of the magnetic and geographic poles.

Challinor's Model

Challinor (1968, 1969, 1970a) has numerically integrated the modified equation of motion

$$\frac{d\vec{U}_\perp}{dt} = -2\vec{\Omega}\times\vec{U}_\perp \quad - \frac{1}{\rho} \quad \nabla P \quad - \nu_{ni} \, (\vec{U}_\perp - \vec{V}_\perp)$$

That is, the viscous term and vertical motions were ignored, and the nonlinear term was retained. Jacchia and Slowey's (1967) asymmetric pressure distribution function was used to compute the pressure-gradients.

The maximum and minimum pressures fitted to this distribution function were taken from the CIRA (1965) model (5) atmosphere. The density was assumed to vary in the same way as the pressure. The ion velocity was computed from a dynamo electric potential distribution. Assumptions were also made of the global electron density distribution and conductivity distribution at 250 km.

The component equations of motion were solved at a number of latitudes by an iterative procedure in which longitude was cycled in 1° steps until the solution converged (3 to 8 cycles of longitude). The results of these calculations are shown in Figure 3.1. The ordinate is local time and the abscissa is geographic latitude. The higher nighttime speeds due to ion-drag (frictional loss) are easily seen. At high latitudes, winds are poleward during the daytime and equatorward at night. Equatorial winds are zonal: eastward in the evening and westward in the morning hours. Nighttime speeds are 150 to 300 m sec^{-1} and daytime speeds range from 50 to 150 m sec^{-1}.

Kohl's Model

Kohl (1970) reports the results of a similar calculation for 400 km, which has been redrawn and presented as Figure 3.2. (The results were redrawn so that they can be easily compared with Figure 3.1.) A specific statement of the assumptions used by Kohl is not given in the paper. It is easily seen that Kohl's model is very similar to Challinor's model for 250 km.

Vest's Model

Vest (1973) has published the results of his tidal wind calculations for 140, 180 and 300 km. These results are presented as Figure 3.3.

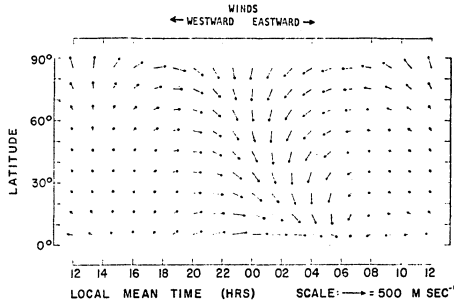

Figure 3.1 Model tidal wind field at 250 km. After Challinor (1970a).

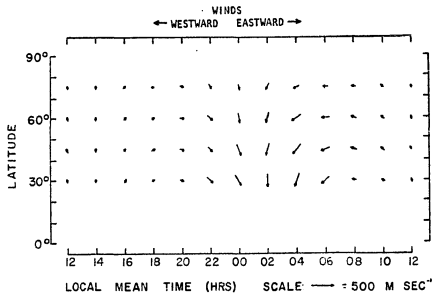

Figure 3.2 Model tidal wind field at 400 km. After Kohl (1970).

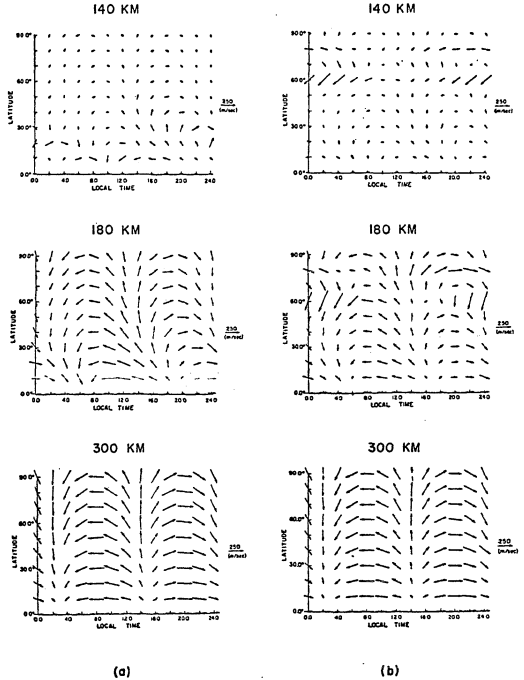

Figure 3.3 Plots of tidal winds at 140 km, 180 km, and 300 km altitudes as a function of latitude and local time (a) without auroral heating and (b) with auroral heating. After Vest (1973).

Vest included all of the terms of the equation of motion except the ion-drag term. Additionally, Vest computed the diurnal pressure (and density) perturbations from a solar heating model rather than using the empirical pressure distribution of Jacchia and Slowey (1967). Two models were treated: with and without auroral heating. Discussion of the auroral heating model is deferred until later in this chapter, and attention is confined here to the unperturbed model. The wind pattern, presented in Figure 3.3a, is similar to that of Challinor's model but the magnitudes of Vest's daytime winds are too large by a factor of 3 at midlatitudes. Vest notes this discrepency and states that it is due to the neglect of the ion-drag term. Vest's model for 300 km agrees rather well with Challinor's 250 km model when allowance is made for the magnitude discrepancy. An important feature of this model is the lack of phase change of the winds with altitude. Basically the winds above 200 km appear to be similar to those at 250 km and above, except that they are reduced in amplitude.

3.2 COMPARISON OF TIDAL WIND MODELS WITH OBSERVATIONS

There appears to be basic agreement, at least in the F-region, between the models proposed by various authors for the tidal wind field. Several authors have employed these models to predict the behaviour of ionization, and for the most part are successful. As a further test of the tidal models, comparison is made with observed winds and the wind field deduced from the S_q magnetic variation.

Winds Deduced from the S_q Magnetic Variation

Neutral motions drive charged particle motions in the thermosphere according to equation 2.5. In the dynamo region (90 to 130 km), a

current results from differences in the ratio of the collision frequency to the gyrofrequency for ions and electrons. This current produces small but regular magnetic perturbations (the S_q variation) which are measured at the earth's surface. The diurnal wind field deduced from a study of the S_q variation by Kato (1956) is presented as Figure 3.4. The basic pattern of the deduced wind vectors is similar to that calculated for greater altitudes by Challinor (1970a) and Vest (1973). The maximum deduced wind speeds are approximately 100 m sec^{-1}, or about half the amplitude predicted for 250 km. Aside from a minor change in direction of the low-latitude vectors, there is only one significant difference in that the time of reversal of zonal wind components at auroral latitudes is shifted from about midnight to 03 hours. Otherwise the patterns are similar.

Derivation of dynamo region winds from observed magnetic variations are based upon assumed conductivity distributions. In addition, it is necessary to place a condition upon the wind field. The condition often used assumes the wind field to be expressed as the gradient of a velocity potential (Chapman and Bartels, 1940). Kato (1956) required, more realistically, that the wind field satisfy a linearized equation of motion (equation 2.1 with Coriolis, inertial and pressure-gradient terms retained). A more recent approach to this problem tries to find solutions to the neutral equation of motion subject to solar heating and lunar gravitation driving forces through the pressure-gradient term (Tarpley, 1970). These solutions are then used to predict current distributions and magnetic variations. However, this approach cannot yet predict the observed magnetic variations. Kato's deduced wind field is probably the best

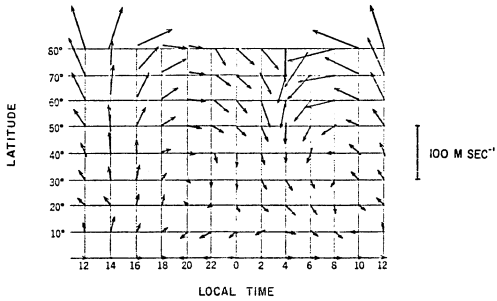

Figure 3.4 The dynamo region wind field deduced from the magnetic S_q variation. After Kato (1956).

available model for the dynamo region wind field.

The agreement between Kato's wind field and the models of Challinor and Vest is fair. The mode represented by Kato's wind field is predicted to be evanescent, and depends upon a local driving force. This mode does not allow rotation of the wind vector with altitude. Thus the basic agreement between the models and Kato's derived wind field is very reasonable, and implies that the variation of wind direction predicted by the models holds at all altitudes of interest in this study. Kato (1957) also derived a semi-diurnal wind field from the magnetic variation data. The computed semi-diurnal wind magnitudes are much smaller than the diurnal winds and are unimportant at auroral-zone latitudes.

Low- and Middle-Latitude Winds Deduced from Trail Releases

Bedinger (1970) compared the directions of motion of some 21 low- and middle-latitude trail releases (at latitudes between 8° and 40° geographic) with the predicted directions of motion from Challinor's (1970a) model. Data were taken from the highest triangulated points which ranged from 180 to 260 km (mean 196 km). The releases were approximately uniformly distributed in season over a 10-year span. The data were segregated into evening and morning twilight periods. The morning releases (8 in all) agreed well in magnitude and direction with the model predictions. About one half of the evening twilight observations are in agreement with the model. In general, Challinor's model seems to basically predict the motions of the low- and middle-latitude thermosphere.

The deviations from Challinor's (1970a) model seen in Bedinger's (1970) results may be related to the influence of geomagnetic activity on the low- and middle-latitude wind field. Such an effect might be

induced by an additional pressure perturbation associated with the geomagnetic activity. Further speculation is unwarranted until the influence of geomagnetic activity at high latitudes is understood. Nevertheless, it should be noted that Smith (1968) and Hays and Roble (1971) have discussed the possibility of such perturbations in their interpretation of specific low- and middle-latitude observations of anomalously large equatorward winds at times of geomagnetic storms. If such is indeed the case, and deviations from the tidal models are observable at low and middle latitudes, then such perturbations should be even more obvious in similar comparisons at high latitudes where the bulk of the energy associated with geomagnetic activity is deposited.

3.3 MODELS OF THE HIGH-LATITUDE WIND FIELD PERTURBATION DUE TO ION-DRAG

Rishbeth (1972) has suggested that the tidal wind field changes somewhat under the influence of geomagnetic activity, possibly as a result of changes in the thermospheric composition. However, the terms in the equation can also change. The viscous-drag term will decrease with the density increase associated with geomagnetic activity. The CIRA (1965) atmospheric models at 200 km allow a factor of 2 density increase between low- and high-activity. This density factor is the same factor as is given for day-night pressure difference change between low- and high-activity. No change should occur at 200 km, then, in the magnitude of the pressure-gradient term. At 300 km, the density does apparently increase faster than the total pressure differential, implying decreased wind speeds in the upper thermosphere at times of high activity. However, the energy input to the thermosphere can also significantly increase during periods of geomagnetic activity. A possible large

source of energy for the neutral thermosphere is the large-scale electric field observed in the auroral zone. Examination of the mechanism whereby the electric field can accelerate the neutral thermosphere was presented in Chapter 2. Examination is now made of two specific models of this ion-drag acceleration.

Fedder and Banks' Model of Ion-Drag Winds

Fedder and Banks (1972) have found a solution to the coupled equations of ion and neutral motion. The set of equations they used are for the ions:

$$\frac{\partial \vec{V}_\perp}{\partial t} = \frac{q_i}{m_i} \left(\vec{E}_\perp + \vec{V}_\perp \times \vec{B}_\perp \right) - \nu_{in} \left(\vec{V}_\perp - \vec{U}_\perp \right), \qquad 3.2a$$

and for the neutrals:

$$\frac{\partial \vec{U}_\perp}{\partial t} = \frac{1}{\rho} \frac{\partial}{\partial z} \left(\mu \frac{\partial \vec{U}_\perp}{\partial z} \right) + \nu_{ni} \left(\vec{V}_\perp - \vec{U}_\perp \right) \qquad 3.2b$$

The pressure-gradient and Coriolis forces were neglected. The electric field was assumed to vary as $E(t) = 20\ [\ 1 - \cos(\pi\ t/1800)]$ mv m^{-1} for $0 \leq t \leq 1800$ sec and be 40 mv m^{-1} for $t > 1800$ sec. (Another model was considered in which the electric field strength was assumed to be periodic, $E(t) = 20\ [\ 1 - \cos(\pi\ t/1800)]$ mv m^{-1} for $t > 0$ sec. This model gives essentially similar results and is not considered further.) A suitable atmospheric density model was chosen along with moderate electron densities. It was assumed that both $\vec{V}_\perp$ and $\vec{U}_\perp$ were zero at $t = 0$. Boundary conditions assumed were $\vec{U} = 0$ at 100 km and $\partial\vec{U}/\partial t = 0$ at 500 km. It is stated by the authors that these boundary conditions affect the solutions only within one atmospheric scale height of the assumed boundary. The horizontal components of the ion and neutral velocities were computed

by numerical integration as a function of time for several altitudes. These results have been replotted in Figure 3.5 (a, b, c and d) to give the theoretical speed and direction profiles at four times t = 1, 2, 3, and 6 hours, respectively, after the field was turned on. The wind speed plotted in these diagrams is the fraction of the ion-drift speed E/B, which the neutral wind would attain in the steady state. For plotting purposes it was assumed that the electric field was directed northward. For a southward field, north and west would become south and east, respectively. Above 200 km the neutral wind acquires the ion-drift speed and direction quickly (1 to 1-1/2 hr), but the time required below 150 km is longer. At early times the neutral acceleration and hence velocity reflects the direction of ion motion as a function of altitude. That is, there is a substantial turning to the Pedersen (north) direction with decreasing altitude below 200 km. As the magnitude of the neutral velocity increases with time, viscosity becomes relatively more important and causes downward momentum transport. Thus the speed profile steepens below 150 km and there is a corresponding change in the wind direction between 125 and 200 km toward the direction of ion motion at the upper levels.

The presence of other forces, for example horizontal pressure-gradients, can result in a change in the velocity profiles shown in Figure 3.5. It is anticipated that much of the influence of these forces will be seen in the direction profile and the speed profile will not change appreciably. The importance of these forces can only be assessed by comparing the results of this simplified theory to observations.

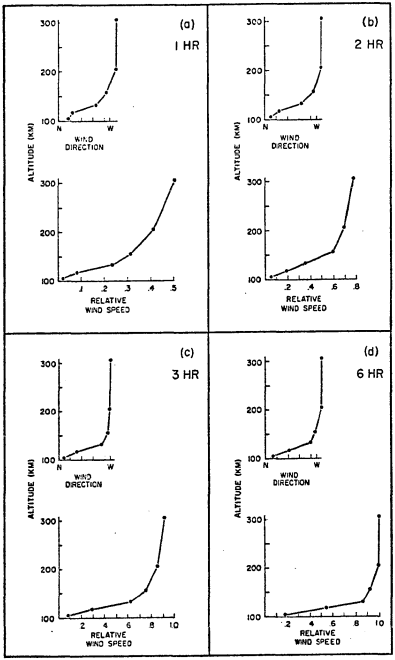

Figure 3.5 Theoretical ion drag winds as a function of height for (a) 1 hour (b) 2 hours (c) 3 hours and (d) 6 hours after turning on of an electric field of 40 mv m^{-1}. After Fedder and Banks (1972).

Heaps' Model of Ion-Drag Winds

Heaps (1972) has solved the neutral equation of motion

$$\frac{d\vec{U}}{dt} = \frac{1}{\rho}\nabla\cdot(\mu\nabla)\,\vec{U} - 2\vec{\Omega}\times\vec{U} - \frac{1}{\rho}\nabla P + g + \vec{J}\times\vec{B}$$

where the ion-drag term has been replaced by $\vec{J}\times\vec{B}$ in order to avoid explicit dependence upon the ion velocity. The current density $\vec{J}$ was computed using a time-independent tensor conductivity. The electric field was assumed to be both a function of latitude and time. Peak magnitudes were chosen to be 50 mv m^{-1} northward at 23 hours magnetic time and southward 50 mv m^{-1} at 01 hours. Between 23 hours and 01 hours the electric field was chosen to vary linearly with time so that it passed through zero at midnight. From noon until 23 hours it was directed northward and increased exponentially to its peak value. An exponential decay was also assumed from 01 hours to noon. A gaussian-like latitudinal distribution was assumed with a peak at 60° invariant latitude and a full width at half maximum of 5°. This variation was obtained in approximation by an eight-term cosine series which had attendant nulls and non-zero strengths over the polar-cap region and equatorward of the region pervaded by the field. These apparently do not have any effect on the ion-drag wind solutions.

The vector equation of motion was solved numerically by an iterative computer technique to find the ion-drag wind as a function of time (taken in small steps) for various latitudes and altitudes. Cartesian coordinates were used and uniformity was assumed along one axis to remove dependence on one coordinate. Initially the wind components were chosen to be zero.

The wind components at the lower boundary (90 km) were also assumed to be zero. The vertical gradients of the wind components were set to zero at the upper boundary (450 km).

Heaps plotted his results as contour diagrams of the neutral zonal and meridional components as a function of latitude and altitude for several times. These diagrams were scaled and the results replotted in the more frequently used speed versus height and wind direction versus height format. This was done for two different times and for several distances from the latitudinal peak of the assumed electric field. For 18 hours magnetic time these results are shown in Figures 3.6(a and b).

In these figures, the speed profiles were normalized by the greatest magnitude, U_{max}, which is given with each speed profile. The model electric field strength at this time is $\simeq$20 mv m^{-1}. The integration procedure began at 17 hours or one hour prior to the time of the diagrams so that the chosen initial conditions may still have a significant effect on the solution. The wind system is symmetric in latitude about the peak. One feature of these diagrams which deserves attention is the lack of northward turning of the wind direction at low altitudes which may be caused by viscosity. The results of these calculations for 23 hours magnetic time are shown in Figures 3.7 (a to d) for 0, 100, 250 and 500 km distance from the latitudinal peak of the electric field. The speed profiles are basically similar to those of 18 hours but the peak speeds are much larger as a result of the increased electric field strength. Here a northward turning of the wind direction is apparent only at the outer edges of the electric field distribution (again the wind system is symmetric). The reason for this lack of turning is not explained by Heaps.

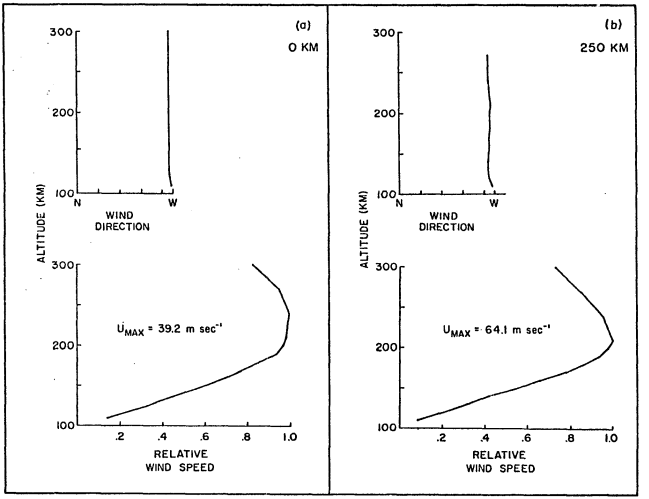

Figure 3.6 Heaps' (1972) model of ion-drag winds at 18 hours magnetic time for 0 and 250 km distance north or south of the center of the assumed electric field distribution. U_{MAX} is the peak wind speed.

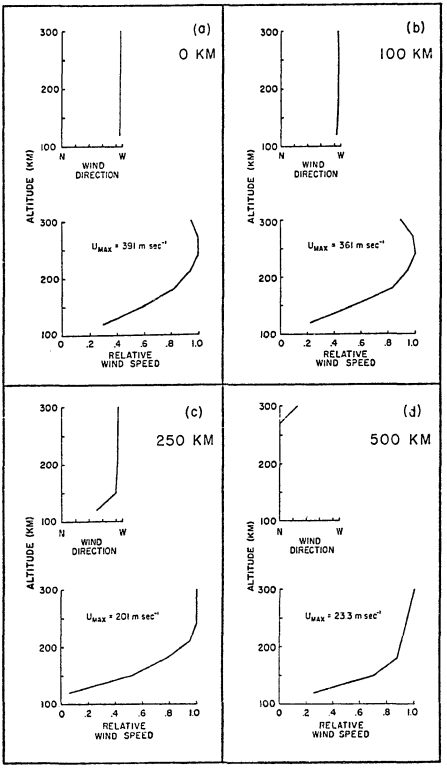

Figure 3.7 Heaps' (1972) model of ion-drag winds at 23 hours magnetic time for four distances north or south of the center of the assumed electric field distribution: (a) 0 km, (b) 100 km, (c) 250 km, and (d) 500 km.

3.4 MODELS OF THERMOSPHERIC WINDS GENERATED BY AURORAL HEATING

A second possibly large source of energy in the high-latitude thermosphere is auroral heating. It was demonstrated in Chapter 2 that the predominant source of auroral heating is dissipation of the auroral electrojets. The heating rate due to this dissipation exceeds the heating due to absorption of solar EUV radiation. Significant perturbations of the thermospheric pressure distributions can be expected to be generated. Two models of the winds generated by these pressure distributions have been published, and are examined here.

Vest's Model of Meridional Winds

Vest (1973) assumed that the high-latitude heat input to the auroral thermosphere could be expressed as the sum of heat inputs from two particle sources: a discrete flux in the oval and a diffuse flux centered equatorward of the oval. Both of these fluxes were given a 5 to 1 diurnal variation to correspond with the observations of Sharp and Johnson (1968) and Feldstein and Starkov (1971). The heat input from discrete fluxes in the oval were approximated by a function having maximum amplitude $1.12\ \Delta H \times 10^{-3}$ Joules m^{-2} sec^{-1} at 22 hours where the magnetic perturbation (ΔH) is expressed in nT. This heat input was apparently supplied evenly in an oval of 10° width centered at 70° latitude. The heat input from the diffuse flux was distributed uniformly over the latitudes $65 \pm 10°$ and had a maximum of 7.5×10^{-4} Joules m^{-2} sec^{-1} at 08 hours. The total heat input over the globe from this diffuse flux was 9×10^{9} Joules sec^{-1}. The altitude dependence of the heating was taken to have a shape approximating that of the H_{α} excitation profile as calculated by Eather (1967).

In his calculations Vest ignored Joule heating as well as the ion-drag term in the neutral equation of motion. However, Vest performed his calculations using H = 500 nT. Thus, the auroral oval heating was 2.5×10^{-2} Joules m^{-2} sec. According to the estimates presented in Chapter 2, this is a reasonable estimate for auroral oval heating during conditions of substantial auroral activity, even though the source of the heat may be incorrectly ascribed. More serious is neglect of the ion-drag term, which overestimates the daytime winds. The results of Vest's calculations for a 500 nT disturbance were presented as Figure 3.3b. While the details of the method of solution used by Vest are not reviewed here, it is important to note that the solutions presented are steady-state solutions. Specifically, Vest's heat inputs are assumed to be present continuously, and the computation was continued until the solution converged.

The influence of auroral heating is clearly evident at 140 and 180 km, but not at 300 km. The perturbation of the tidal wind field on the equatorward side of the oval (60°), is such that equatorward meridional winds predominate during the night and reach 375 m sec^{-1} at 02 hours and 180 km. On the poleward side of Vest's oval (at 80°), nighttime meridional speeds are predicted to be nearly zero at both 140 and 180 km, probably due to the removal of the diurnal heating pressure-gradient by auroral heating. The result at high latitudes (80°) is a zonal eastward wind throughout the night. At high latitudes, only the winds above the pole are relatively unperturbed. At an auroral zone latitude (70°), small changes are seen. In the evening at 180 km, auroral heating apparently causes an increase in the equatorward meridional component, while the winds at 02

and 04 hours have their zonal components reversed to westward. At 140 km, the effects of auroral heating are clearly dominant above 60° latitude and only result in minor perturbations equatorward of 50°. Significant perturbations appear to be associated with auroral heating at both 140 and 180 km in low latitudes (10 to 30°). These changes are not explained.

The principal facets of Vest's model may be correct, in spite of the obvious difficulty caused by the neglect of the ion-drag term and possible deficiencies in the assumed heating functions. Between 140 and at least 180 km strong equatorward winds are predicted, during the night, equatorward of the auroral oval. Corresponding poleward winds do not appear on the poleward side of the oval. The meridional component predicted by Vest cannot account for the observation of large (300 m sec^{-1}) F-region equatorward winds by Hays and Roble (1971a) at midlatitudes or the similar observation of Smith (1968) in which a peak wind speed of 230 m sec^{-1} was found in a TMA release at 150 km over Hawaii.

If Vest's calculations are correct, then only small, aurorally associated, perturbations should appear in observations of the meridional winds made above 200 km. The predicted temperature perturbation due to auroral heating is small at 200 km (5%) and decreases rapidly above 200 km. Wind observations made above 200 km are, therefore, expected to show principally the unperturbed tidal motion.

Heaps' Model of Meridional Wind Perturbations

Heaps also calculated a model of the wind perturbations resulting from pressure-gradients generated by Joule dissipation. The electric field distribution employed was the same as that used in the ion-drag wind model discussed previously and the conductivities employed were

independent of the coordinates and time. A crude approximation to the Joule heating results. Integrating Heaps' profile of the Joule heating over altitude at 23 hours magnetic time (the time of maximum electric field strength), the Joule heat is found to be 4.5×10^{-3} Joules m^{-2} sec^{-1}, which is comparable to the estimate made in Chapter 2 for moderate auroral activity.

Figure 3.8 illustrates Heaps' solution for the thermospheric response to Joule heating. The winds illustrated are predicted for 23 hours magnetic time. The heating produces a vertical (upward) motion (maximum 7 m sec^{-1}) and meridional winds up to 30 m sec^{-1}. The zonal winds (maximum 15 m sec^{-1}) result from the action of the Coriolis force -the ion-drag term was ignored for this model. The maximum pressure disturbance at 23 hours is 7.2% of the unperturbed pressure and appears at 240 km altitude in the center of the heated region. The maximum temperature and pressure perturbations are found to occur approximately 3 hours after the maximum in the electric field strength.

Heaps also added the ion-drag generated winds to the heating winds to produce a model of the wind field which should result from the application of an electric field to the thermosphere. The resulting motions are shown in Figure 3.9. The Coriolis force and the large zonal motion modify the meridional winds produced by the heating. The wind field is asymmetric with higher meridional wind speeds in the poleward part of the assumed "electric field oval". The maximum meridional speed is predicted to be only 60 m sec^{-1}. The maximum temperature and pressure perturbations are predicted to occur approximately 3 hours after the maximum in the electric field strength.

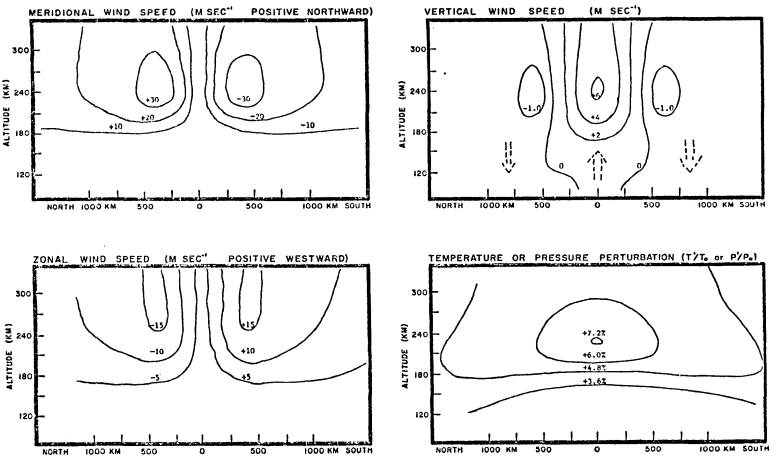

Figure 3.8 Meridional, zonal and vertical winds and the temperature/pressure perturbations at 23 hours magnetic time predicted by Heaps (1972) for auroral heating. The ordinate is the distance from the center of the assumed electric field distribution.

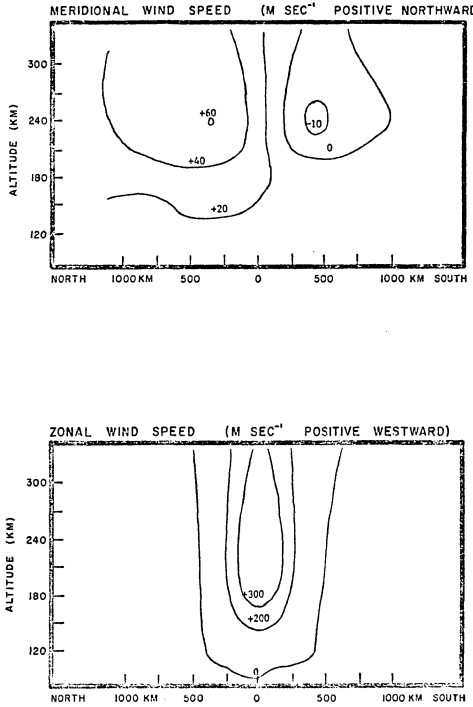

Figure 3.9 Combined heating and ion-drag wind field at 23 hours magnetic time. After Heaps (1972).

In summary, Heaps' combined model predicts rather small meridional perturbations to the tidal wind system, but substantial zonal perturbations. The largest meridional perturbations (60 m sec^{-1}) are predicted to occur above 200 km approximately 250 km north of the center of the assumed electric field distribution. A substantial fraction of this peak perturbation is predicted to occur more than 1000 km north of the center of the electric field distribution. Equatorward of the electric field distribution, the predicted perturbation of the meridional winds are very small (10 m sec^{-1}). Heaps' predicted perturbations of the zonal wind are in substantial agreement with the model of Fedder and Banks, but the meridional perturbations predicted do not agree with Vest's model. There is therefore a basic disagreement between these two models.

3.5 SUMMARY OF THERMOSPHERIC WIND MODELS

Table 3.1 presents a summary of the assumptions of the models which have been discussed in this chapter, the altitude range in which they are intended to apply, and the principal characteristics of the modeled winds which are of interest subsequently in this study.

TABLE 3.1

SUMMARY OF TIDAL AND HIGH LATITUDE WIND MODELS

	TERMS RETAINED IN THE EQUATION OF MOTION $\frac{\partial \vec{U}}{\partial t} = -(\vec{U}\cdot\nabla)\vec{U} - 2\vec{\Omega}\times\vec{U} - \frac{1}{\rho}\nabla p + \frac{\mu}{\rho}\nabla^2\vec{U} + \nu_{ni}(\vec{V}_\perp - \vec{U}_\perp)$					ALTITUDE RANGE
TIDAL MODELS						
Challinor (1970a)	yes	yes	E	no	yes[1]	250 km
Kohl (1970)	?	yes?	E	?	yes	400 km
Vest (1973)	yes	yes	A	yes	no	140-300 km
ION-DRAG MODELS						
Fedder and Banks (1972)	no	no	no	yes	yes[2]	100-350 km
Heaps (1972)	yes	yes	A	yes	yes[3]	100-360 km
AURORAL HEATING MODELS						
Vest (1973)	yes	yes	A[4]	yes	no	140-300 km
Heaps (1972)	yes	yes	A	yes	yes[3,5]	100-360 km
COMBINED AURORAL HEATING AND ION-DRAG MODEL						
Heaps (1972)	yes	yes	A	yes	yes[3]	100-360 km
TERMS	nonlin.	Cor.	pres. grad.	visc.	ion-drag	

SYMBOLS A - Analytic model
E - Empirical model based on Jacchia and Slowey (1967)

NOTES 1. Ion motion determined from Electric field derived from Sq magnetic variation.

2. Ion motion determined from a local model of the electric field in the polar cap.

TABLE 3.1 (continued)

GEOMETRY	DIMENSIONS	PRINCIPAL FEATURES
spherical	2	Produces a global wind system. Motions are from the subsolar latitude and 1400 LT to the antisolar latitude and 0330 LT. These motions are equatorward at night and poleward during day. At auroral-zone latitudes they are eastward in evening and westward in morning hours.
spherical	2	
spherical	2	(overestimates daytime winds)
cartesian	2	Produces winds of magnitude E/B in $\hat{E} \times \hat{B}$ direction in the F-region and smaller winds turning to the direction of E in the E region.
cartesian	3	Same as Fedder and Banks' model except that Coriolis force produces small motions in the direction of E in the F region.
spherical	2	Strong (200 m/sec) equatorward meridional winds produced on equatorward side of heated region, weaker (30 m/sec) poleward motions produced on poleward side.
cartesian	3	Weak, symmetric winds (30 m/sec) produced on both sides of heated region.
cartesian	3	Strong zonal motion (300 m/sec) produced by north-south electric fields and weak meridional winds produced by heating.

3. An auroral zone electric field distribution is assumed which drives both ion motion and currents which heat the thermosphere.

4. Auroral zone thermosphere heated by particle precipitation which produces a pressure perturbation.

5. Ion-drag is included only as a frictional force in this model.

CHAPTER 4

OBSERVATIONS OF THE MERIDIONAL WIND COMPONENT

The models reviewed in the last chapter suggest that the tidal wind field is always present at all latitudes and that auroral heating and electric fields can produce perturbations of this wind field at high latitudes. The perturbations produced by auroral heating are predicted by both Heaps (1972) and Vest (1973) to be primarily meridional in nature. The observed morphology of auroral-zone electric fields suggests that perturbations produced by the ion-drag mechanism in the F-region wind field are in the zonal directions. It appears profitable, then, to resolve observations of the high-latitude wind field into zonal and meridional components. Accordingly, the next chapter is devoted to an examination of the zonal component while the meridional component observations are examined in this chapter. Resolution of the observed winds into zonal and meridional components is made in a geomagnetic frame as it is in this frame that auroral and geomagnetic phenomena are best ordered.

There are several mechanisms which can produce meridional winds at auroral-zone latitudes. Besides auroral heating and tidal winds, which have been discussed, there are two separate ion-drag mechanisms. Fedder and Banks (1972) applied their model to the polar-cap where the dawn-to-dusk electric field produces dayside to nightside winds. These winds may penetrate to auroral-zone latitudes and be observed. Additionally, an east-west component of an electric field, if present in the auroral-zone thermosphere for sufficiently long periods, could produce observable meridional winds. Examination of the meridional component of wind

observations is made with these possible driving mechanisms in mind.

4.1 METHODS AND ERRORS OF OBSERVATION

Two collections of data are available for examination of the meridional wind component: a considerable number of barium releases and interferometric Doppler observations of auroral 6300A emissions (from 160 to 350 km, see Appendix C). A brief discussion of the errors of wind determinations by release techniques is presented in Chapter 5, where these data are more extensively employed. The present analysis is primarily based upon Doppler wind measurements acquired with the University of Michigan Fabry-Perot Interferometer, obtained during the late winter and spring of 1972. Instrumental parameters and most of the pertinent details of the data reduction techniques are given by Hays and Roble (1971b). Reduction of the data employed here was performed by personnel of the University of Michigan (who kindly provided their data for use in this study). All data were taken at Ester Dome Observatory, near College, Alaska, during clear nights when the moon was down or was sufficiently small that background continuum posed no problems. Corrections were applied for source intensity variations. For these data, no wavelength reference was used and the Doppler shift was computed from the relative shift of two profiles obtained at azimuths differing by 180°. Measurements were made at the same zenith angle and four different azimuths in succession. Each profile required about 10 minutes of observation. Pairs of Doppler shifts were then used to obtain the zonal and meridional wind components. The possible difficulties of this procedure are examined in Appendix C where the principles of interferometric Doppler measurements are discussed. It is noted that this procedure results in averaging

over spatial gradients so that the observed winds approximate those overhead of the observatory even though observations were commonly made at 45° zenith angle. The estimated error of these measurements is $\pm$ 30 m sec^{-1}, a value representative of the displacement between a zenith profile and the center of the two profiles used to compute the wind components (Meriwether, 1973).

4.2 MEAN TEMPORAL BEHAVIOR OF MERIDIONAL WINDS

The observed meridional wind components as determined from the 6300A interferometric measurements are plotted in Figure 4.1 (a-e) as a function of local time. Poleward motions are plotted upward and equatorward motions are plotted downward. All available data have been plotted even though there are gaps on some nights. Inspection of these histograms suggests that the mean behavior of the observed winds is similar to the temporal behavior predicted for the tidal winds by Challinor (1970a) and Vest (1973). For comparison, the magnitude of the predicted meridional component of Challinor (with amplitude halved) is shown as the curve in Figure 4.1. A brief explanation of the origin of this curve is necessary. Challinor's results were plotted as vectors as a function of latitude and local time (presented as Figure 3.1). These vectors were scaled at 65° latitude (the latitude closest to College) and the geomagnetic zonal and meridional components computed for two stations, College and Kiruna. These computed components are shown in Figure 4.2 for these stations. The geographic zonal and meridional components at the two stations are, of course, identical, but this is not the case when the components are resolved in a geomagnetic frame because the true azimuth of geomagnetic north at the two stations is different. The geomagnetic components at the two

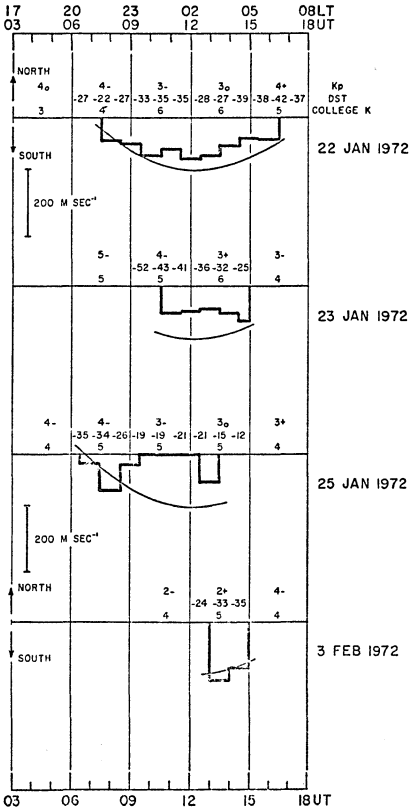

Figure 4.1 (a) Observed magnitudes of the meridional wind component obtained at Ester Dome Observatory by 6300Å interferometry. The curve is the tidal component predicted by Challinor (1970a) with amplitude halved. Values of the K_p, D_{st} (provisional), and K (College) indices are given.

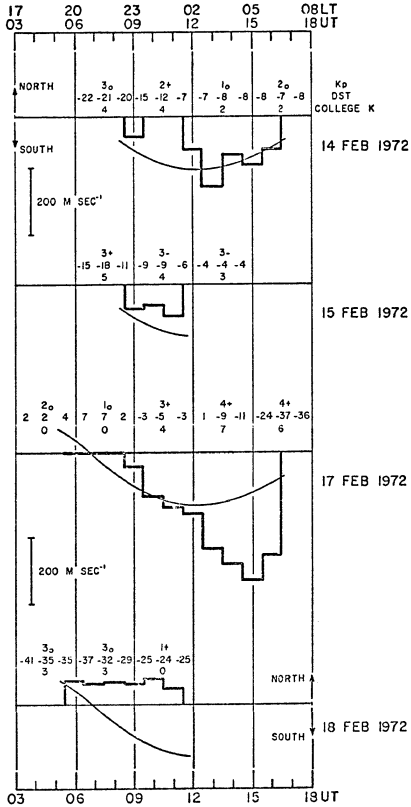

Figure 4.1 (b)

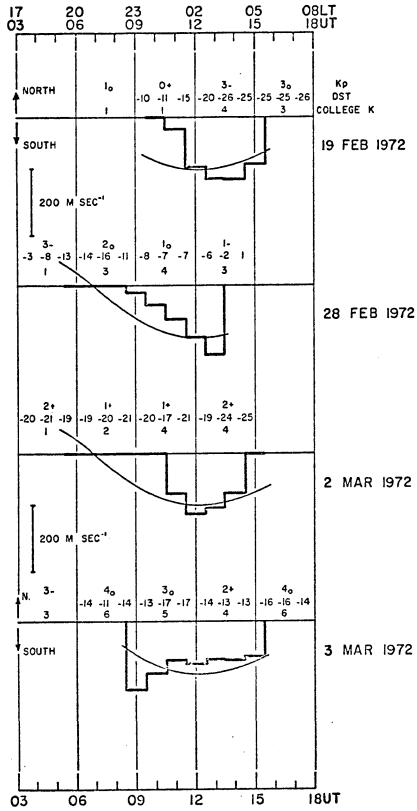

Figure 4.1 (c)

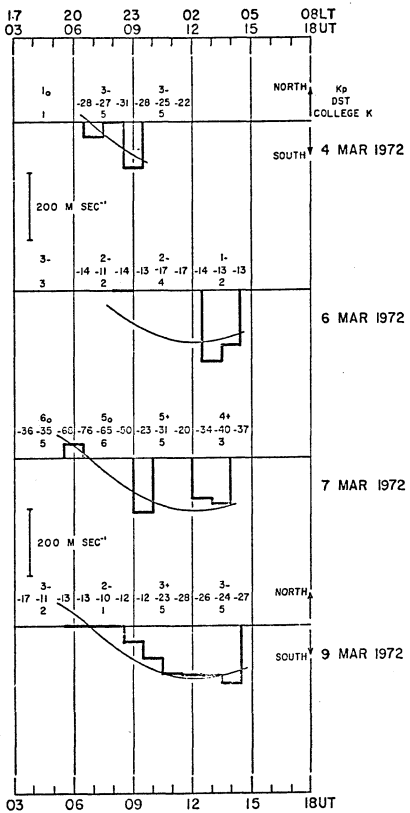

Figure 4.1 (d)

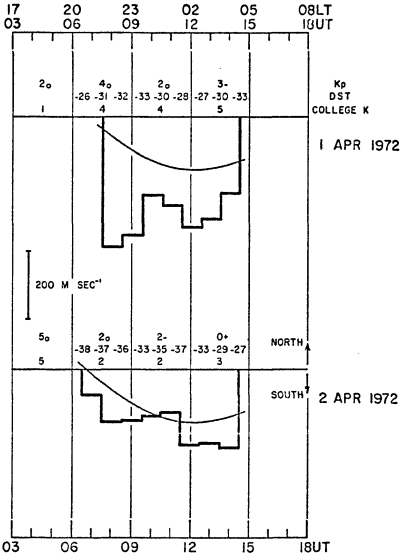

Figure 4.1 (e)

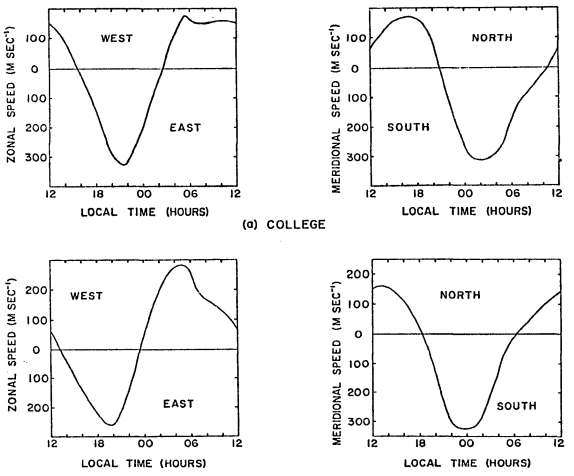

Figure 4.2 Zonal and meridional components of Challinor's tidal model in a geomagnetic frame for (a) College and (b) Kiruna.

stations are basically similar except that Kiruna leads College by two hours. Similarly, the zonal and meridional components from Vest's unheated model for 140, 180 and 300 km are shown in Figure 4.3.

To verify the suggestion that the general behavior of the observed meridional winds is similar to that predicted by the models, the data shown in Figure 4.1 were averaged hour by hour. The resulting mean meridional component is presented in Figure 4.4. Although the sample standard deviations of the measurements are large, the trend of the mean is well defined and closely follows the prediction of Challinor. Actually the curves shown in both Figures 4.1 and 4.4 are Challinor's model with amplitude halved.

In support of this mean behavior of the interferometric data, the motions of several barium releases are considered. Figure 4.5 presents the meridional components of motion of several neutral clouds as a function of local time for releases made from Esrange, Sweden, and Andenes, Norway. The releases are numbered (according to their line number in Table 5.1) and subscripted to indicate different releases from the same rocket. Separation of the releases into three altitude regions is indicated by symbols. The curved line is the meridional component of Challinor for Kiruna with amplitude reduced by a factor 2. The release points are distributed about the curve, and would be unevenly distributed about a curve representing the full amplitude of the meridional component of the tidal models. Assuming the deviations are due to a random process, then the observed behavior is compatible in the mean with a wind field which is identical with the tidal models of Challinor and Vest with half amplitude.

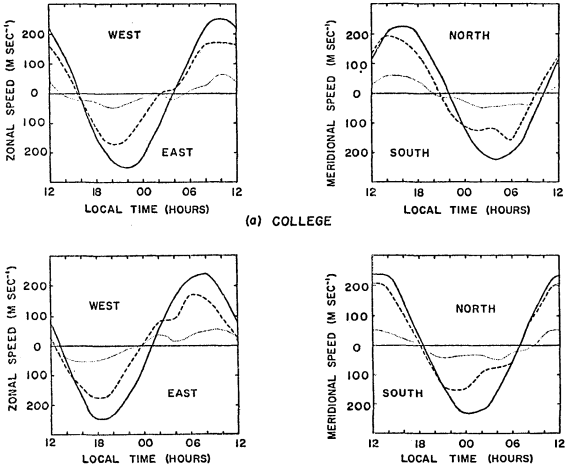

Figure 4.3 Zonal and meridional (geomagnetic) components of the tidal wind field predicted by Vest (1973) without auroral heating for (a) College and (b) Kiruna. The solid, dashed and dotted curves represent the components at 300, 180, and 140 km, respectively.

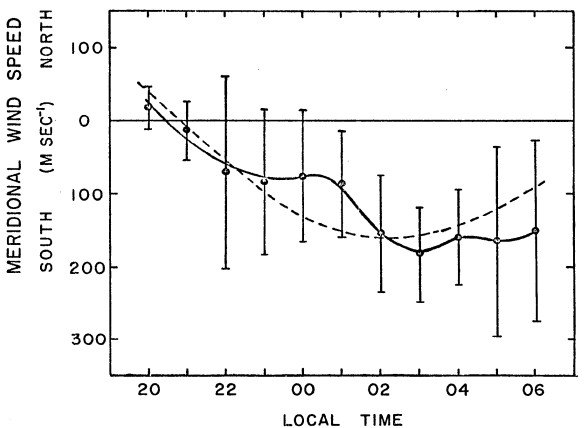

Figure 4.4 Mean and standard deviation of the meridional wind component observations at Ester Dome Observatory as a function of local time. The dashed curve is Challinor's meridional component with amplitude halved.

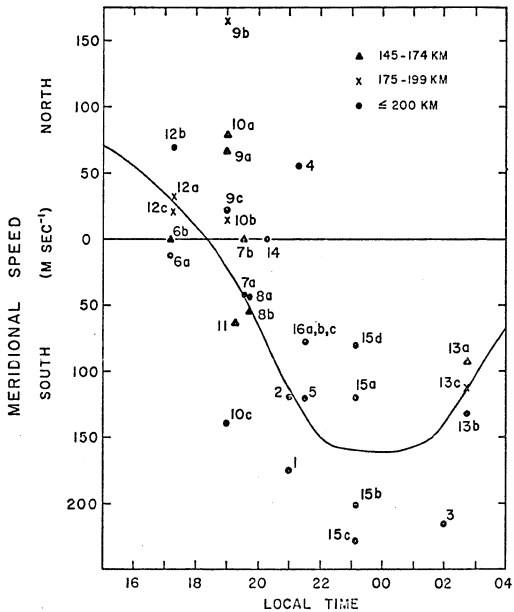

Figure 4.5 Meridional wind components derived from the motions of several barium releases from Esrange and Andenes. The curve is Challinor's predicted meridional component of the tidal wind field with amplitude halved.

Three hypotheses can be advanced to explain the observed, mean, behavior of the high-latitude meridional component. These hypotheses are: (a) the observed meridional winds are not tidal winds but are due entirely to some other force, or (b) the observed meridional winds result from a superposition of the tidal wind field and another wind field, due to a non-tidal force, or (c) the observed winds are, indeed, tidal winds but the existing tidal theories over-estimate the magnitude of the nighttime winds at high latitudes. The first hypothesis (a) implies that the tidal flow is somehow cut off or prevented from reaching auroral-zone latitudes. This modification of the flow pattern would have drastic consequences for the middle-latitude tidal winds. Further, the forces acting at high latitudes must drive winds which are very similar to those predicted by the tidal models: that is, the phase must be identical and the magnitudes of the winds half of the magnitudes predicted by the tidal models. Both of these conditions are very restrictive and improbable. The hypothesis (b) requires a non-tidal wind field which is exactly reversed in phase and has amplitude approximately half of the predicted tidal winds. Since there is about a 3 hour time difference between the local times of magnetic midnight at the two stations, any geomagnetically associated non-tidal winds are unlikely to have both the proper phase and amplitude relationship at the two stations. Hypothesis (b) is therefore unlikely. Hypothesis (c) discussed below, provides a more plausible explanation of the observed behavior.

There exists only one model which predicts poleward motions for a perturbation wind field at auroral latitudes. Heaps' model shows poleward winds of up to 60 m sec^{-1} on the poleward side of the nighttime auroral

oval. However, the present measurements require larger wind speeds, up to 150 m sec^{-1}, and are probably more representative of the equatorward side of the oval. There is therefore no argument in support of hypothesis b.

Both hypotheses a and b require a non-tidal force which, from inspection of the equation of motion, can be only the ion-drag or Coriolis forces. It will be demonstrated in Chapter 5 that the mean zonal wind reverses direction from west to east about 02 hours LT and that the zonal wind is primarily driven by horizontal electric fields. Therefore, the observed mean meridional wind component cannot be due to the action of the Coriolis force because the meridional wind would necessarily reverse after 02 hours, not earlier (1830 to 2030 LT depending upon location) as observed. Arguments concerning the ion-drag mechanism are given later in this chapter.

In contrast, the third hypothesis, that the observed winds are tidal winds but the models are in error in their prediction of the magnitudes, can be supported. For the times of the measurements the mean electron density in the polar-cap was 5 times in excess of the density assumed by Challinor. The mean electron density computed from the Resolute Bay, Canada, (84.3° N geomagnetic latitude) ionospheric soundings of f_oF_2 was 3×10^{11} m^{-3}. This electron density is not at all atypical of the density at the F_2 peak measured at Resolute Bay for the four months of the measurements (Challinor, 1970b). Additionally, the height of the F_2 peak was generally in the range 250 to 300 km, and therefore these measurements can be compared to Challinor's assumptions directly. The magnitude of the ion-drag term in the polar-cap must therefore be greater than in Challinor's

model and a speed reduction result for the polar-cap tidal winds. The effect of the increased ion-drag in the polar-cap at auroral-zone latitudes is difficult to estimate because of other possible forces in or near the auroral-zone. Assuming that no other forces are present, the effect of an increased ion density in the polar-cap must be a reduction of the tidal wind speeds in the nightside auroral zone through the advective term (an inertial effect). Furthermore, it is very likely that the average electron density in the auroral zone is higher than assumed by Challinor. Between 22 hours and 05 hours (LT) Challinor's assumed electron density is just in excess of 10^{11} m^{-3}. If the actual electron density were higher, then the ion-drag force in the auroral zone would be increased. The increased electron density in the polar-cap and the probable increase in electron density in the auroral zone both act to reduce the tidal wind speeds. The assumption is therefore made that the mean observed meridional component in the auroral-zone thermosphere can be described by the tidal models of Challinor (1970a), Kohl (1970) and Vest (1973) with the magnitude of the meridional speed reduced by a factor of two at all local times.

4.3 CORRELATION OF MERIDIONAL WINDS WITH VARIOUS INDICES

It is obvious from inspection of Figures 4.1 and 4.5 that there are substantial deviations of the observed meridional winds from their mean temporal behavior. In an attempt to determine the cause of these deviations, visual correlation is made with several indices. Figure 4.1 includes values of the (College) K index (Townshend, 1972), (provisional) Dst index (Sugiura and Poros, 1972), and K_p index (Lincoln, 1972). Even cursory inspection shows that there is no direct correlation between the K_p index and either the magnitude of the observed meridional winds

or the deviations of these winds from their mean behavior. Similar conclusions are reached when the College K index and f_oF_2 values in the polar cap (Resolute Bay, Canada) are used for correlation instead of K_p. There is no correlation with the sign of the ΔD magnetic disturbance observed at College with the winds or their deviations from the mean. Since K_p is a quasi-logarithmic measure, albeit a poor one, of the magnitude of the auroral electrojet currents (Rostoker, 1972), K_p can be used as a crude measure of the global auroral heating rate: as Cole (1971) predicts auroral heating is proportional to the square of the Hall current magnitude. A lack of correlation may imply that K_p is not a good measure of the global heating. The College K index, in the same way, may provide a measure of the local heating rate. Local heating will probably not affect local pressure-gradients substantially, but may produce significant pressure-gradient changes on the poleward and equatorward edges of the heated region. Any perturbation of meridional winds by local heating should therefore be to reduce the speed in the heated region because the pressure-gradient changes will be such as to oppose the tidal winds. As has already been discussed, the Resolute Bay f_oF_2 values reflect changes in the magnitude of the ion-drag force in the polar cap. These changes apparently are not seen in the interferometric observations. Lastly, the ΔD magnetic perturbation is caused, in part, by north-south currents resulting from east-west electric fields. The lack of correlation of the wind deviations is weak support for the suggestion that electric fields are not responsible for meridional winds in the auroral zone.

While the deviations of the observed meridional winds from their mean behavior do not correlate with the K_p and K indices, there is possibly

some correlation with changes in these indices. The net deviation of the observed meridional winds from the (modified) tidal model in each three-hour interval is classified as being in excess of the model speed, less than the model speed, or approximating the model speed. At least two hours of data must be present in each three-hour interval or the data is discarded. The number of three-hour intervals in which these classes are observed is tabulated in Table 4.1 (a). Separation of these events is made upon the basis of increased, decreased or stationary values of K_p from the preceeding interval. Table 4.1 (b) presents a similar analysis based upon local K rather than K_p. There is insufficient data available to allow application of a statistical (χ^2) test to determine if the deviations from the modified model are correlated with the changes of K_p and local K. In the absence of additional data, all that is possible is to show that the tendencies indicated in Tables 4.1 (a) and (b) are physically plausible. Inspection of the vertical columns shows that:

1. in 56% of the events in which K_p increased the observed meridional winds exceeded the speed predicted by the model,
2. in 56% of the events in which K_p decreased the observed meridional winds were less than predicted,
3. in 53% of the events in which local K increased the observed winds were less than predicted, and
4. in 83% of the events in which K decreased the observed winds exceeded those predicted by the modified model.

These observations are consistent with the suggestions that K_p gives a measure of the global auroral heating, and pressure disturbance which tends to increase the equatorward wind component, while local K is a

TABLE 4.1 (a)

THE NUMBER OF THREE-HOUR INTERVALS IN WHICH THE NET DEVIATION OF THE MERIDIONAL WINDS OBSERVED BY THE 6300A INTERFEROMETER AT ESTER DOME OBSERVATORY WERE IN EXCESS OF, OR SLOWER THAN, OR APPROXIMATELY EQUAL TO THE MODIFIED TIDAL MODEL (CHALLINOR, 1970a, WITH AMPLITUDE HALVED) VERSUS THE CHANGE IN K_p INDEX FROM THE PRECEDING INTERVAL.

MERIDIONAL WINDS	K_p INCREASED	K_p DECREASED	NO CHANGE
EXCEED MODEL	5	6	1
LESS THAN MODEL	2	10	1
APPROXIMATE MODEL	2	2	0

TABLE 4.1 (b)

THE NUMBER OF THREE-HOUR INTERVALS IN WHICH THE NET DEVIATION OF THE OBSERVED MERIDIONAL WINDS WERE IN EXCESS OF, OR SLOWER THAN, OR APPROXIMATELY EQUAL TO THE MODIFIED TIDAL MODEL (CHALLINOR, 1970a, WITH AMPLITUDE HALVED) VERSUS THE CHANGE IN COLLEGE K INDEX FROM THE PRECEDING INTERVAL.

MERIDIONAL WINDS	K INCREASED	K DECREASED	NO CHANGE
EXCEED MODEL	6	5	1
LESS THAN MODEL	9	0	4
APPROXIMATE MODEL	2	1	1

measure of the local heating which produces pressure-gradients opposing the equatorward winds.

4.4 DEVIATIONS OF THE MERIDIONAL WINDS FROM THEIR MEAN BEHAVIOR

On a statistical basis deviations of the observed meridional winds from their mean behavior appear to be associated with auroral heating in the electrojets. However, the magnitude of the observed deviations greatly exceeds those predicted by the models of Heaps (1972) and Vest (1973). Increased heating should increase the magnitude of the auroral-zone pressure perturbation and result in larger wind perturbations. However the heating rates assumed by Heaps and by Vest are in substantial agreement with the estimates made earlier (in Chapter 2) and there is no reason to suppose that heating will be substantially larger except during major magnetic storms. It is, therefore, not clear that the observed deviations are due to auroral heating. Since the statistical analysis is inconclusive, examination is made of individual nights of data.

Four nights of data were chosen for detailed analysis, three of which show major departures from the mean meridional behavior curve and one which shows only minor deviations in spite of a large substorm. The nights chosen are February 17, and 18, March 7, and April 1, 1972. Selection of these nights is partially based upon the availability of other data. For each of these nights the all-sky camera pictures from Inuvik, NWT; Fort Yukon; and College were scaled every 10 minutes to determine the latitudinal extent of visual aurora as a function of time. Crude estimates of the auroral brightness were also made from the pictures. From these data, latitude-time plots of the auroral extent for the four nights are drawn and presented as Figures 4.6a, 4.7a 4.8a and 4.9a for

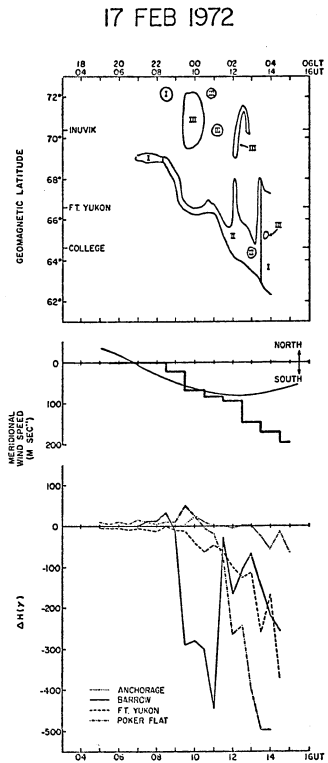

Figure 4.6 (a) The latitude-local time distribution of aurora during the night of February 17, 1972 (UT). (b) Observed meridional wind component with curve representing the modified tidal model. (c) The magnitude of the H component magnetic perturbation measured at Barrow, Fort Yukon, Poker Flat, and Anchorage.

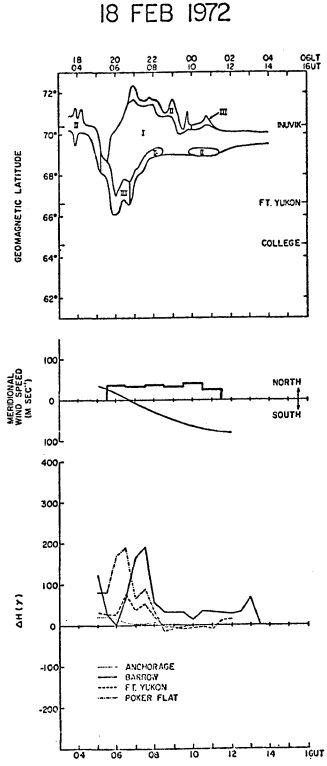

Figure 4.7 (a) The latitude-local time distribution of aurora during the night of February 18, 1972 (UT). (b) Observed meridional wind component with curve representing the modified tidal model. (c) The magnitude of the H component magnetic perturbation measured at Barrow, Fort Yukon, Poker Flat, and Anchorage.

7 MAR 1972

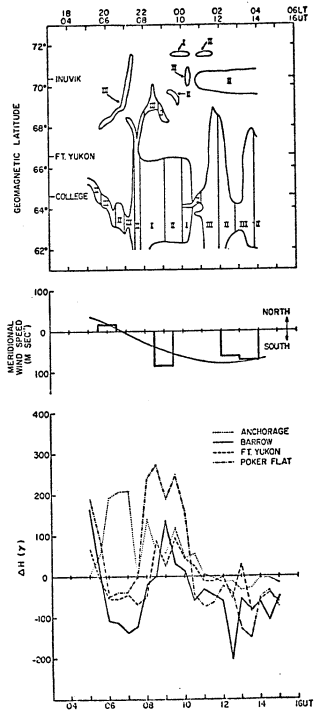

Figure 4.8 (a) The latitude-local time distribution of aurora during the night of March 7, 1972 (UT). (b) Observed meridional wind component with curve representing the modified tidal model. (c) The magnitude of the H component magnetic perturbation measured at Barrow, Fort Yukon, Poker Flat, and Anchorage.

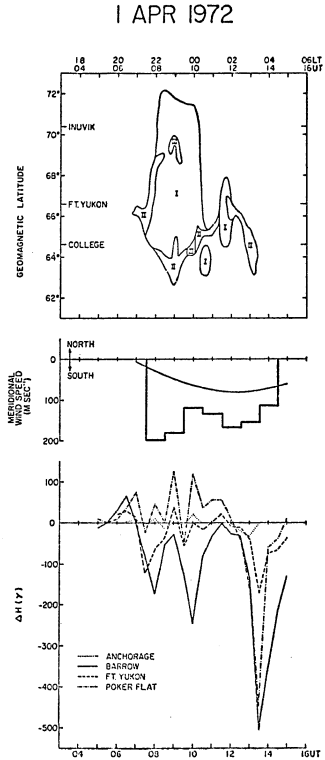

Figure 4.9 (a) The latitude-local time distribution of aurora during the night of April 1, 1972 (UT). (b) Observed meridional wind component with curve representing the modified tidal model. (c) The magnitude of the H component magnetic perturbation measured at Barrow, Fort Yukon, Poker Flat, and Anchorage.

the nights of February 17, 18 March 7 and April 1, respectively. The Roman numerals I, II, and III indicate a subjective estimate of the auroral intensities in the ranges <2kR, 2 to 20kR, and >20kR, respectively. Also shown on each figure are the measured meridional wind components (in part b) and a plot of the ΔH magnetic perturbations recorded at Barrow, Fort Yukon, Poker Flat and Anchorage (in part c). Scalings of the magnetic records were made every half hour.

The course of auroral development is normal for the three nights February 17, 18, and March 7. That is, there is a more or less steady equatorward motion of the aurora in the pre-break up hours which is followed by one or more substorms. This same development is not seen on April 1st., probably due to increased oval size at the time twilight first permits all-sky camera observations. In general, the strength of the magnetic perturbation is roughly correlated with the brightness of the aurora.

During the night of February 17 (UT date) the observed meridional winds speed was initially zero for the three hours beginning at 20 hours local time (LT) and then increased monotonically through the observing period. Equatorward meridional speeds were observed to approach 400 m sec^{-1} at 05 hours LT. A small equatorward wind was observed at Ester Dome Observatory about 23 hours LT, at which time the apparent rate of equatorward motion of the aurora terminated about 2330 LT coincident with the appearance of bright auroral overhead at Inuvik and a marked negative bay at Barrow. Overhead aurora was present at Ester Dome Observatory from 0130 LT onwards. The beginning of the negative bay was first detected at Poker Flat Range about this same time. On this night

the equatorward meridional wind speed increases in a fashion similar to the time integral of the magnetic perturbation.

Unusual meridional winds were observed on February 18 (UT date): instead of reversing prior to 21 hours LT, the meridional wind remained poleward through the observing period. The poleward speed was approximately 40 m sec^{-1}. Auroral activity occurred early and decreased after 21 hours LT. An apparent break up occurred at the latitude of Fort Yukon at approximately 20 hours LT. The winds during this night appear to be unrelated to the auroral and magnetic activity.

March 7 (UT date) is characterized by winds approximating the modified model and by considerable particle precipitation throughout the night. The latitudinal extent of the visual aurora was great and was well south of 62° geomagnetic latitude during two extended intervals. Only weak negative bays were observed during the night except for a very brief (15 min) 400γ bay at College beginning about 2115 LT. Substantial positive bays were observed at Anchorage and Poker Flat Range, exceeding 200γ. The magnetic activity at Poker Flat is consistently as great or greater than elsewhere. If anything, the observations of this night support a suggestion that local heating is relatively unimportant for the production of significant perturbations of the meridional winds.

Widespread aurora, although generally weaker in intensity, is also characteristic of the premidnight hours on April 1st (UT date). The meridional wind component was considerably greater than its mean behavior throughout the night. Magnetic perturbations measured at Poker Flat Range and Fort Yukon were small. More substantial negative bays were observed at Barrow: 175γ at 22 hours LT, 250γ at 00 hours LT, and 500γ at 0330 LT.

The maximum magnetic perturbation measured at Anchorage was -35γ. Clearly much of the heating occurred North of Ester Dome so that the wind observations are consistent with increased pressure-gradients on the equatorward side of the heated region resulting in increased equatorward winds over Ester Dome.

In summary, study of auroral and magnetic activity during four nights lends support to the suggestion that deviations of the meridional wind component are associated with heating of the thermosphere by the dissipation of the auroral electrojets. On February 17 and April 1, the bulk of the electrojet current was well poleward of Ester Dome. The increased meridional (equatorward) winds observed on these nights are consistent with increased pressure-gradients poleward of the observing station. In contrast, local heating such as is present on March 7 does not produce large deviations in the meridional winds. The meridional winds observed on February 18 are unusual. The bulk of the electrojet current and particle precipitation occurred well poleward of the observing station and receded poleward during the wind observations. Increased equatorward winds should have been observed instead of the poleward winds which were measured. Magnetic and auroral activity declined during the times of the February 18 observations following the magnetic storm of February 17 (maximum K_p =5, and K (College) = 7. No explanation of the poleward winds observed on February 18 can be offered without more data of a similar nature so that a pattern of activity can be established for these poleward wind events. However, it appears that the only distinguishing characteristic of this night is the decline of magnetic activity, which may be related to the source of the poleward winds. Heaps' model at late

magnetic times, when the electric field strength is declining, show poleward motions well to the equatorward side of the center of the electric field regions. These poleward winds are however very small (20 m sec^{-1}). It is also noted the DeVries (1972) observed a relative pressure minimum over the auroral zone during the declining phase of a major magnetic storm. If a pressure distribution such as measured by DeVries occurred on this night, the meridional wind behavior of February 18 would present no problem as it could be driven by the pressure-gradient force.

Besides auroral heating, which produces pressure-gradients changes, there are two other factors which could alter the magnitude of meridional winds: the Coriolis force and the ion-drag force. The Coriolis force coupled with large zonal wind speeds could result in deviations of the meridional winds from their mean temporal behavior. Inspection of the zonal wind component (to be examined in Chapter 5) shows that changes in the zonal speed are not correlated with changes in the meridional speed. Therefore, the Coriolis force is not important for producing perturbations in the meridional winds. The ion-drag force can accelerate or decelerate meridional winds. In the absence of a substantial east-west electric field component, ion-drag will act to reduce meridional speeds in the auroral zone. When substantial east-west electric fields are present, the meridional winds speeds will be reduced or increased depending upon the direction of the electric field. For an abrupt and sustained change in the ion density, or the electric field component in the east-west direction, or both, the response of the thermosphere is characterized by a time constant, previously estimated (in Chapter 2), of approximating 2.5 hours. Evidence is presented in Chapter 5 suggesting that for the

events under study this time is too long and that 1.5 hours is perhaps a better estimate. Thus it should be possible to differentiate between speed changes caused by ion-drag or by heating, for which the thermospheric response time is approximately 3 hours (Heaps, 1972), on the basis of the apparent temporal dependence of the meridional wind deviations. For the most part, the Ester Dome interferometric observations of the meridional wind component show only slow variations. Notable exceptions occur at 02 hours LT on February 14 and 23 hours LT on March 4. Thus these observations of the meridional wind component are consistent with the presence of perturbations in the global pressure distribution generated by auroral heating. These pressure perturbations modify the tidal winds substantially and can produce increased or reduced equatorward wind speeds.

4.5 THE SOURCES OF MERIDIONAL WINDS

It has been shown that the observations of the meridional wind component are compatible with a basic, underlying tidal motion of the thermosphere which is perturbed by the presence of auroral heating at high latitudes. The tidal motion can be seen only in the mean because of the presence of large perturbations. These perturbations are probably correlated with changes of the geomagnetic K_p and K (local) indices indicating that the perturbations may be caused by auroral heating generated by dissipation in the auroral electrojets. Examination of the positions of the visual aurora and the electrojet currents (as indicated by measurements of the ΔH magnetic perturbation) indicate that the observed magnitude of the meridional wind perturbations depend upon the position of the electrojet with respect to the station where the wind observations are made. When the electrojet is located well poleward of the

station, enhanced equatorward wind speeds are observed. When the electrojet is located nearly overhead of the observing station, meridional speeds are reduced. Finally, it is demonstrated that the meridional wind perturbations are not due to the Coriolis force. The east-west electric field could be the cause of the observed meridional wind perturbations through the ion-drag mechanism. However, the lack of correlation with the sign of the D component magnetic perturbation and the slow temporal changes in speed suggest that heating rather than ion-drag is responsible for the deviations of the meridional winds. Apparently, then, the observations of the thermospheric meridional winds are in qualitative agreement with theory: that is, the tidal wind field is present and is perturbed by pressure-gradient winds generated by auroral heating. However, the magnitudes of the perturbations are not well predicted by the models.

Fedder and Banks (1972) model suggests that, in the polar cap, the dawn-to-dusk electric field and the ion-drag force should produce dayside to nightside winds. If the electric field has been steady for at least 2 time constants (there is no measure of the time constant in the polar cap; Fedder and Banks estimate that it is about 1 hour in the F-region), then on the low-latitude side of the polar cap these winds should have an equatorward meridional wind component with a cosine time dependence and a maximum at midnight. If the electric field is not steady or has just been "turned on" then, in the midnight sector, rapidly changing speeds can be expected. The electric field in the polar cap is frequently measured to have a strength in excess of 30 mv m^{-1} (Heppner, 1972c) which can result in wind speeds of the order of 600 m sec^{-1}. The Coriolis force, which was neglected in Fedder and Banks calculations, will shift the time

of maximum meridional winds somewhat earlier. Because of inertia, these winds should penetrate well into the auroral zone. However, no winds of this description are observed in the College interferometer data. A brief examination of some polar-cap wind measurements is made to shed light on this problem.

Meriwether et al. (1973) report the neutral motions observed for three groups of barium releases from Cape Perry, Canada. These releases were clearly made in the polar cap as the launch site was well to the north of the poleward boundary of the auroral oval (for all Q values). The measured electric fields from the ion cloud motions are approximately dawn-dusk and have strengths in excess of 20 mv m^{-1}. Neutral and ion motions from two groups if these releases are shown in Figure 4.10, one each in the morning and evening hours. The predicted neutral motion of Challinor (1970a) is shown as well. The lower releases of March 7 are in reasonable agreement with Challinor's tidal motion. The upper release of March 7 (altitude 278 km) clearly shows a substantial component of motion in the direction of ion motion. However, the releases of March 8 do not behave in the same way. Neutral motion between 190 and 270 km altitude is clearly in the northeast (geographic) direction while the ion motion and the predicted wind vector of Challinor are eastsoutheast and east, respectively. The large northward component of motion cannot have been driven by the diurnal heating pressure-gradient nor ion-drag. This component of motion is opposite to that expected from the Coriolis force. Apparently there must be some other force present which is affecting the motion of the neutral thermosphere in the polar cap. Additional releases made on March 9 at the same local time as the March 8

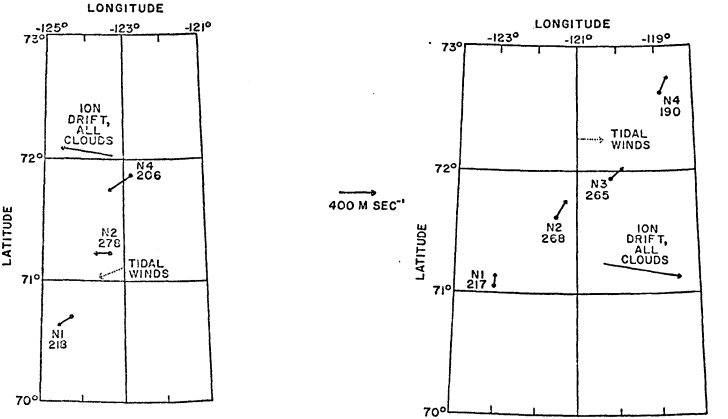

Figure 4.10 Polar cap neutral and ion motions reported by Meriwether et al. (1973) and the predicted tidal winds of Challinor (1970a). Geographic coordinates are used.

releases behave very similarly to the March 8 releases.

It is apparent that ion-drag does not completely dominate the polar-cap neutral thermospheric motion and that some other force must provide the poleward components of motion reported by Meriwether. The direction of the winds observed of March 8 and March 9 is compatible with an additional pressure-gradient generated by auroral heating equatorward of the release location. More measurements are needed in the polar cap in order to determine the relative importance of ion-drag and pressure-gradients in determining the motion of the neutral thermosphere in the polar cap and to determine the influence of auroral heating on the pressure-gradients there.

CHAPTER 5

OBSERVATIONS OF THE ZONAL WIND COMPONENT

According to the theory and models discussed earlier, there are expected to be zonal motions of the high-latitude thermosphere which are driven by the ion-drag force as well as the pressure-gradient force where the pressure-gradients arise from the diurnal heating pressure distribution. Pressure-gradients generated by auroral heating are expected to be aligned in the meridional direction and so should not produce changes in the zonal wind component. (The meridional winds produced were discussed in Chapter 4). Thus, it is anticipated that observations of the zonal winds will show only tidal and ion-drag driven motions. In this chapter, examination is made of wind observations by three techniques as a test of this hypothesis and to determine the relative importance of tidal pressure-gradient and ion-drag forces in determining the high-latitude zonal winds.

5.1 METHODS AND ERRORS OF OBSERVATION

Three collections of data are available for the study of the zonal component of high-latitude thermospheric winds. These collections are the 6300A interferometric observations made at Ester Dome Observatory, Alaska, a small number of TMA trail releases made from Fort Churchill, Canada, and a considerable number of barium releases made from several auroral-zone rocket launch sites. These data are examined separately as the altitudes of measurement are different, as are the errors of measurement. Discussion of the principles and errors of the interferometric observations has been presented previously. Before examining

the observations themselves, the barium and TMA trail release and analysis techniques are considered.

Barium releases are primarily made to study the electric fields present in the high-latitude thermosphere, but permit wind measurements as well. (An extensive examination of release techniques is made in Appendix D). Barium releases form both ion- and atomic- (neutral) clouds which drift independently according to their respective equations of motion and are visible (and can be photographed) because the barium atoms and ions resonantly scatter solar radiation in the visible spectrum. Photographic triangulation is performed to determine the positions of the clouds as a function of time. (Triangulation methods are discussed in Appendix E). Electric fields are inferred from the relative motion of the ion and neutral clouds. Unfortunately, interest in thermospheric winds has not been as great as in electric fields so neutral cloud motion vectors are only occasionally published with corresponding ion motions or electric fields. Because of the primary desire to measure electric fields, the release altitude is chosen sufficiently high that the effect of collisions may be neglected in deriving electric fields from the ion motion. At these altitudes, diffusion is so rapid that observable neutral cloud lifetimes are only 3 to 15 minutes. Asymmetries in cloud geometry, unequal background sky brightness and variations in photographic sensitivity combine to produce triangulation errors from 5 to 10 km (see Wescott et al., 1969, and Appendix E). This triangulation error, coupled with short observation times, and relatively slow neutral motions can produce large errors in the determined wind vectors.

Other phenomena complicate analysis of barium release wind data. The presence of vertical shear in the wind field can substantially distort the shape of the cloud, elongating it in the direction of the shear. If this is not taken into account properly, then substantial errors result for certain geometries of the cloud with respect to the observing sites. Internal atmospheric gravity waves may result in velocity errors unless their presence is recognized and their effects are removed from the data. Furthermore the limited height extent of these releases restricts the range of altitudes over which data are obtained. This limitation can be partially reduced by releasing several clouds at different altitudes, but the rocket trajectories in such experiments are usually tailored to give maximum horizontal spread between the releases for the electric field measurements. It then becomes difficult to separate horizontal- and vertical-gradients.

Many of the wind measurement problems inherent in the barium technique are also common to TMA trail release wind measurements. However there is a considerable advantage in having a continuous trail of released material since wind measurements can be obtained continuously over a range of altitudes. The effects of internal atmospheric gravity waves can be seen and more easily separated from the prevailing winds. The price which must be paid for these benefits is a decreased triangulation accuracy (see Appendix E). Generally the materials released as trails are of lower atomic (or molecular) weight and so diffuse more rapidly than barium, increasing the relative measurement errors still further.

Examination of neutral wind data obtained from barium and TMA releases must be made cautiously so as to avoid pitfalls of the measurement errors. Analysis of these data in this study is based upon the average behavior of several releases and not upon the behavior of individual observations. In most cases, averaging is not actually performed and the data points retain their individual identity. Instead, the data are presented so that the individual and collective behavior are easily seen. Inferences are then drawn from the collective behavior.

5.2 OBSERVATIONS OF ZONAL THERMOSPHERIC WINDS FROM BARIUM RELEASES

Since the barium technique permits measurements of both the neutral wind vector and the ion drift at the release altitude, data from barium releases may be employed to examine the following questions.

1. How important is ion-drag as a driving force for neutral motion at high latitudes?
2. What is the effective time constant for ion-drag acceleration?
3. Is there any relationship between neutral (ion-drag) motion and magnetic activity?

In attempting to answer these questions a number of releases are examined. Table 5.1 lists both neutral- and ion-cloud velocity determinations taken from the literature for 37 high latitude releases, together with supporting data. Geographic coordinates are used, only because this is the original form of most of these data. Launch time and dates are given in universal time and the velocity vectors are

TABLE 5.1

ION AND NEUTRAL CLOUD VELOCITIES FROM A NUMBER OF BARIUM RELEASES

Experiment Number	Date (UT)	Time (UT)	Height (km)	Neutral Cloud Azim.	Neutral Cloud Speed	Ion Cloud Azim.	Ion Cloud Speed	Range (ref.)
1	7.4.67	2001	230	177	180	122	280	i(a)
2	8.4.67	2003	234	186	128	239	132	i
3	9.4.67	0104	243	158	217	95	289	i
4	10.4.67	2018	230	282	121	116	200	i
5	11.4.67	2025	236	189	133	220	67	i
6a	23.10.67	1609	205	86	67	254	117	i
6b	23.10.67	1609	154	75	67	260	111	i
7a	20.3.68	1827	218	172	43	109	43	i
7b	20.3.68	1827	170	253	55	145	26	i
8a	23.3.68	1839	212	122	60	220	77	i
8b	23.3.68	1839	167	132	65	225	79	i
9a	15.3.69	1758	146	264	430	245	250	i
9b	15.3.69	1758	190	281	378	243	350	i
9c	15.3.69	1758	226	263	167	233	333	i
10a	17.3.69	1804	145	265	458	263	700	i
10b	17.3.69	1804	196	257	433	254	700	i
10c	17.3.69	1804	241	237	450	254	766	i
11	18.3.69	1819	173	230	150	240	227	i
12a	14.2.70	1619	195	277	86	263	425	i
12b	14.2.70	1619	210	277	188	265	545	i
12c	14.2.70	1619	175	280	50	260	505	i
13a	2.4.70	0148	175	144	100	94	40	i
13b	2.4.70	0148	210	172	133	114	35	i
13c	2.4.70	0148	175	154	114	108	43	i
14	4.4.70	1916	210	-	0	96	47	i
15a	31.8.67	2206	230	195	137	95	595	ii(b)
15b	31.8.67	2206	278	151	210	96	690	ii
15c	31.8.67	2206	310	150	238	95	950	ii
15d	31.8.67	2206	225	161	81	97	720	ii
16a	2.9.67	2031	230	191	85	88	1625	ii
16b	2.9.67	2031	320	107	155	107	535	ii
16c	2.9.67	2031	230	232	183	127/333	195/220	ii
17	5.3.69	0430	170	123	119	138	61	iii(c)
18	6.3.69	0430	170	119	75	318	90	iii
19	15.3.69	0506	165	325	71	313	2000	iii
20	19.3.69	0517	168	140	100	142	53	iii
21	20.3.69	0537	176	44	83	299	217	iii

i Esrange, Sweden
ii Andenes, Norway
iii Poker Flat, Alaska

(a) Stoffregen et al., 1971
(b) Wescott et al., 1969
(c) Olsen, 1970

presented as true azimuth and speed in m sec^{-1}. Errors are not given in some of the original data; these errors are expected to be within $\pm$ 20 m sec^{-1} or $\pm$ 10%, whichever is greater. In cases where the ion velocity varied during the observations, two values are given representing the extreme motions. In one of these cases, 15d, the electric field reversed as is evidenced by the nearly 160° azimuth change. These data are taken from two principal launch areas (Alaska and Western Europe).

In a first attempt to determine the presence of ion-drag acceleration of neutrals, the ion drift- and neutral motion-vectors are plotted in Figure 5.1. In this diagram a large dot represents a neutral-wind vector, $\vec{U}_{\perp}$, and the ion-drift vector, $\vec{V}_{\perp}$, is represented as the end point of the line emanating from the neutral dot. Thus the plotted lines represent the vector difference $|\vec{V}_{\perp} - \vec{U}_{\perp}|$, and the end points of each line give the neutral and ion velocities. The (1965 Corrected) geomagnetic directions form the reference frame. This coordinate system was chosen because it best orders the ion drift velocities along the east-west axis. Two ion-drift velocities cannot be plotted on this scale, their positions are indicated by the directions of the arrowheads and a number indicating their distance from the origin.

There are certain observations which can be made from inspection of Figure 5.1. These observations are:

1. a pronounced lack of northward velocity component is present for both the neutral- and ion-motion,
2. the westward zonal component for the neutrals predominates over the eastward zonal motion,

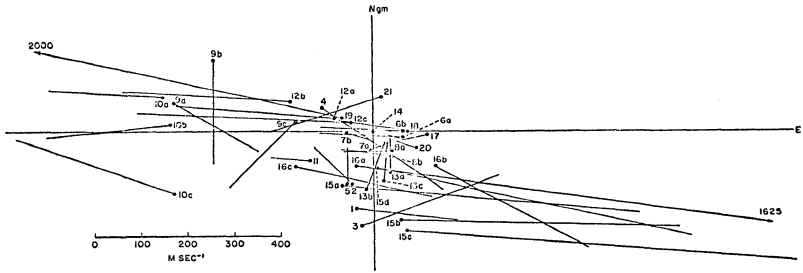

Figure 5.1 Distribution of observed barium neutral cloud velocities (•) and barium ion cloud velocities (end of line connected to dot) for the releases listed in Table 5.1 in a geomagnetic coordinate frame.

3. the zonal ion motion is generally stronger than the zonal neutral motion,

4. the vector velocity difference between the ion- and neutral-motion is generally large and is never zero. The greater the neutral speed the greater is the velocity difference.

The first of these observations results from the established (in Chapter 4) character of the meridional wind component. The second is easily accounted for since most of these releases were made in the evening twilight, a time when positive bays, and corresponding westward ion-drift, predominate. A check of the magnetogram at the station closest to the release indicates this is indeed true. The third and fourth observations suggest that, at times of activity, neutral zonal motion is largely driven by ion-drag. For the ion-drag force to cause neutral acceleration, there must be a velocity difference between the ions and neutrals. Obviously, this velocity difference exists and is never zero, at least for the twilight situation of these releases.

Since the ion-drag force depends explicitly upon the velocity difference $\vec{V}_\perp - \vec{U}_\perp$, this quantity is examined next. Figure 5.2 is a plot of $\vec{V}_\perp - \vec{U}_\perp$ in a geomagnetic frame. There is an obvious tendency for the vector differences to be aligned along the geomagnetic east-west directions, which must result from a preferred orientation of the electric field vector. Figure 5.3 contains a plot of $\vec{V}_\perp - \vec{U}_\perp$ in a frame which is aligned with the statistical orientation of auroral arcs as given by Gustafsson's (1967) mean data curve. There is a tendency for the vector velocity difference to be aligned along the

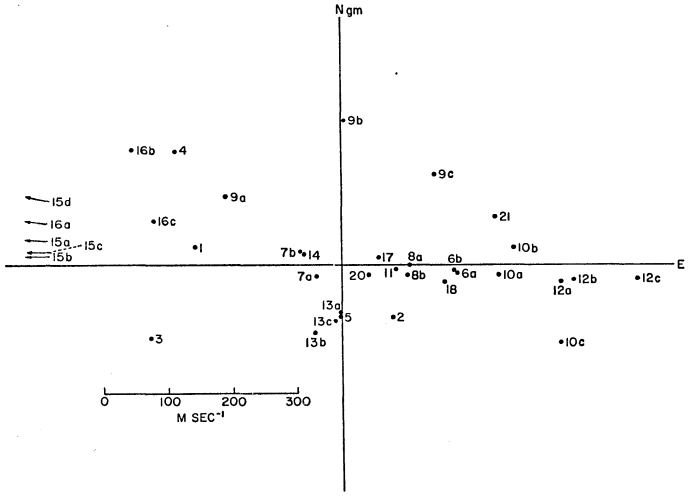

Figure 5.2 Distribution of the velocity difference vector ($\vec{v}_\perp - \vec{u}_\perp$) for the barium releases listed in Table 5.1 in a geomagnetic frame.

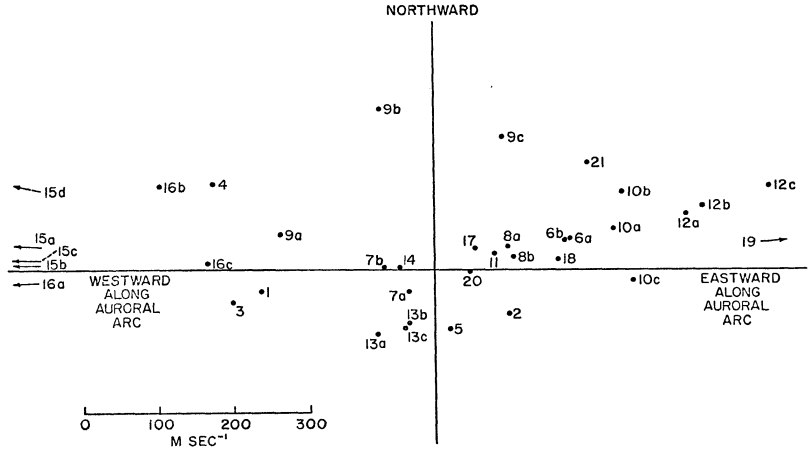

Figure 5.3 Distribution of the velocity difference vector ($\vec{v}_\perp - \vec{u}_\perp$) for the barium releases listed in Table 5.1 in a frame aligned with the statistical orientation of auroral arcs.

statistical arc direction but this tendency is not as strong as the alignment in the geomagnetic frame. A possible error may be present in the calculation of magnetic time used to find the arc orientation from Gustafsson's data, but the actual error in arc orientation expected is less than the individual station departures from Gustafsson's mean curve. As such, this error should not be important. There are, however, significant changes in arc orientation through a substorm (depending upon the position of the station with respect to the auroral oval and the substorm). These cannot be reflected in Gustafsson's mean curve and will serve to scatter the present data points. Unfortunately, it is only very rarely that the orientations of auroral arcs at the times of barium releases are reported. Thus the present alignment must be considered as reasonable supporting evidence for electric field orientation normal to auroral arcs and corresponding alignment of ion-drag winds along the arcs. However, alignment is better in the geomagnetic frame so this frame will be used even though it is expected that the controlling orientation is that of the auroral arcs.

Figure 5.4 contains a histogram of the number of observed velocity differences, $|\vec{V}_\perp - \vec{U}_\perp|$, in 50 m sec^{-1} increments. Two very large differences were omitted from this diagram. The mean velocity difference is approximately 230 m sec^{-1}. According to the discussion presented in Chapter 2, this velocity difference is great enough for ion-drag to be an important force for high-latitude thermospheric neutral motion in the twilight situations examined here.

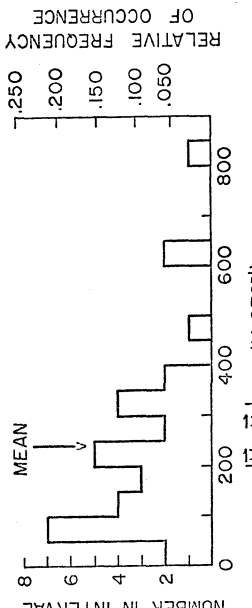

Figure 5.4 Histogram of the velocity difference $|\hat{V}_T - \hat{U}_T|$ for the barium releases listed in Table 5.1.

Rees (1971) has plotted the zonal wind speed determined from barium clouds released above 150 km against the average perturbation in the H magnetic component of a nearby magnetometer. His data are shown in Figure 5.5. Rees finds that there is a linear relationship when a two-hour average of ΔH is used, but no obvious relationship with 1 or 3 hour averages. This is taken to be evidence for a 2 hour time constant.

This approach to finding the time constant for neutral thermospheric response, however, may be questioned. The magnitude of the current density, $|\vec{J}|$, can be expressed as a product of the magnitude of the electric field seen by the charged particles, $|\vec{E}'|$, and an effective, height-integrated, conductivity for currents perpendicular to the magnetic field, which is denoted by $\Sigma_\perp$. The magnetic perturbation measured at the earth's surface is proportional to $|\vec{J}|$, and is principally in the direction of $\vec{E}'$ because the height-integrated Hall conductivity, Σ_H, exceeds the height-integrated Pedersen conductivity, Σ_P (Wescott et al., 1970). The ion velocity at high altitudes (above 150 km) is in the Hall current direction and has magnitude E'/B. As shown in Chapter 2, the neutral thermospheric gas asymptotically approaches this velocity with a time constant which is to be determined. In principle, if the conductivity remains constant, Rees suggests that the neutral zonal speed should be proportional to the magnitude of the time average of the magnetic perturbation when the averaging interval is equal (approximately) to the time constant. One major difficulty with this argument is that $\Sigma_\perp$ is not constant.

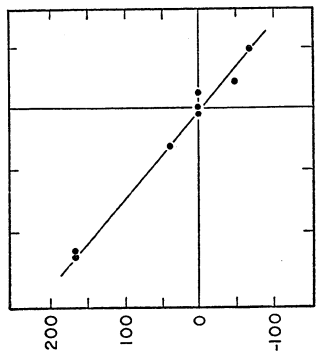

Figure 5.5 Plot of barium neutral cloud zonal speeds against the two hour average of the ΔX magnetic perturbation. From Rees (1971).

Additionally, other forces acting upon the neutral gas producing zonal winds complicate the analysis. Judging from the previously mentioned tendency of the barium neutral speeds to be larger when the barium ion-drift speeds are large, it is anticipated that it is in these events that a relationship between $\overline{\Delta H}$ and the neutral zonal wind should be sought. When the ion-drift speed is small, ion-drag neutral motion is small and observed neutral motions are extremely sensitive to other zonal forces. Thus points must be disregarded near the origin of Rees' diagram. When this is done, it is apparent that the relationship found by Rees is really based upon three points. Of course, if all other contributions to zonal winds were known, these could be removed from the observations so that just the ion-drag term remained. However, this is not possible at this time.

As a check of the above arguments, two figures are presented based on the releases tabulated in Table 5.1. In Figure 5.6 the magnitude of the total horizontal perturbation $[(\Delta X)^2 + (\Delta Y)^2]^{1/2}$ is plotted versus the magnitude of ion-drift ($\vec{V}_i$). The corresponding electric field is indicated as well ($B = 5 \times 10^{-5}$ T was assumed). Straight lines indicate the expected behavior for a uniform horizontal current sheet with fixed transverse height-integrated conductivity $\Sigma_\perp$. Judging from the scatter of these points there is considerable variability of the auroral-zone ionization. This figure and conclusion are similar to those presented by Haerendel (1970). Figure 5.7 shows the present data (from Table 5.1) plotted for comparison with Rees'

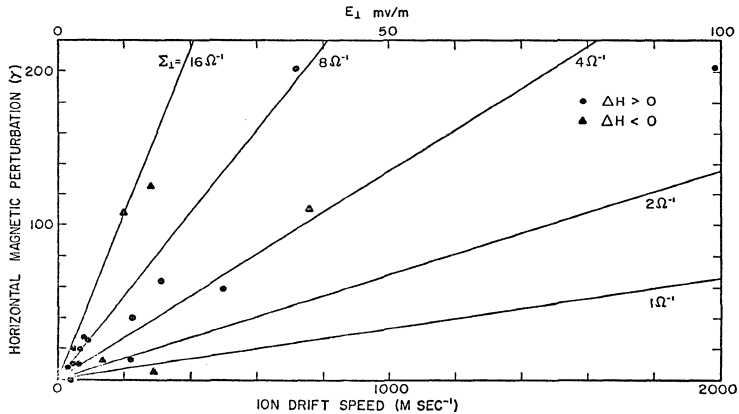

Figure 5.6 Ion-drift speed versus the recorded magnetic perturbation $\sqrt{(\Delta X)^2 + (\Delta Y)^2}$ at the launch site and time of launch for the barium releases listed in Table 5.1. The straight lines indicate the values of the effective transverse conductivity $\Sigma_\perp$ which would give the measured magnetic perturbation when an infinite plane current is tangent to the dynamo layer at the station and induced ground currents are not present.

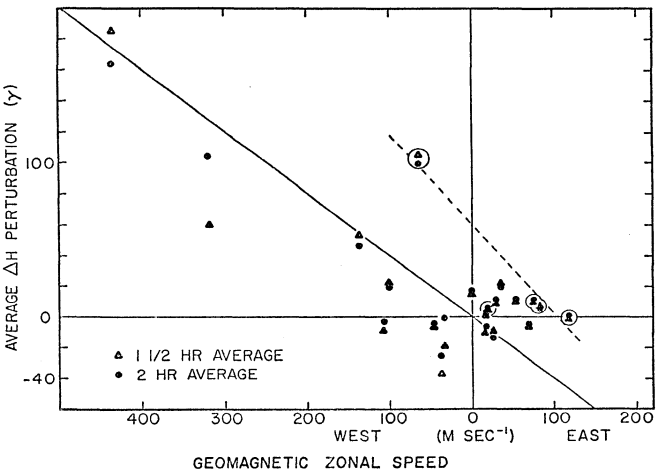

Figure 5.7 Plot of the observed (geomagnetic) zonal speeds of the barium clouds listed in Table 5.1 against the 1 1/2 and 2 hour averages of the H magnetic perturbation measured at the launch site. The Alaskan releases are circled. The dashed line shows the mean relationship between the average magnetic perturbations and the zonal speeds of the Alaskan releases. The solid line indicates the relationship found by Rees (1971).

diagram (Figure 5.5). Following Rees (1971), the magnetogram of the station closest to the release point was scaled every five minutes and these scaled values were averaged over four intervals, the first hour, the second hour, the first hour and a half, and the first two hours. Differing from Rees' procedure, Figure 5.7 is of the perturbation $\overline{\Delta H}$ and the geomagnetic zonal component of the wind. As was shown earlier, any ion-drag wind component will show most clearly in a geomagnetic frame which is more nearly aligned with the auroral electric field than a geographic frame. For the Esrange releases the difference between geographic and geometric frames is small but this is not the case for the Alaskan releases. In order to plot all of the releases listed in Table 5.1 on one diagram, a geomagnetic frame is employed. The same frame should be taken for the magnetic data, i.e. $\overline{\Delta H}$. Some of the plotted points fall nearby the straight (unbroken) line indicating that they tend to fit Rees' relation. Substantially increased scatter is observed when similar plots were made using the first and second hour average perturbation values. In the present case, there is no reason for choosing either the 1 1/2 hour or 2 hour averages as giving a better fit. If the method were believed to be correct then the conclusion could be reached that the time constant for neutral acceleration by ion-drag is approximately 1 1/2 to 2 hours. For the present data, averaging over periods greater than 2 hours was not attempted as Rees has already determined that no better relationship is obtained.

The Alaskan releases (circled) tend to be aligned along a line

(shown as dashed in Figure 5.7) which intersects the ΔH=0 axis at a neutral zonal speed approximately 100 m sec^{-1} (eastward) from the same intersection of Rees' line. As stated earlier, Rees' line is primarily based on three releases, which were made from Esrange on March 15, 17, and 18, 1969. These releases were all made within 10 minutes of 1905 local time. For this time Challinor's model predicts the zonal tidal wind component to be eastward at 250 m sec^{-1}. The Alaskan releases were all made within 30 minutes of 1900 local time in early and mid March of 1969. Thus we should expect that the observed difference between the behavior of these two groups of releases is real and not due to some long term variation of the thermosphere, although the difference may not be statistically significant due to the small number of releases in each case. At this point, however, it can only be assumed that the difference is real. Challinor's (1970a) tidal wind prediction indicates that the zonal component should have a magnitude of 230 m sec^{-1} (eastward) at College for the above time. The difference between these two predicted zonal speeds is insufficient to cause the observed 100 m sec^{-1} difference. However, Challinor's 250 km model is not appropriate for these data. The mean release height of the Esrange releases used by Rees was 188 km, while the mean height for the Alaskan releases was 170 km. The 180 km prediction of Vest (1973) might then be more suitable. This approach predicts eastward zonal speeds of 160 m sec^{-1} for College and 170 m sec^{-1} for Kiruna at these times. Interpolation to the mean altitudes will not help since the Esrange releases would be pre-

dicted to have a larger eastward speed than the Alaskan releases.

The discrepancy between the zonal velocities of the Alaskan and the Esrange releases is not removed when the neutral wind component parallel to the average auroral arc orientation is plotted against the magnetic perturbation component perpendicular to the arc orientation. Either the discrepancy is due to too small a sample or is due to differences in the conductivity. It is difficult to see how a zero error of 80γ could be made systematically for one of the two stations. The remaining variable which is difficult, if not impossible to account for in these plots, is the conductivity.

Two estimates of the magnitude of horizontal gradients of the horizontal thermospheric winds may be made, using published data. On two occasions, at 1836 LT March 2 and 0445 LT March 4, 1970 (both dates UT), simultaneous releases of (nominally) 4 barium clouds were made from Barter Island, Alaska, and Poker Flat Range. The neutral cloud velocities from these releases have been scaled from figures presented by Meriwether et al. (1972). These data are not included in the releases listed in Table 5.1. Table 5.2 lists the individual neutral cloud velocities together with the release heights and mean velocities for each group of releases on the two nights. The mean separation between the groups of releases was 650 km for the March 2 releases and 530 km for the March 4 releases. Velocity differences within each group of releases are believed to be due to triangulation errors.

The magnitudes of the horizontal wind gradients are determined

TABLE 5.2

NEUTRAL BARIUM CLOUD VELOCITIES FROM RELEASES MADE SIMULTANEOUSLY FROM TWO LAUNCH SITES IN ALASKA (GEOGRAPHIC COORDINATES)

DATE	RELEASE	HEIGHT (km)	SPEED ($m\ sec^{-1}$)	AZIMUTH
2 March 1970	2S1	239	230	10°
(Poker Flat)	2S2	314	200	319°
	2S3	324	310	327°
	2S4	253	280	340°
		Mean	231	347°
2 March 1970	2N1	218	300	348°
(Barter Is)	2N2	252	230	317°
	2N3	219	180	339°
		Mean	230	336°
4 March 1970	4S1	220	200	246°
(Poker Flat)	4S2	284	300	230°
	4S3	278	320	248°
	4S4	232	290	265°
		Mean	270	247°
4 March 1970	4N1	218	510	255°
(Barter Is)	4N2	285	700	263°
	4N3	282	710	262°
	4N4	226	640	252°
		Mean	638	258°

from the mean velocity vectors of each group of releases. There is essentially no horizontal gradient between the northern and southern release groups of March 2. The mean speed difference (1 m sec^{-1}) and azimuth difference (11°) are not significant. The speed difference (368 m sec^{-1}) between the release groups of March 4, however is great enough to be significant. The horizontal gradient is 0.69 m sec^{-1} per km. Again, the difference in azimuths (11°) on March 4 is probably not significant.

There is a considerable difference between the magnitudes of the horizontal gradients observed on these two occasions. On both occasions, the observed winds were substantially zonal and several auroral arcs were observed between the two groups of releases. Meriwether et al. (1972) indicate that some of the individual neutral cloud velocities may have been obtained from as little as 3 minutes of observation. Relatively large errors are therefore suspected. Furthermore, the data have been averaged over a considerable range in altitude (218-324 km) without regard for real altitude dependent differences. This averaging can only reduce the magnitude of the horizontal gradients. Nevertheless, it appears that the magnitude of the horizontal gradient of the horizontal wind is still smaller (by nearly an order of magnitude) than the vertical gradient of the horizontal winds (see estimates of Chapter 2 and section 5.5).

Of the three questions posed at the beginning of this section, partial answers have been obtained for two but the question of the effective time constant remains unanswered. It has been shown that

ion-drag is an important driving force for neutral thermospheric motions in the east-west (zonal) directions. However, the relative importance of pressure-gradient forces and ion-drag forces is unresolved. It has been demonstrated that the magnitude of the zonal winds is related to the magnetic perturbations measured at the earth's surface. The relationship, however, remains poorly defined. Examination of the 6300A interferometric observations is made next to pursue these questions further.

5.3 OBSERVATIONS OF ZONAL WINDS BY 6300A INTERFEROMETRY

Investigation of the characteristics of the zonal wind component are continued with examination of observations of these winds obtained by the University of Michigan interferometer. A histogram of the hourly averages of the zonal (geomagnetic) wind component is plotted in Figure 5.8 (a-e) together with the trace of the horizontal (H) magnetic perturbation as measured at College. Dates are given in UT and refer to the 0000 to 2200 (UT) time period of each diagram. The scale values are the same for each graph. The baseline of the magnetometer trace approximates the quiet day (S_q) variation and is believed to be accurate within 10γ. Here only a crude analysis of the variations of the zonal component is made because of the lack of detailed knowledge of the distribution of auroral 6300A emission at the time of the measurements and because of the relatively large error of measurement and the spatial averaging inherent in the reduction procedures. Additionally, measurements of the electric field, while in part available, are not used here. Instead the ΔH component is

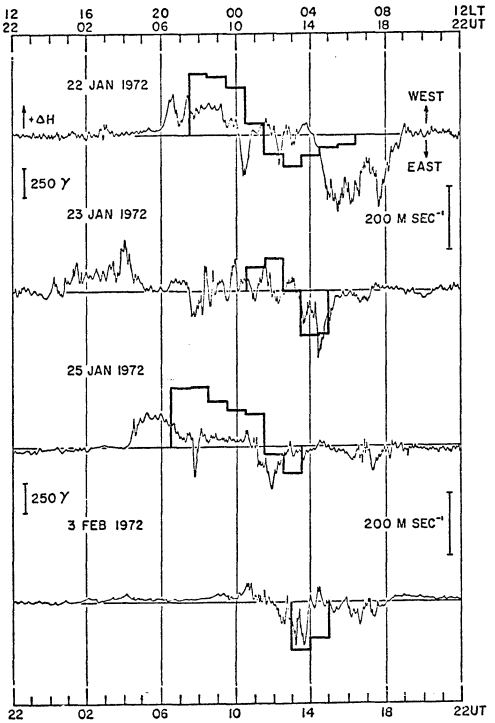

Figure 5.8a Observed magnitudes of the zonal wind component obtained at Ester Dome Observatory by 6300 Å interferometry with the College ΔH magnetic perturbation.

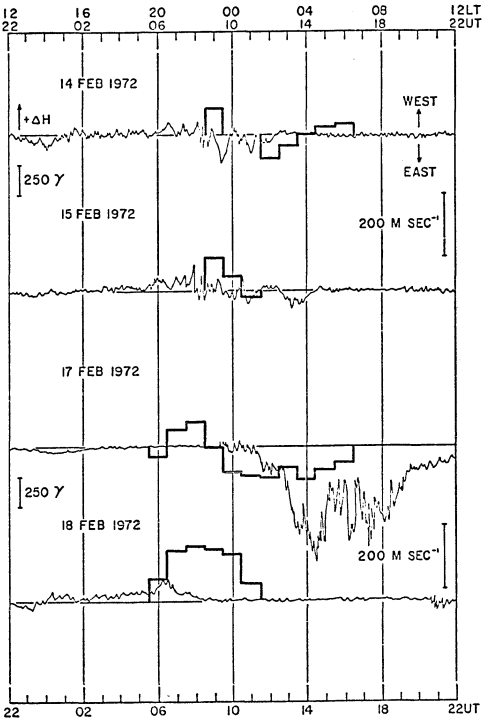

Figure 5.8b

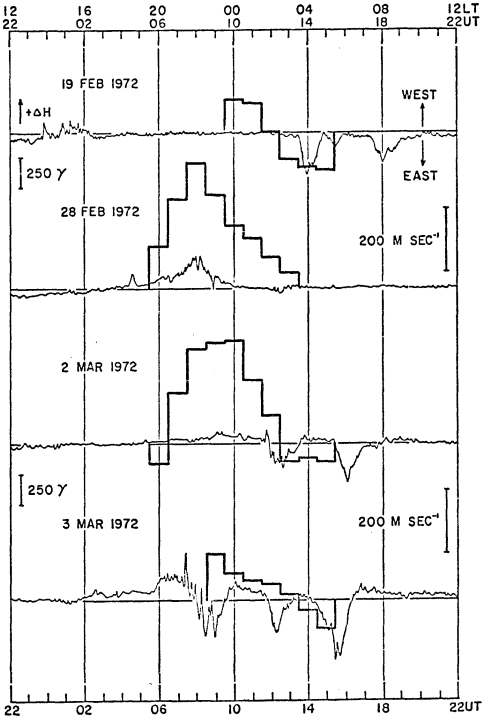

Figure 5.8c

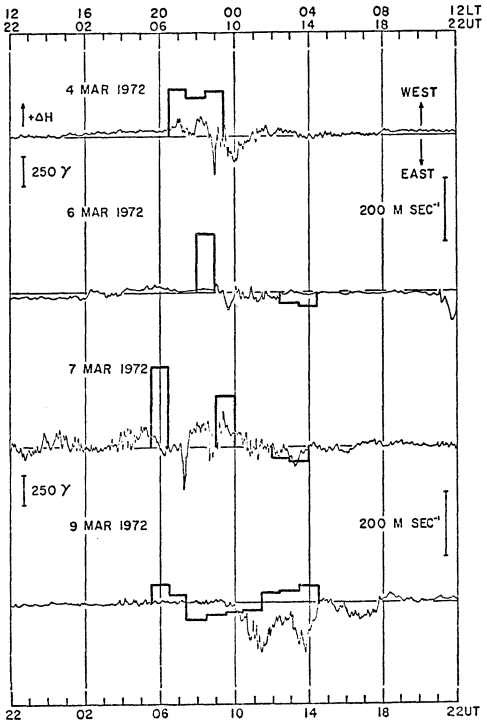

Figure 5.8d

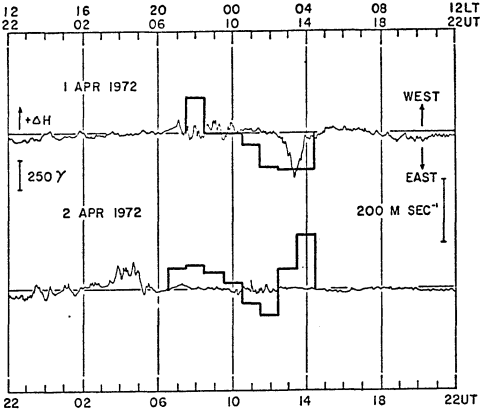

Figure 5.8e

used as an indication of the direction of the electric field. An ordering of the variations according to magnetic activity and time is attempted here. Interest is focussed upon the gross temporal behavior of the zonal winds.

Since the ion-drag force can be expressed as $\vec{J} \times \vec{B}$ and the surface magnetic perturbation $\Delta\vec{B}$ is related to the integral of $\vec{J}$ over all space, it should be expected that changes in the zonal wind speed can be directly related to the measured magnetic perturbation. However, the bulk of the current seen by a surface magnetometer is in the dynamo region (90-130 km) while the observed winds, and therefore the $\vec{J}$ of interest, are higher (above 150 km). Relative changes in the electron density profile above and below 150 km can cause correlation between the zonal wind speed changes and the measured magnetic perturbation to break-down. Such changes must be anticipated in the auroral zone as the character of the precipitating particle fluxes changes, producing ionization at different heights. Since the direction of the electric field can be inferred from the sign of the H component magnetic perturbation independently of the electron density profile, correlation is attempted with the electric field direction. The influence of field-aligned currents is not expected to be important in this correlation.

Detailed inspection of Figure 5.8 yields the following description of the behaviour of the zonal wind component. In the very early evening, the zonal wind component is at times eastward. This only occurs where there is very little or no magnetic disturbance, and only appears in

the present data on February 17 and March 2. The eastward component is interpreted as the tidal wind motion of the thermosphere from dayside to nightside. On neither occasion does the zonal motion reverse prior to the occurrence of some magnetic disturbance. On most nights, however, there is some magnetic disturbance and the first observed winds are consistently westward. A positive disturbance is seen in the H magnetic component, associated with a northward directed electric field. The magnitude of this westward zonal component, at times, appears to be related to the magnitude of the ΔH perturbation although the proportionality factor may differ, as can be seen in comparison of the February 28 and March 2 data. On other occasions such proportionality is not evidenced but the association of a positive disturbance in ΔH with westward motion is clear. If a negative bay develops, as a result of a change from northward to southward electric field direction, the zonal winds begin to respond by decreasing. For short-lived negative bays or for small-amplitude bays the zonal component may not reverse and will remain westward. This behavior is seen in the January 25 and March 3 data. If, however, the negative bay is of long duration or large amplitude, such as on March 2 or the second bay on January 25, the westward zonal motion is changed to eastward motion. This eastward zonal wind may persist throughout the remainder of the observing period or may become westward again (for example February 14 and April 2), if a positive bay is re-established.

This gross behavior is consistent with ion-drag acceleration of the zonal component of neutral motion at these altitudes. At times the magnitude of these winds appears to be proportional to the magnetic

perturbation although the proportionality factor seems to vary from night to night as well as during the night on most observing nights. This is consistent with our knowledge of the conductivity, and it is more surprising to find occasions when the conductivity is apparently constant. It appears that the zonal component of thermospheric winds as measured by the Doppler shift of auroral 6300A emission follows the temporal variation of the electric field in a manner which is consistent with theory.

There are however some events which are at odds with the above interpretation. On February 17, the zonal component became eastward prior to any significant negative bay activity. March 3 shows westward winds persisting through the latter part of the first negative bay and through a second negative bay beginning at 0200 LT. Earlier measurements of the winds would be of benefit in resolving this apparent lack of neutral response. If a large zonal westward wind ($\geq$ 300 m sec^{-1}) were associated with the positive bay between 2030 and 2300 LT and if the ionospheric electric field was thereafter small, then the observed zonal wind could be just the slowing down of the pre-existing wind. However, the tidal wind field at the times of the measurements is expected to have a westward component. The tidal wind field may then be responsible in part for the observed behavior. This explanation can be applied to the zonal winds observed between 0000 and 0400 LT on March 9. During this time period, the geomagnetic zonal component of the tidal wind at 250 km in Challinor's model (see Figure 4.2) is predicted to change from eastward at 180 m sec^{-1} to westward at 110 m

sec^{-1}. This is more than sufficient to cause the observed reversal. The possible effects of tidal zonal winds must therefore be investigated.

Figure 5.9 shows the average magnitude of the zonal wind component of the interferometer measurements as a function of time. All data points (from Figure 5.8) were used. Because some of the wind determinations began on the half hour, 30-minute averages were performed. The mean and standard deviation of the zonal component are shown for each 30-minute period. In spite of the large deviations, there is a remarkable trend. The zonal speed passes through zero approximately 0210 LT or about 1/2 hour after magnetic midnight. Statistically, the magnetic field at auroral-zone stations changes from positive ΔH to negative ΔH at 2300 local magnetic time. Thus the zonal wind reversal occurs about 2 hours after the statistical magnetic reversal. Prior to this time a regime of westward motion is present. This average westward zonal wind attains a peak speed of 160 m sec^{-1} at 2200 LT or about 3 1/3 hours before magnetic midnight. After reversing, the zonal component on average has a rather small magnitude of approximately 50 m sec^{-1} and no clearly defined trend. Coincidently, the model tidal zonal winds (at College) reverse at about 0230 LT (see Figure 4.2). However, the tidal winds are quite unlike the average temporal behavior exhibited by the observed winds. In fact, the predicted tidal zonal winds are so different from the observed winds that the data suggest that the tidal winds are not important. It appears that for the zonal component the ion-drag winds completely dominate the tidal motion.

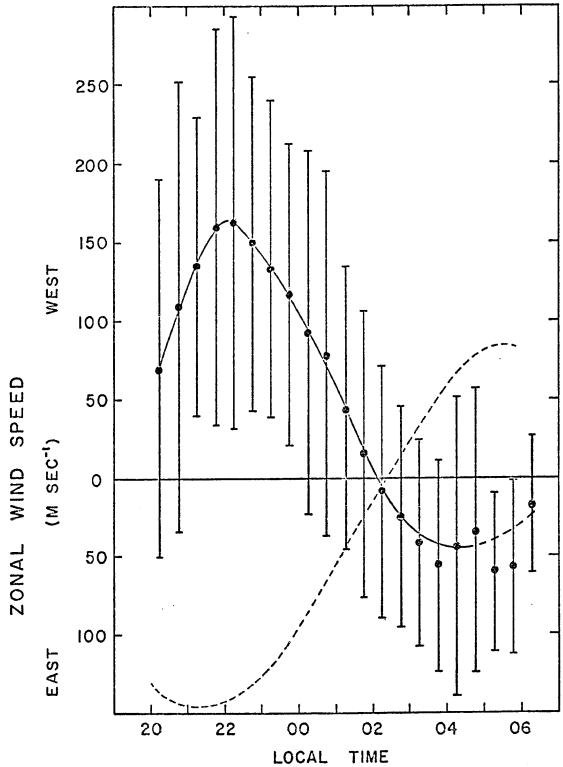

Figure 5.9 Mean and standard deviation of College 3600Å interferometer measurements of the zonal winds. Dashed curve is Challinor's (1970a) predicted zonal component with amplitude halved.

This same behavior is apparent in the zonal components of motion of the European releases listed in Table 5.1. The mean zonal component of these releases appears to reverse about 2230 LT, with a possible error of about 1 hour because the number of releases is small. The models predict the tidal zonal component should reverse about 2330 LT. The phase relationship between the predicted zonal winds and the European releases zonal motions is very similar to that seen in Figure 5.9 except that the observed winds may reverse about one hour before the model winds. The observed zonal reversal is about 1 hour after magnetic midnight, just as is seen in the College data.

Since the meridional component of the tidal winds are observed to be an apparent factor of 2 smaller than predicted by the models of Challinor (1970a) and Vest (1973), it seems reasonable to suppose that the zonal tidal winds are similarily reduced. There is a method which allows this supposition to be checked. If the zonal wind component of ion-drag winds is denoted by U_{yI} and the observed zonal wind component is denoted by U_{yo}, then for each altitude and time the following relation may be written

$$U_{yo} = U_{yI} + U_{yT} \quad , \qquad 5.1$$

where U_{yT} is the zonal component of the tidal wind. Strictly speaking, equation 5.1 is not valid because of the presence of the nonlinear term in the equation of motion. However, in order to carry out this analysis, it will be assumed that equation 5.1 is valid and that the vertical gradients of the horizontal winds is zero. That is, it is assumed, that for the altitudes of interest, both the tidal winds and

the ion-drag winds are altitude independent. This condition seems to be met for altitudes above 150 km for both the tidal wind predictions of Vest (1973) and for the ion-drag winds of Fedder and Banks (1972). Using equation 5.1, the ion-drag component (U_{yI}) may be computed from the average zonal winds (shown in Figure 5.9) and the tidal model of Challinor. Figure 5.10 shows the results of these computations. The heavy curve results when Challinor's model tidal winds are halved and the light curve results when the full predicted magnitudes are used. The effect of the removal of the tidal zonal winds is to increase the magnitude of the computed ion-drag winds. Using Challinor's full magnitudes, the computed zonal ion-drag winds can easily be acquired two hours after turning on of an electric field of 60 mv m^{-1}, assuming a time constant of 2 hours. This field strength is somewhat large, and a more reasonable value of 45 mv m^{-1} is obtained if Challinor's speeds are too large by a factor of two. This argument is sensitive to the actual value of the time constant, but is taken, nevertheless, as indication that for the zonal component of the tidal wind field the models have too large a magnitude.

This same procedure for removing the tidal component may be applied to the individual observations as well as the averaged data. Figures 5.11 (a-e) contain histograms of the computed ion-drag winds when tidal winds with magnitude half that predicted by the models are removed. All of the basic features previously ascribed to the observed zonal winds are retained in these figures. Additionally, some of the discrepancies are removed.

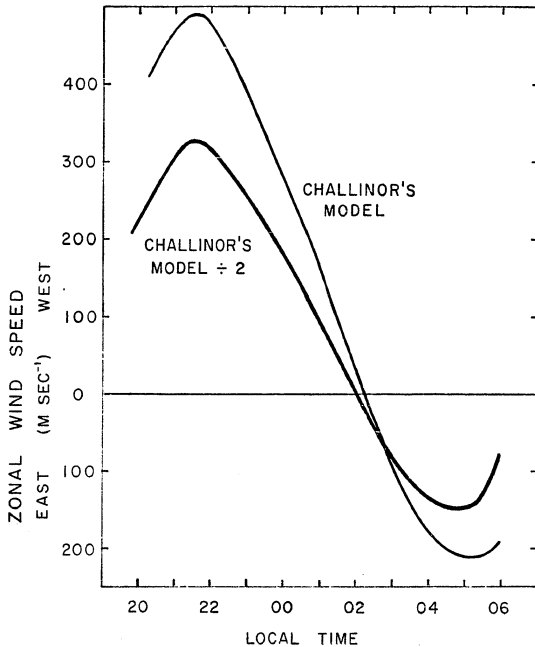

Figure 5.10 Computed ion-drag winds obtained from the mean observed winds and Challinor's tidal model. The light curve represents the ion-drag winds computed using Challinor's model. The heavy curve results from using Challinor's model with amplitude halved. See text for details.

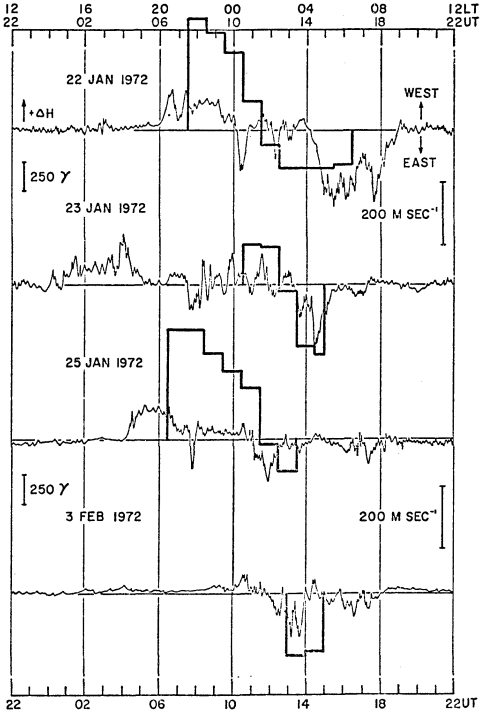

Figure 5.11a Computed zonal ion-drag winds. See text for explanation.

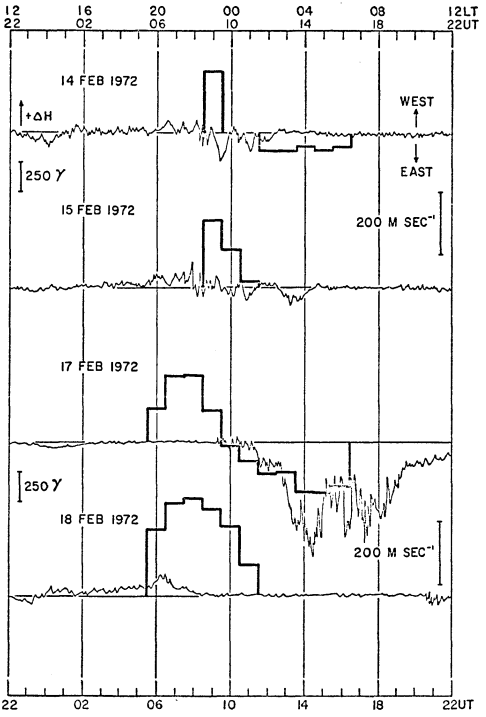

Figure 5.11b

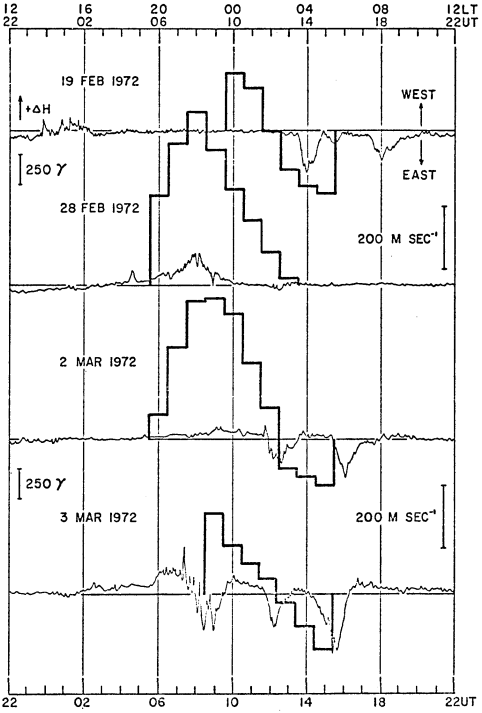

Figure 5.11c

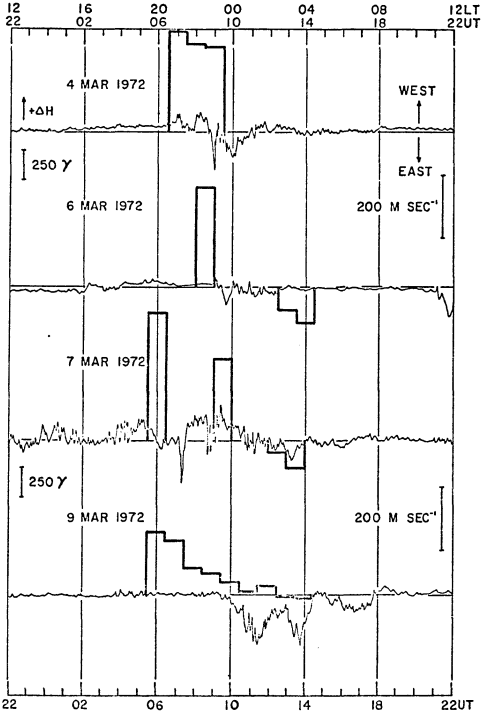

Figure 5.11d

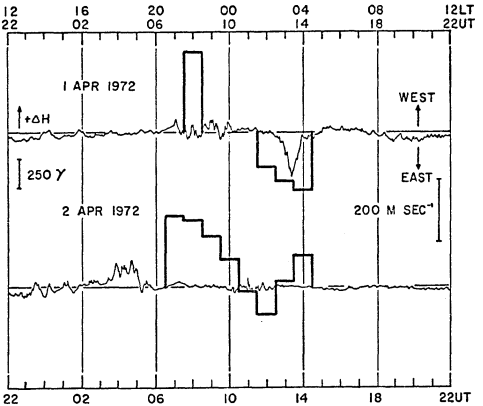

Figure 5.11e

Figure 5.12 shows the mean and standard sample deviations of the observed zonal winds as a function of substorm time. For the present purpose t = 0 substorm time was defined as the time at which the first strong negative bay occurred. Precisely the time at which ΔH at College changed from positive to negative was used. However, in order to keep sample intervals the same, deviations of $\pm$ 15 minutes were allowed. The decrease in zonal speed prior to t = 0 is apparently real and precludes determination of the time constant of neutral response. Nevertheless it is possible to define a response time of the neutral motion to reversals of the electric field. This response time is taken as the delay after substorm onset at which the zonal wind reverses. For these data, the response time is just short of one hour.

A similar examination is made of the data modified by the removal of Challinor's zonal component with magnitude halved. This result is shown as Figure 5.13. Note that Figures 5.12 and 5.13 are very similar, again indicating that the removal of the tidal component does not modify the above conclusions with regard to the overall response of the neutral motion to the electric field. The response time in this case is just greater than one hour. It can be concluded, therefore, that the time constant for neutral acceleration by auroral-zone electric fields is 1 to 2 hours above 170 km.

The examination of the thermospheric zonal winds obtained from interferometric observations of auroral 6300A emission has elucidated the relationship between the zonal winds and variations of the terres-

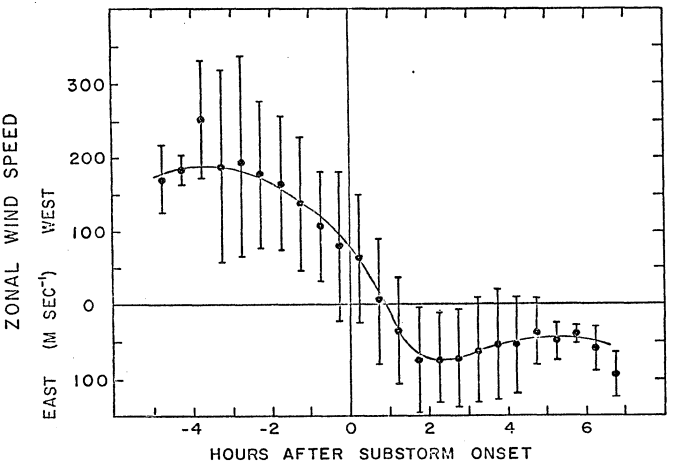

Figure 5.12 Mean and standard deviation of the observed zonal winds at Ester Dome Observatory by the 6300Å interferometer ordered with respect to the beginning of the first negative bay recorded by the College magnetometer.

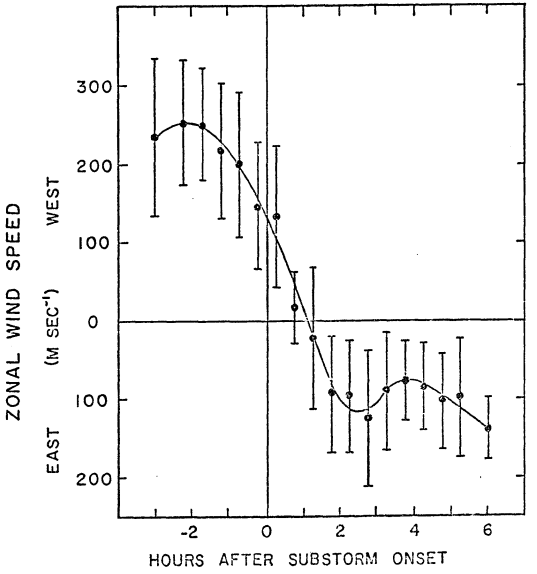

Figure 5.13 Mean and standard deviation of the computed ion-drag winds ordered with respect to the beginning of the first negative bay recorded on the College magnetometer.

trial magnetic field, and has permitted an estimate to be made of the time constant for neutral acceleration. This time constant is approximately 1 1/2 hours in the auroral-zone thermosphere. In brief, positive bays in the H component of the magnetic field are associated with westward zonal motions of the thermosphere. On the average, one hour after the onset of a negative bay, the zonal winds reverse and become eastward. Negative bays of small duration or amplitude do not necessarily precede a reversal of the zonal winds but large negative bays of sufficient duration (1 hour or more) are invariably associated with a reversal. If a positive bay re-occurs after a negative bay, the zonal winds may again reverse and become westward. The presence of the tidal (pressure-gradient) winds is obscured by the ion-drag driven winds. The relative amplitude of the tidal winds seen in the zonal component is roughly half that of the ion-drag winds. The three questions originally posed have now been answered. However, these examinations have been based upon data averaged in altitude (the interferometric observations) or with no altitude resolution (barium data). The third collection of data allows a partial examination of the vertical structure of the zonal component of the thermospheric wind field.

5.4 TRAIL RELEASE WIND OBSERVATIONS AT FORT CHURCHILL, CANADA

Figures 5.14 to 5.20 include all the published wind profiles made at Fort Churchill, Canada, by the vapor trail technique (Bedinger, 1966; 1971). Two characteristics of these profiles are immediately apparent, the presence of large oscillations in speed and direction

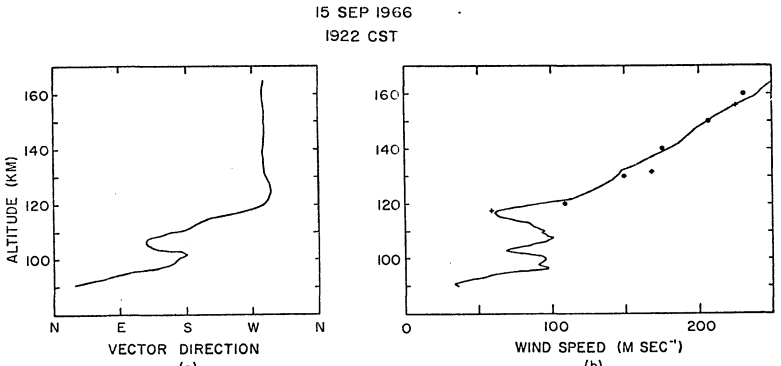

Figure 5.14 Vector neutral wind profile observed above Fort Churchill, Canada, from a TMA release at 1922 CST 15 September 1966, showing (a) the geographic direction of motionaas a function of altitude, and (b) the wind speed as a function of altitude. Crosses (+) are theoretical speeds computed by Fedder and Banks (1972) normalized at 155 km. Dots are theoretical speeds from Heaps (1972) normalized at 150 km.

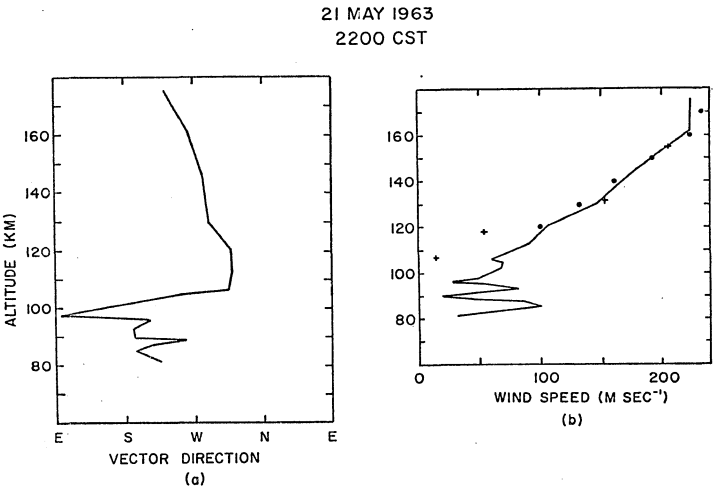

Figure 5.15 Vector neutral wind profile observed above Fort Churchill, Canada, from a TMA release at 2200 CST 21 May 1963. Refer to Figure 5.14 for other details.

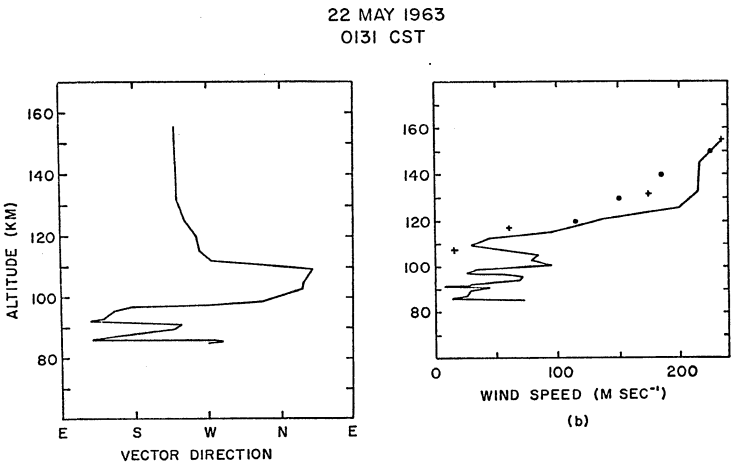

Figure 5.16 Vector neutral wind profile observed above Fort Churchill, Canada, from a TMA release at 0131 CST 22 May 1963. Refer to Figure 5.14 for other details.

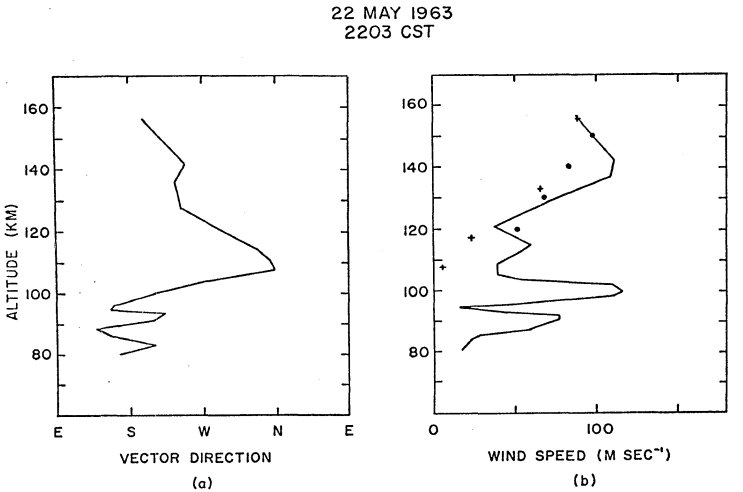

Figure 5.17 Vector neutral wind profile observed above Fort Churchill, Canada, from a TMA release at 2203 CST 22 May 1963. Refer to Figure 5.14 for other details.

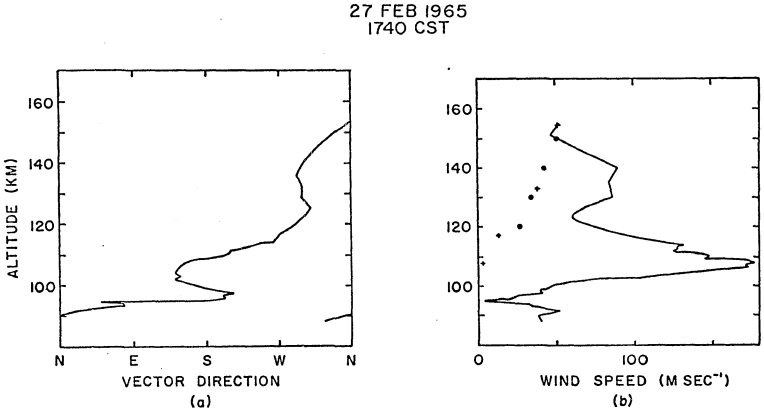

Figure 5.18 Vector neutral wind profile observed above Fort Churchill, Canada, from a TMA release at 1740 CST 27 February 1965. Refer to Figure 5.14 for other details.

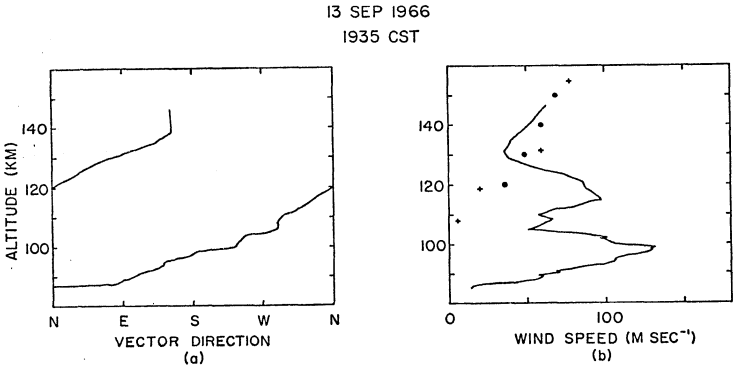

Figure 5.19 Vector neutral wind profile observed above Fort Churchill, Canada, from a TMA release at 1935 CST 13 September 1966. Refer to Figure 5.14 for other details.

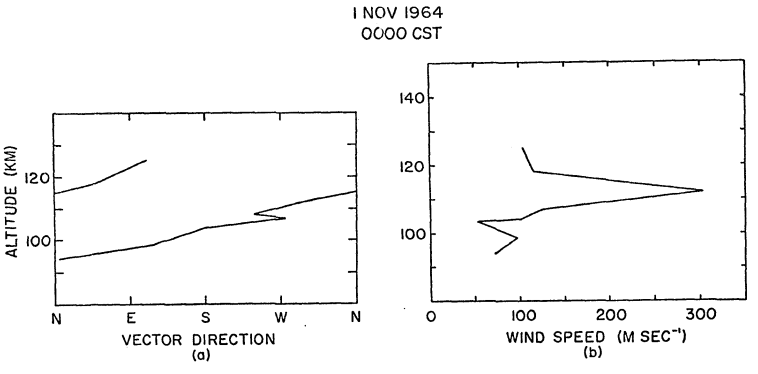

Figure 5.20 Vector neutral wind profile observed above Fort Churchill, Canada, from a TMA release at 0000 CST 1 November 1964. Refer to Figure 5.14 for other details.

which are especially marked below 110 km and, in the first half of the examples, a nearly linear speed increase with altitude between 120 and 160 km in a westerly direction. Although there is no definite proof that the oscillations are due to internal atmospheric gravity waves, Kockanski (1966) has made just this identification for the three May, 1963, profiles shown as Figures 5.15 to 5.17. An important characteristic of these oscillations is the tendency for extrema in speed to occur at the same altitudes as marked changes in vector direction. These oscillations are commonly observed between 80 and 110 km in low- and middle-latitude wind profiles. When the amplitude and vertical wavelength are plotted as a function of height, the result is very similar to that expected for internal atmospheric gravity waves (Kockanski, 1966).

On occasions similar oscillations are present above 120 km. Kockanski (1966) has identified their presence up to 180 km. This may be the cause of the irregularities appearing above 120 km in the present data. Examples appear at 130 km in Figure 5.16 and at 140 km in Figure 5.17. These observations are made to support the contention that wavelike distrubances appear in the data. However, primary emphasis is to be placed on larger scale (vertical) phenomena. The presence of these oscillations has no real consequence in the argument which is to follow because of their relatively small magnitude.

A principal feature of the data presented in Figures 5.14 to 5.20 is a strong tendency for a nearly linear increase in wind speed with altitude above 120 km. This occurs in Figures 5.14, 5.15 and 5.16.

It is characteristic of this behavior to be associated with a marked westward direction of motion. Furthermore, each of these cases appear to coincide with a period of positive disturbance in ΔX on the Fort Churchill magnetogram. The release at 1922 LT September 15, 1966 was preceded by a positive bay of seven hours duration. During this interval the peak perturbation of ΔX on the Fort Churchill magnetometer was + 120γ. The average perturbation in ΔX over the two hours before the release was + 60γ. A small positive bay event began at 1130 LT on May 21, 1963. The ΔX component measured at Fort Churchill remained positive from this time until about one hour after the release shown in Figure 5.16. A small, gradually developing, negative bay began about 0215 LT May 22, 1963. Thus both of the profiles shown as Figures 5.15 and 5.16 were obtained at times of positive magnetic disturbances. For the two hours preceding the 2200 LT May 21 release, the average ΔX perturbation was measured to be + 18γ while this average value decreased to + 9γ for the subsequent release at 0131 LT May 22.

Figures 5.17, 5.18 and 5.19 all show significantly smaller and irregular speed profiles above 120 km. The direction profiles of these winds tend to rotate slowly with altitude and are quite unlike the profiles exhibiting a near-linear speed dependence. Very little magnetic disturbance is found on the Churchill magnetometer for these events. The 2203 LT release on May 22 took place after three hours of no noticable activity. Departures from the quiet-day baseline were not apparent. A longer duration of no activity preceded the 1935 LT

13 September 1966 release (Figure 5.19). The 1740 LT release of 27 February 1965 was made after 1 hour of small (10γ) irregular oscillations. These oscillations were approximately centered on the quiet day baseline so that the net deviation from quiet day during this hour is very small. This activity followed a 4 hour period during which $\Delta X = 0$. Thus there were very little geomagnetic activity preceding this release, and the others.

One other profile (Figure 5.20) has been included for completeness. No data are given above 125 km so this profile is of little interest in this study. It should be noted, however, that this profile is exceptional in two respects. Firstly, it apparent that the wind vector executes more than one complete turn between 90 and 110 km. And secondly, the peak speed near 120 km is of exceptional magnitude. For a few hours preceding 00 hours local time on both November 1 and 2, 1964 (the release time is given ambiguously as 0000 CST 1 November, 1964) the Fort Churchill magnetogram shows no significant departure from the quiet day baseline. The spiral behavior is also apparent in Figure 5.19, again at a period of low geomagnetic activity. Such spiral winds are commonly observed at middle latitudes and probably represent the influence of semi-diurnal waves.

It is obvious that there is a marked difference in the wind speed profiles obtained during periods of positive bay activity and those obtained when there was no activity at all. It is the westerly motion associated with the positive bay magnetic activity which suggests that ion-drag is responsible for this motion. Furthermore, each of the

three profiles showing this behavior has a northward turning of the direction profile just below 130 km, before beginning to execute the more complex motion of lower altitudes. This turning is expected from the turning of the ion motion into the Pedersen direction at low altitudes.

These profiles provide a test of the model computations of Fedder and Banks (1972) and Heaps (1972). On each wind speed profile contained in Figures 5.14 through 5.19 predicted profile points have been plotted for the two models. A cross (+) indicates the speed at the given height as predicted by Fedder and Banks for a time one hour after the onset of their electric field. The dots (•) indicate profile points taken from Heaps' model for 2300 hours magnetic time, assuming that the data were taken at the center of the latitudinal electric field distribution. The crosses corresponding to Fedder and Banks' model have been normalized to the observed profile at 155 km. Heaps' profile has been normalized at 150 km. It is apparent that both Heaps' model and Fedder and Banks' model fit the observed profiles well when magnetic activity is present. However when activity is very low (Figures 5.17 - 5.19), the theoretical profiles are greatly different from the observed winds.

The correspondence between the theoretical and observed profiles suggests that ion-drag, the driving force for these two models, is responsible for the observed winds above 120 km when magnetic activity is present. When there is no magnetic activity present the observed winds are smaller and do not behave in a manner like that predicted

by the ion-drag models. In these cases, ion-drag may still be an important force, but as a frictional force, not as a driving force.

Figures 5.15 (a) and 5.16 (a) show a southerly component above 140 km while Figure 5.14 (a) shows a northerly component in this same region. According to the previous discussion, it is expected that this must be due to addition of the tidal wind field to the ion-drag winds. The variation of this added component with time is consistent with this interpretation. That is, the added component is apparently northward at 1920 LT (16 September, 1966, release) and southward at 2200 and 0131 local times (21 and 22 May, 1963, releases).

It should be expected that wind profiles obtained at times of low geomagnetic activity should be consistent with the existing tidal wind theory. The 2203 LT release of 22 May 1963 (Figure 5.17) does show a southerly component above 120 km and the 1740 LT release of 27 February 1965 (Figure 5.18) shows a northward meridional component above 120 km, in agreement with the theory. However both of these events have westward zonal components, not eastward as theory predicts. This might be due to the oscillatory perturbations present in these profiles. Additionally, a small northward electric field may be present which provides the westward zonal components without giving a measurable magnetic perturbation. With the few profiles available for study it is not possible to come to any firm conclusions. Nevertheless there is some correspondence between the observed profiles, both with activity present and not present, and the behavior expected on the basis of tidal wind predictions.

These TMA trail data are the only available means of empirically determining the vertical gradients of the horizontal winds in the auroral thermosphere. Mean vertical gradients observed between the altitudes of 120 and 160 km are 3.18, 2.88, and 3.13 m sec^{-1} per km, in the profiles showing linear speed dependence with altitude, Figures 5.14, 5.15, and 5.16 respectively. Slightly larger gradients are present in the other, irregular, profiles. Based upon the upper limits of the interferometric measurements and of the neutral barium speeds, it is estimated that vertical gradients up to a factor of 2 larger can occur. These estimates are in agreement with the numbers discussed in Chapter 2.

For the trail releases, the magnitude and direction of the ionospheric electric field, the ion-drift velocity and their time histories are completely unknown. Thus it is impossible to predict neutral wind velocities on the basis of the theories available. Accordingly, the only comparison with theory which can be made is that of the height dependence of the wind vector. When this is done, normalizing to the observed wind speed at some altitude, there appears to be reasonable agreement. The spread in local time of these observations tends to rule out other forces as a cause of the observed winds, and the predominance of the westward zonal component clearly justifies the ion-drag interpretation. Additionally, the meridional component seen in these releases (Figures 5.14 through 5.19) is in substantial agreement with tidal wind predictions. Thus, these trail data support the description which has been developed in this chapter

of zonal motions of the upper atmosphere. Very briefly, this development shows that the basic zonal motion of the auroral-zone thermosphere is determined by the horizontal electric field and is perturbed by pressure-gradients resulting from the diurnal heating of the thermosphere, globally, by the absorption of solar EUV radiation.

CHAPTER 6

CONCLUSIONS

It has been demonstrated that the principal characteristics of the auroral-zone thermospheric wind field are in qualitative agreement with the models which have been proposed, but there are substantial quantitative differences. Winds generated by pressure-gradients resulting from absorption of solar EUV radiation (tidal winds) are present in the auroral-zone thermosphere but it appears that their magnitudes are a factor of 2 smaller than several models predict. Departures of the meridional wind component from the basic tidal motion are substantial (of the same order as the tidal motions themselves) and appear to be due to auroral heating. In this respect, the magnitudes of the observed departures are much greater than one model predicts (Heaps, 1972) and occur at greater altitudes than predicted by the other model examined (Vest, 1973) although agreeing with the magnitudes of this model. The zonal component is dominated by acceleration of the neutral thermosphere by ions drifting under the influence of crossed electric and magnetic fields, the ion-drag mechanism. The principal details of this zonal motion are correctly predicted in published models but the observations differ in detail from these models because the electric field assumed differs from the field actually present. Secondary zonal motions are driven by pressure-gradients resulting from the diurnal solar EUV absorption. These comparisons, together with the principal assumptions of these models, are summarized in Table 6.1.

TABLE 6.1

COMPARISON OF WIND OBSERVATIONS AND MODELS

TIDAL MODELS	LOW AND MIDDLE LATITUDES		AURORAL-ZONE LATITUDES
Challinor (1970a)	good	1	apparently overestimates wind speeds by a factor of 2
Kohl (1970)	?	2	predominates the meridional winds in the mean
Vest (1973)	good at night	3	of secondary importance for zonal winds
ION-DRAG MODELS			
Fedder and Banks (1972)	no effect anticipated	1	qualitatively describes the zonal winds
Heaps (1972)	no effect anticipated	2	not important for the meridional winds
AURORAL HEATING MODELS			
Vest (1973)	no effect predicted	1	correctly predicts the magnitudes of the meridional wind perturbations but possibly at the wrong heights
		2	incorrectly predicts zonal winds
Heaps (1972)	no effect predicted	1	underestimates both zonal and meridional winds
COMBINED AURORAL HEATING AND ION-DRAG MODEL			
Heaps (1972)	no effect predicted	1	qualitatively describes the zonal winds
		2	underestimates the meridional wind perturbations

Specifically, the principal findings of this study are:

1. The mean temporal dependence of the observed meridional wind component at high latitudes suggests that meridional motion is primarily driven by pressure-gradients resulting from solar heating. That is, the meridional wind component is primarily tidal in origin. Hourly averages of the meridional components recorded on 18 nights during the winter and spring of 1972 show a diurnal variation similar in phase, but reduced in amplitude, to the theoretical models for the wind field based upon solar heating. Additionally, the meridional motions of some 37 neutral barium releases are in agreement with this diurnal variation.

2. Deviations of the meridional winds from their mean temporal behavior are most probably caused by Joule dissipation of the auroral electrojet and consequent heating of the thermosphere. The magnitude of the equatorward meridional winds appears to be correlated with the position of the auroral electrojet currents. When these currents are located poleward of the observing location, enhanced speeds are observed. When these currents are located overhead of the observing station, reduced speeds are observed. Increases (decreases) in K_p are associated with increased (decreased) meridional speeds. The opposite behavior is apparent when the local K index is used. Lastly, the time variation of the observed changes in the meridional winds are generally slow, suggesting heating is responsible for them.

3. Zonal winds in the auroral thermosphere are dominated by collisions with ions drifting under the action of north-south electric fields.

   The existence of a difference between ion and neutral velocities in the thermosphere has been established using barium release data, demonstrating the normal presence of an acceleratory ion-drag force. The temporal dependence of the zonal wind component is found to be consistent with theory when the direction of the electric field is inferred from the sign of the magnetic (H) perturbation. Wind speed profiles determined from three trail releases during positive bay events are in agreement with theory.

4. Pressure-gradients resulting from absorption of solar EUV radiation are of secondary importance in determining the zonal thermospheric motion at auroral latitudes.

   Zonal winds of tidal origin are detected by the presence of anomalous reversals of the observed zonal winds in comparison with their expected temporal behavior. Correction of the observed winds by subtraction of the predicted tidal component removes the anomalous reversals. If the model tidal winds are used in subtraction, too large an electric field is required to drive the computed ion-drag winds. However, if the tidal winds' component is assumed to have half the amplitude predicted by theory, the anomalies are removed and the electric field is required to have reasonable strength. These arguments lend further support to conclusion 1.

5. The response time of the thermosphere above approximately 175 km to changes in the electric field is one to two hours.

Averaging the zonal wind component in time, ordered with respect to the start of a substorm, shows that the zonal motion reverses, in the mean, approximately one hour after the substorm begins. A similar result is obtained when the observed zonal motions are corrected for the tidal contribution. In contrast, the response of the thermosphere to auroral heating appears to be longer, but is not measureable with the present data.

These principal results are summarized in Table 6.2 together with the observed wind speeds for each component. The importance of ion-drag as a means of accelerating the pre-midnight auroral thermosphere has recently been observationally established (Meriwether et al., 1973). This study extends the recognition of this importance to all hours of the night. Observations of the meridional wind component and its causes have not been discussed in the literature.

The nature of the wind field in the polar-cap thermosphere has emerged as an important problem as a result of this study. The large scale over-the-pole wind field predicted by Fedder and Banks (1972) does not appear to be a dominant feature of the polar-cap winds because such winds should penetrate well into the auroral zone and be seen as a strong equatorward meridional component peaking at or before midnight. Additionally, in the early evening hours a strong (400 to 600 m sec^{-1}) eastward zonal wind should be observed while in the pre-dawn hours strong westward zonal wind should be observed. Such behavior is not

TABLE 6.2

PRINCIPAL RESULTS OF THIS STUDY

WIND COMPONENT	PRIMARY DRIVING FORCE	MAGNITUDE OF WINDS PRODUCED	SECONDARY DRIVING FORCE	MAGNITUDE OF WINDS PRODUCED
MERIDIONAL	PRESSURE GRADIENTS GENERATED BY GLOBAL HEATING	150 M/SEC† (PEAK)	PRESSURE GRADIENTS†† GENERATED BY AURORAL HEATING	UP TO 150 M/SEC
ZONAL	ION-DRAG††† DUE TO NORTH-SOUTH ELECTRIC FIELDS	UP TO 400 M/SEC	PRESSURE GRADIENTS GENERATED BY GLOBAL HEATING	UP TO 150 M/SEC

† MEASUREMENTS REPORTED HERE ARE CONSISTENT WITH PUBLISHED TIDAL MODELS WITH AMPLITUDE HALVED

†† MEASUREMENTS REPORTED HERE ARE CONSISTENT WITH A RESPONSE TIME OF SEVERAL HOURS

††† MEASUREMENTS REPORTED HERE ARE CONSISTENT WITH A TIME CONSTANT OF APPROXIMATELY 1 1/2 HOURS

apparent in the auroral-zone observations examined in this study, nor in the few polar-cap barium measurements which have been reported. Two of these three barium measurements indicate neutral motions, at altitudes up to 270 km, which have a larger component of motion in the direction perpendicular to the ion motion than in the direction of ion motion. This larger, perpendicular, component cannot have been generated by solar-heating pressure-gradients as the tidal winds predicted for the time of these measurements are approximately aligned with the ion motion. It appears then, that a non-tidal pressure-gradient force must be present in the polar cap which dominates the ion-drag force at the times of these barium measurements. These two groups of observations suggest that ion-drag is normally not the dominant force driving polar-cap neutral winds, contrary to the suggestion of Fedder and Banks.

In order to reduce the magnitude of the ion-drag force in the polar cap, either the ion-neutral collision frequency must be small or the average dawn-to-dusk electric field must be small (<5 mv m^{-1}). This latter possibility is unlikely considering the large number of satellite measurements of the electric field reporting polar-cap field strengths in excess of 20 mv m^{-1} (see discussion in Chapter 2). Reduction of the collision frequency can be obtained if the ion density or the neutral density is reduced in the polar cap (relative to the auroral zone). Considering the morphology of particle precipitation, it is very likely that the polar-cap ion density is generally smaller than that in the auroral zone. Thus the observed reduction of the

relative importance of the ion-drag force in the polar cap is expected. However, for the times of the 6300A interferometric measurements, the average F-region peak electron density measured at Resolute Bay was large (although only half that assumed by Fedder and Banks). Thus, if the electron density in the whole polar cap was as large as that reported for Resolute Bay, a basic discrepancy arises. How can the ion-drag force be relatively unimportant in situations when the F-region electron density is large? The resolution of this discrepancy probably lies in lower polar-cap electron densities than obtained from the Resolute Bay ionospheric soundings. However, the existence of a non-tidal pressure-gradient in the polar cap is clearly demonstrated in the barium measurements. The pressure-gradient force is directed away from the auroral zone (as best as can be determined from the present data) and therefore opposes the ion-drag driven winds proposed by Fedder and Banks. Such a pressure-gradient may well be generated by auroral heating. Plainly, more measurements of neutral winds in the polar cap are needed to determine the relative importance of ion-drag and pressure-gradient forces there. These measurements should be made with companion measurements of the electron density profile and electric fields.

A number of other important questions are raised by the pattern of auroral zone winds which has been developed in this study. Some of these questions are:

1. How is the equation of mass continuity satisfied? Zonally there is a net divergence of mass from the midnight sector of the auroral

zone. Is this divergence made up by vertical motions from below or from equatorward mass transport from the polar cap, or both?

2. What is the latitudinal extent of the zonal and meridional winds reported here? (Undoubtedly, this extent depends upon the magnitude of the Joule dissipation of the auroral electrojets and the extent of the auroral electric fields).
3. What are the characteristics of the dayside auroral thermospheric wind field?

It is necessary to continue to make auroral zone measurements of thermospheric winds, particularly continuous measurements such as are provided by 6300A interferometry, to improve the statistical basis of the knowledge of the wind field. These measurements should be accompanied by simultaneous measurements at other latitudes to determine the extent of the winds and the magnitudes of gradients. Such data are now completely lacking, excepting the two simultaneous groups of barium releases discussed earlier. More accurate modelling of the wind field requires these data.

The recently developed technique allowing tracking of a lithium trail in full daylight is suggested as a means of investigating the properties of the dayside wind field. Considering the relative importance of ion-drag, dayside wind measurements should be supported with electric field measurements. It may be possible in the near future to track barium releases, both ions and neutrals, by the same technique used for the lithium observations. Alternatively, the electric field could be measured by radar techniques. The

characteristics of the dayside thermospheric wind field should be investigated, if for no other reason than as a test of the models. It is likely that dayside winds are affected by geomagnetic activity, although not necessarily to the same degree as the nightside because of the reduced electric field strength. Simultaneous dayside and nightside measurements are also highly desirable to isolate the longitudinal extent and the relative importance of changing thermospheric densities.

In conclusion, it has been demonstrated that significant changes in the thermospheric wind field at high latitudes are associated with geomagnetic activity. This new understanding has led, as is usually the case, to further questions. The means of answering these questions are available. Perhaps in the near future, we shall have a complete understanding of a subject area which did not exist 25 years ago.

APPENDIX A

LIST OF SYMBOLS

$\vec{B}$ magnetic induction vector

c speed of light

D diffusion coefficient

e charge of the electron

$\vec{E}'$ electric field

$\vec{E}$ externally impressed electric field

$\vec{F}$ mechanical force

$\vec{g}$ gravitational acceleration of the earth

$\vec{H}$ horizontal magnetic perturbation

h_o initial radius (of an expanding spherical release)

$\hat{i}$ unit vector in the x-direction

I intensity of light

$\hat{j}$ unit vector in the y-direction

$\vec{J}$ current density

$\hat{k}$ unit vector in the z-direction

k Boltzmann's constant

k_j energy conversion factor

m_e mass of the electron

m_i ion mass

m_r mass of released particles

n number density

N or N_e electron number density

N_i ion number density (of each species i)

N_n neutral number density

N_r total number of released particles

P pressure

P_e electron partial pressure

P_i ion partial pressure

q_i ionic charge

r radius

R distance to triangulation point

$\vec{S}$ vector in the direction of observation

t time

T neutral temperature

T_e electron temperature

T_i ion temperature

$\vec{U}$ neutral wind velocity

U_{yI} ion-drag winds in the zonal direction

U_{yo} observed zonal winds

U_{yT} tidal wind component in the zonal direction

$\vec{V}$ ion velocity

$\hat{x}$ unit vector (sometimes in northward direction)

$\vec{X}$ position vector

$\hat{y}$ unit vector (sometimes in westward direction)

$\hat{z}$ unit vector (sometime in the vertically upward direction)

α $=\sigma_1 B^2/\rho$ (reciprocal response time of thermosphere to changes in $\vec{E}$)

β $=\sigma_2 B^2/\rho$

$\Delta\vec{B}$ vector magnetic perturbation measured at earth's surface

ΔH horizontal component of $\Delta\vec{B}$ (in direction of the horizontal component of $\vec{B}$ when $\Delta\vec{B} = 0$

ΔD change in terrestrial magnetic field declination

$\overline{\Delta H}$ average horizontal magnetic perturbation over some time interval

θ geographic colatitude (Chapter 2)

θ zenith angle (Appendix C)

λ wavelength

λ_* vacuum wavelength

λ_o wavelength of profile peak

μ coefficient of viscosity

ν_e total electron collision frequency

ν_i total ion collision frequency

ν_{ni} effective collision frequency for momentum transfer, neutrals to ions

ν_{in} effective collision frequency for momentum transfer, ions to neutrals

ν_{ra} collision frequency between released particles and atmospheric constituents

ξ volume emission function

ρ mass density

ρ_e electron mass density

ρ_i ion mass density

σ_1 Pedersen conductivity

σ_2 Hall conductivity

σ_3 $=\sigma_1 + \sigma_2^2/\sigma_1$, Cowling conductivity

$\sigma_\parallel$ parallel conductivity

Σ_H height integrated Hall conductivity

Σ_P height integrated Pedersen conductivity

$\Sigma_\perp$ effective, height integrated, transverse conductivity

ϕ azimuth angle

ω_e electron gyrofrequency

ω_i ion gyrofrequency

$\vec{\Omega}$ angular velocity of the earth's rotation

APPENDIX B

APPROXIMATE LOCATIONS OF STATIONS MENTIONED IN THIS STUDY[†]

STATION	GEOGRAPHIC LATITUDE (°N)	GEOGRAPHIC LONGITUDE (°E)	1965 CORRECTED GEOMAGNETIC LATITUDE (°N)	1965 CORRECTED GEOMAGNETIC LONGITUDE (°E)	UT-LT (hours)
ANCHORAGE, ALASKA	61.20	210.15	60.8	261.3	10
ANDENES, NORWAY	69.30	16.10	66.1	103.1	-1
BARROW, ALASKA	71.60	203.60	69.7	247.0	10
BARTER ISLAND, ALASKA	70.13	216.33	70.7	256.9	10
CAPE PERRY, CANADA	70.70	236.50	75.4	274.5	8
CHATNIKA, ALASKA	65.13	212.50	65.2	260.1	10
COLLEGE, ALASKA	64.87	212.20	64.9	260.3	10
ESTER DOME OBSERVATORY, ALASKA	64.88	211.95	64.9	260.0	10
FORT CHURCHILL, CANADA	58.80	265.80	70.3	325.9	6
FORT YUKON, ALASKA	66.57	214.75	67.1	260.7	10
INUVIK, CANADA	68.35	226.20	71.1	268.4	9
KIRUNA, SWEDEN	67.80	20.40	64.3	104.0	-1
POKER FLAT, ALASKA	65.13	212.50	65.2	260.1	10
RESOLUTE BAY, CANADA	74.70	265.10	84.3	306.0	6

[†] From Berkey (1972) and Boyd (1973)

APPENDIX C

INTERFEROMETER WIND MEASUREMENTS

Radiation from metastable atomic states is used to measure the temperature and bulk velocity in the thermosphere. Several emission lines are available for measurement and this selection permits some degree of height resolution and choice of neutral- or ion-motion. For example, the ^1D and ^1S states of atomic oxygen giving rise to the important aurora and airglow lines at 6300A and 5577A respectively, allow measurements of winds and temperatures in the 150 to 400 km height range and the 90 to 200 km ranges, respectively. The oxygen ion transition at 7319A permits measurement of the ion-drift. While details of excitation and quenching processes differ with the different lines, 6300A provides a good illustration of the details of these processes and their significance to wind measurements. Wind measurements made at 5577A have been reported by Peteherych and Shepherd (1970), but little work has been done in this area. Ion-drift measurements using 7319A radiation supplement other methods of ion-drift measurement (radar techniques).

The ^1D state of atomic oxygen may be excited by a number of processes. In an auroral situation, most ^1D excitation is caused by direct electron excitation by auroral secondary electrons,

$$O(^3P) + e^- \rightarrow O(^1D) + e^- \qquad C.1$$

and by dissociative recombination

$$O_2^+ + e^- \rightarrow O(^3P) + O(^1D). \qquad C.2$$

Additionally, ^1D excitation is possible via absorption in the Schumann-Runge continuum

$$O_2 + h\nu \rightarrow O(^3P) + O(^1D) \qquad C.3$$

which provides an important source at twilight. A discussion of the rate coefficients and cross sections for these processes may be found in papers by Schaeffer et al. (1971, 1972).

No matter the source of the excitation, radiation when emitted is affected by the Doppler effect. That is, a photon emitted in a particular direction is Doppler shifted by an amount proportional to the magnitude of the emitting particle's velocity in the direction of photon emission. The magnitude of the Doppler shift, $\Delta\lambda$, is given approximately by

$$\Delta\lambda/\lambda_* = (\vec{U} \cdot \hat{S})/c \qquad C.4$$

where $\vec{U}$ is the bulk velocity of the oxygen atoms, $\hat{S}$ is the unit vector in the direction of observation, c is the speed of light and λ_* is the vacuum wavelength. For λ_* =6300.23A and $|\vec{U}|$ = 100 m sec^{-1} in the direction of observation, the maximum Doppler shift is $\pm$ 2.1 x 10^{-3}A . A high resolution instrument is therefore necessary. In contrast to this, temperature measurements require less exacting resolution. The emitted line profile as a function of temperature, T (°K), may be expressed as

$$I(\lambda) = I_o \exp\left\{\frac{-mc^2}{2kT}\left(\frac{\lambda-\lambda_o}{\lambda_o}\right)^2\right\} \qquad C.5$$

where I_o is the peak line intensity at wavelength λ_o (Breene, 1964). The half intensity points are reached at

$$|\lambda-\lambda_o| = \frac{\lambda_o}{c}\sqrt{\frac{2KT\ln 2}{m}} \qquad C.6$$

For atomic oxygen (m = 16 AMU) at 400°K the full width at half maximum of the profile is 2.3 x 10^{-2}A, a much easier resolving task. For this reason temperature measurements have long been possible, but wind measurements have become feasible only recently. As can be seen in equation

C.6, the profile width is proportional to $T^{\frac{1}{2}}$. Temperature measurements rely upon the Doppler effect, as it is the thermal speed distribution which is actually reflected by the line profile. The line profile is expressed as a function of temperature as a matter of convenience. Expected bulk speeds (winds) are usually considerably less than thermal speeds in the thermosphere.

In order that the observed line spectrum accurately reflect temperatures and the Doppler shift reflect winds, it is necessary that the motions of the emitting atoms be representative of the atmospheric temperature and bulk velocity. This can be assured if any kinetic energy resulting from the excitation process can be removed prior to radiation. This thermalization is accomplished by elastic collisions with other neutral constituents of the atmosphere. These collisions are effective in distributing kinetic energy amongst the colliding partners so only a few such collisions are necessary within the radiative lifetime of the atom. Since the neutral-neutral collision frequency is large (approximately 1/2 sec^{-1} at 300 km) relative to the radiative lifetime ($\sim$110 sec) this condition is easily met.

A Fabry-Perot interferometer is normally employed for these Doppler measurements because of its great optical throughput and spectral resolution. With present-day instrumentation and adequate care, neutral wind speed measurements to within 10 m sec^{-1} are possible (Hays, 1972). Measurements of winds and temperatures are possible wherever there is sufficient intensity to permit a line profile to be obtained. A few tens of rayleighs are sufficient, but require considerable integration times (>600 sec). Shorter integrations may be employed with higher intensities.

There are height limits of the atmospheric emission at 6300A due to the long lifetime of the ^1D state and the excitation processes. The lower height limit is set by the quenching reaction

$$O(^1D) + N_2 \rightarrow O(^3P) + N_2^* \qquad C.7$$

in which the N_2 molecule acquires vibrational excitation at the expense of the excitation of the oxygen atom. This quenching is illustrated in Figure C.1, where both the excitation and emission rate profiles from a recent calculation by Rees (1970) are presented. The computations shown are for the polar-cap region where soft precipitating electrons predominate in $O(^1D)$ production. A companion calculation for the harder primary spectrum occurring in the auroral oval gives a similar profile although smaller photon emission rates at all altitudes. Excitation sources used in these calculations were direct electronic excitation (equation C.1) and dissociative recombination (equation C.2). At upper heights the emission profile is controlled by both excitation and the oxygen number density. The implications for interferometer wind measurements at 6300A are straight-forward:

1. only winds above 160 km are measurable and,
2. the observed Doppler shift must be related to a mean of the actual wind profile weighted by the 6300A photon emission rate profile.

If the 6300A volume emission is written analytically as $\xi(z)$ photons m^{-3} sec^{-1}, then the observed line profile as a function of wavelength is given by

$$I(\lambda) = \int_{path} \delta[\lambda, \lambda_*(1 + \frac{\vec{U}(z)\cdot\hat{S}}{c})] \, \xi(z) dS \, , \qquad C.8$$

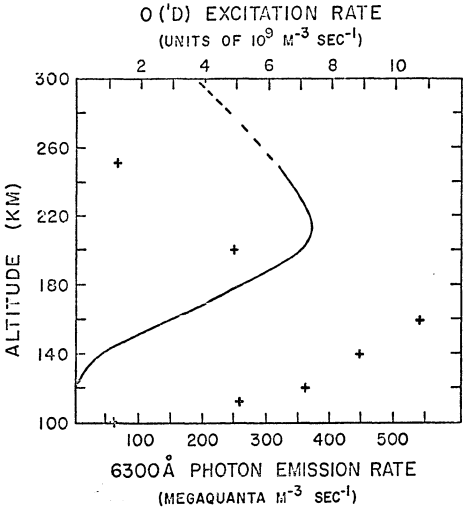

Figure C.1 Theoretical profiles of 6300Å emission (solid curve) and O('D) excitation (crosses). After Rees (1970).

where dS is an increment of length along the line of observation in vector direction $\vec{S}$, and $\vec{U}(z) = \vec{U}$ (Scosθ)is the wind vector at height z, θ being the zenith angle of observation. This equation is only valid for the case where both ξ and $\vec{U}$ are independent of the horizontal coordinates x and y. It has been assumed in deriving this equation that the temperature is zero, so the thermal broadening is ignored.

It is clear that a dominant wind component (in the direction of observation) must be present over a significant portion of the emission height range for a Doppler shift to be measured in the line profile. A randomly oriented wind field contributes only to a broadening of the profile. Since thermal speeds are larger than wind speeds, broadening due to random winds is slight. This broadening can only be interpreted as an increase in temperature. The exact ratio of Doppler shifted emission due to an ordered wind field to that emission from a random wind field at other heights, which permits the ordered winds to be measured, must depend upon the temperature profile of the emitting atoms and the instrumental resolution and noise. Such a detailed analysis is not necessary here, it being sufficient to note that a dominant wind vector must be present in order to measure a Doppler shift.

Without assuming a knowledge of the wind field, it is not possible to use equation C.8 to predict the observed Doppler shifts beyond what has been done earlier in this section. Another difficult problem arises in that ξ is normally a function of the horizontal coordinates in the auroral zone. Since horizontal wind measurements require θ to be nonzero, evaluation of an extended integral of the type given in equation requires $\xi = \xi(x,y,z)$ to be known. However, in the auroral zone, the morphology of 6300A emission (i.e., ξ) is not well understood (Romick

and Belon, 1964). A few general statements, however can be made. Shepherd (1973) observes a zone of diffuse emission at 6300A, wider than the auroral oval and generally parallel to it, to be a regular feature at high latitudes. Superimposed upon this diffuse emission are arc-like emission regions which are generally much broader than normal auroral arcs. These tend to occur on the poleward side of the oval where softer electrons precipitate, but are observed at other places. The relative intensities of the diffuse and arc-like features may vary from night to night. Occasionally, when the diffuse glow is weak and a single arc-like emission region is discernable, it may be possible to measure both winds and temperatures with some degree of height resolution. However, extreme care must be exercised in these cases, and the diffuse background contribution to the profile must be carefully estimated. Normally emission is seen from a wide range of altitudes above 160 km, and therefore a dominant wind component must be present for wind measurements.

The small magnitude of the Doppler shift of the profile due to a dominant wind requires observationally that some means of measuring absolute wavelength be provided in making wind measurements. This is not required in temperature measurements because it is the width of the profile, and not an absolute wavelength, from which temperature is derived. To measure winds, the Doppler shift of the profile peak must be determined with respect to the vacuum wavelength of the line. Two means have been used to do this. The interferometer may be made to view a suitable atomic discharge lamp, temporarily, and scan the profile of a line which is near the wavelength of the 6300A line. Alternatively, a line source may be introduced optically so that it is scanned at the same time as

the 6300A line. The first method allows a smaller free spectral range because, in the second, the reference line must not overlap the 6300A line. Both methods sacrifice observing time in order to provide this wavelength reference. The reference line can be at any wavelength provided that the line will pass through the optics, that it is stable in its wavelength, and that the difference in wavelength between the reference source and the unshifted 6300A line is known. Other, less acceptable, means have been employed which substitute for a reference wavelength. One is the measurement of the Doppler shifts at the same zenith angle, but at azimuths differing by 180 degrees (Armstrong, 1969). The measurement of the relative Doppler shift between the two line profiles is then twice the true Doppler shift, provided that wind gradients over long horizontal distances do not exist. The second method uses the line profile obtained at the zenith as a reference under the assumption of no vertical winds. Little is known of vertical winds, but magnitudes up to 10 m sec^{-1} are predicted for auroral situations (Heaps, 1972). Until more study is given to vertical winds, this referencing technique must be regarded with suspicion. Use of a wavelength reference is preferable to the latter two techniques.

Hays and Roble (1971b) have analysed, in depth, the instrumental effects of the Fabry-Perot interferometer system upon the line profile. It is possible using their work to deconvolve the instrument profile from the measured profile even at low light levels and in the presence of a background continuum. For temperature measurements both their theoretical and numerical error analyses support a 40°K standard deviation for a 1000°K temperature source at airglow intensity limits. The standard deviation of temperature measurement is approximately linear with temperature, and

is about 5°K for an absolute zero source. Although the analysis does not proceed by actual measurement of the width of the profile, temperature uncertainty 40°K at 1000°K source temperature and airglow light levels can be shown, by application of equation C.6, to be equivalent to a 2% change in the profile width. Applying this technique to wind measurements for an airglow situation implies that Doppler shifts of the order of 20 m sec^{-1} will be observable. Since the standard deviation decreases with increasing light level, even smaller uncertainties are to be expected for auroral measurements.

APPENDIX D

RELEASE TECHNIQUES

A number of materials are released into the thermosphere which produce an identifiable change in the atmosphere, usually a change in luminosity, and which can be tracked optically or by some other means, such as radar. Velocity measurements are made by determining the position of the released material by triangulation from several sites at two or more known times. The division of the displacement by the time interval and the direction of motion then define the vector motion. Usually measurement of time presents little difficulty, but positional measurements (triangulation) are more complex and do effect the accuracies of the measured velocities. Detailed examination of triangulation techniques is presented in Appendix E.

Two release modes have been employed: a rapid release of material which produces essentially a point deposition, and a slow release which produces a long trail of material along the trajectory of the carrier rocket. In most cases a chemical reaction is used to produce the desired atom or molecule and simultaneously provide the energy required to force this material from the rocket. An exception to this is trimethyl aluminum, $Al(CH_3)_3$, which is expelled as a liquid from a pressurized cylinder and burns to produce the desired material, aluminum oxide (AlO), at the release altitude. At night a TMA trail may be observed because this burning is chemiluminescent. In twilight, resonance fluorescent scattering of solar photons is dominant. Another material, nitric oxide (NO), a gas, is sometimes released to determine the atomic oxygen density profile and winds in the lower thermosphere by the chemiluminescent reaction

$$NO + O \rightarrow NO_2^* \quad . \qquad D.1$$

In general, most release techniques require the primary chemical reaction to take place inside a cannister which may or may not be ejected from the rocket. A most frequently used reaction is the thermite class of reactions which are generally violently exothermic. Barium releases are made using this class of reaction, but because the reaction proceeds as

$$Ba + CuO \rightarrow BaO + Cu + 96.6 \text{ kcal/mole}, \qquad D.2$$

excess Ba must be added to an initial balanced chemical mixture. Only the excess barium is free to form a neutral barium cloud. When initiated in a specially designed vessel on a rocket, this reaction produces considerable heat, causing expulsion of finely divided or atomic sized reaction products into the atmosphere. Sodium (Na), barium (Ba), strontium (Sr), and lithium (Li) are examples of elements which are frequently released in this manner. Choice of reacting materials does influence the speed of the reaction so that point or trail releases are generally both possible.

The elements and compounds mentioned above all have the property that they will resonantly scatter solar radiation in the visible spectrum. These materials have large photon absorption cross sections and can therefore be seen and photographed at twilight. Observationally, Na and Sr are not ionized to any significant extent by solar ultraviolet radiation. Barium is slowly ionized by a two-step process (Haser, 1967), resulting in both atoms and ions, which is the basis of its usage for measurements of electric fields. Barium ions also have resonance transitions in the visible part of the spectrum. Lithium probably is not ionized.

Released materials, of atomic or molecular sizes, rapidly take up the motion of the thermospheric neutrals (less than two seconds below

200 km altitude). These materials initally have the velocity of the carrier rocket and are slowed down by collisions with atmospheric constituents such that the rocket's motion is not normally seen in photographs of releases. In addition, other larger particles are produced in barium releases which travel along the rocket trajectory for considerable distances. The upper picture of Figure D.1 shows ion, neutral and toroidal (large particle) clouds of a release from Poker Flat Range approximately one minute after release time. The lower photograph shows the structured, late time, development of a large ion cloud.

There are three ways in which observation of release materials may be lost, aside from obscuration. Usually observation is lost due to diffusion away from the release point, which results in densities below a threshold of observability, a threshold set by background illumination, or instrumental sensitivity, or both. For a spherical release the number density n(r,t) as a function of radius and time can be approximated by

$$n(r,t) = \frac{N_r}{\pi^{3/2}(h_o^2 + 4Dt)^{3/2}} \exp\left\{\frac{-r^2}{h_o^2 + 4Dt}\right\} \qquad D.3$$

where N_r is the total number of released particle, h_o is some initial radius (for t=0) and D is the diffusion coefficient (Lloyd and Golomb, 1967). The same authors show that D may be approximately

$$D = KT/m_r \nu_{ra} \qquad D.4$$

where m_r is the mass of the release particles and ν_{ra} is their collision frequency with atmospheric constituents. Thus the larger the mass of the released particles, the smaller D becomes. This mass dependence is especially important for high altitude releases where ν_{ra} is small. Large atomic (molecular) weight materials should be chosen for wind

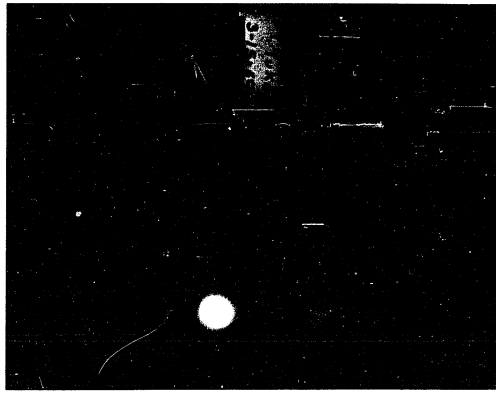

SECEDE III Barium release FIR
from Ft. Yukon, Alaska at T + 4 min. 20 sec. (15051020Z March 1969)

Bob Bumpas

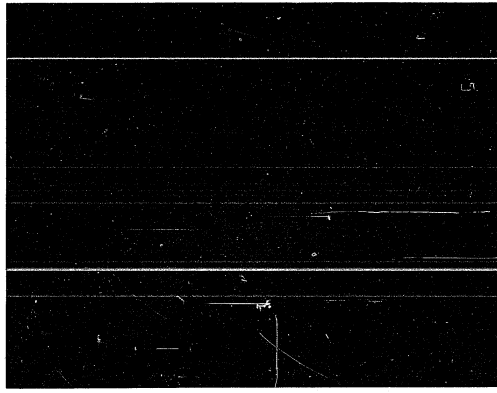

SECEDE III Barium release HEMLOCK
from Bettles, Alaska at T + 26 min. 40 sec. (20060340Z March 1969)

Figure D.1

Merritt Helfferich

measurements above 250 km. Even with barium (m_t =137 AMU.), Wescott et al. (1970) report useful observation times of only five minutes above 300 km. At lower altitudes, 100-220 km, lighter mass materials may be used allowing numerically greater numbers of particles to be released for the same payload mass. Therefore, the planned release altitudes must be taken into account in choosing the material to be released. However, the purposes for which the release is to be made are of overriding concern in this choice. For wind measurements, the choice of barium is well justified on the basis of diffusion alone.

Released materials may also be lost through ionization and by chemical reaction with atmospheric constituents, usually oxygen. While these processes may result in loss of a released material, they may also produce a desirable material. Barium is an example of this, as ionization produces a cloud of barium ions whose motion reflects the presence of electric fields and oxidation produces barium oxide (BaO). In an actual barium release, atomic barium is lost rapidly by these two processes. Rosenberg et al. (1968) report measurements of the time constant for Ba loss at 330 km of 28 sec. The oxidized barium and the BaO resulting from the thermite reaction are usually referred to as the barium neutral cloud. This barium oxide cloud forms a resevoir from which atomic barium is continually created by photodissociation

$$Ba\ O + h\nu \rightarrow Ba + O. \qquad D.5$$

This barium may be returned to the oxide form or it may be ionized. Those atoms which are ionized are then subject to the Lorentz force, although for a shorter period of time than the initally produced ions. Consequently

a trail (or bridge) of ions may link the ion cloud to the neutral cloud as a result of these processes. A bridge fitting this description can be seen in Figure D.1.

APPENDIX E

TRIANGULATION ERRORS

All wind measurements by chemical release require a method for position determination in order to determine velocities. The positional information is usually derived from measurements of the azimuth and elevation angles of selected "points" on the release cloud from two or more stations. Errors inherent in this analysis are only briefly mentioned, or are not discussed at all, in the literature. Since errors must be considered in the analysis of wind measurements, the triangulation technique and possible triangulation errors will be briefly reviewed here.

Consider a point release of some material, which is assumed to remain a point for the duration of measurement. If the position of the material can be determined to be $\vec{X}_1$, at time t_1, and $\vec{X}_2$, at time t_2, then the velocity of the release material is simply given by

$$\vec{U} = \frac{(\vec{X}_2 - \vec{X}_1)}{(t_2 - t_1)} \quad . \qquad \text{E.1}$$

Velocity determination therefore reduces to the problem of finding the position of the release at two points in time. This is done by triangulating the position of the release from two stations. Details of the triangulation method for a point release are reported by La Point et al. (1970). In summary, the observed angles of the release (elevation and azimuth) from two stations are used to compute the position of the release $\vec{X}(t)$. The method also allows calculation of a parameter giving the radius of a sphere in which the release is probably located. This parameter is related to the uncertainty of angle measurement.

Before examining the positional uncertainty of a real (finite) release,

the limiting accuracy for a true point release should be examined. To do this, the principal methods of angle measurement must be examined. Frequently, the procedure used is to scale the point of release in x,y coordinates from the photograph, together with the coordinates of a number of stars. The actual positions of these same stars are calculated from their emphemeris coordinates for the time at which the plate was made. These calculated coordinates are then used to calibrate the plate so that the x,y position of the release may be related to zenith and azimuth angles. If there is image distortion in the plate (usually most pronounced near the edges) at the position of the release, then sufficient stars must be used to correct for this distortion (Wescott et al., 1970). In this way the coordinates of a point can be measured to within an uncertainty of $\pm$ 0.01° when a large format plate with a 30 to 40° field of view is used. The other principally used technique employs a low light level television system, mounted upon an accurately levelled mount, as a pointing device. When the point release is seen in the center of the television frame, the coordinates of the release may be read from shaft encoders to $\pm$ 0.1°. Occasionally, release coordinates must be read from an all-sky camera picture. In such cases, a point can be determined (using the star field to calibrate the frame, and correct for distortion) to better than $\pm$ 1/2° at the zenith and better than $\pm$ 1° at the outer limits of the field of view. For comparison, $\pm$ 1° is assumed. These scaling techniques result in the radius of the error sphere being approximately 6 km using the all-sky camera data, 600 m using the TV pointing system, and 60 m using star plate analysis.

When the actual dimensions of a real release are considered, other errors appear. Consider first a small spherical release, which remains spherical as it grows by diffusion. No longer is there a single point upon which to triangulate so that analysis must be focussed upon the observed outer boundaries of the release, which at first are constantly moving outward. The detection of the outer edge of such a release depends critically upon some detection threshold, which may be different at any two observing sites during twilight. At night, when there is no background luminosity, the detection threshold is set by the instrumental sensitivity. In twilight, background luminosity varies spatially and temporally, increasing the signal to noise ratio. In principle it is possible to remove the twilight sky background by subtraction, so this difficulty will not be discussed further, except to note that an additional uncertainty will be introduced. This uncertainty can only be determined at the time of the analysis taking into account the actual light and noise levels present.

A typical situation is shown in Figure E.1 in plan view. It is obvious that the lines of observation from both stations, the basis of the triangulation measurements and which are individually tangent to the cloud, do not in general intersect at the boundary of the cloud. Furthermore, the lines of observation to opposite sides of the cloud are not tangent to the cloud on a diameter. Two means of determining the position of the cloud are suggested by inspection of this figure.

A. The four lines of observation, two from each station, to each side of the cloud are individually tangent to the surface of the cloud (provided the apparent cloud has the same radius for each station).

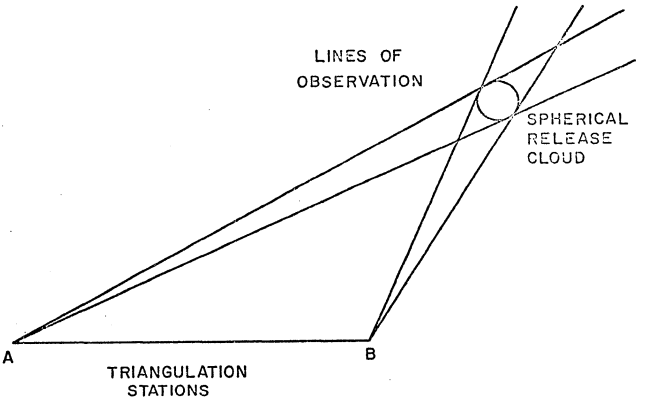

Figure E.1 Typical triangulation situation for a finite spherical release. The release need not necessarily be in the vertical plane of the triangulation stations.

This suggests fitting an arbitrary sphere, which requires four parameters for its definition (3 position parameters and a radius). A system of twelve parametric equations of the lines of observation and one equation for an arbitrary sphere may be written, in which eight unknowns appear. These unknowns are the four parameters specifying the sphere and the four unknown distances from the observing stations to the points of tangency. The equations are not linearly independent. No solution of this type has been reported.

B. Since the cloud is symmetric, a line midway between the lines of tangency at greatest apparent, azimuthal, extent (limbs) should pass nearby the center of the release. It is this condition which is most frequently used to triangulate upon a cloud center. The limb obervations are used to compute the positions of the limbs, from which a center position may be calculated. Alternatively the limb observations may be used to calculate "centered" look angles and the triangulation performed on these angles. These methods are preferable to simple scaling of a supposed center on the basis of visual inspection. In a variation of the above technique, a vertical line is chosen through the release on the basis of several limb scalings at different elevation angles. Points are chosen uniformly along this line (the same number for each station) and triangulation performed for each. A least squares line is fitted to these triangulated points and the midpoint chosen as the best estimate of the actual center. This procedure results in uncertainties from one to a few km (Wescott et al., 1969).

It is not sufficient to simply triangulate on one limb of the release alone. At early times the apparent limb to cloud center distance increases due to diffusion, while at late times the limb contracts back toward the center, now displaced, of the release. The exact temporal dependence of the radius at which the density drops to a critical detection value can be predicted using equation D.3. Use of one limb only for position determination will yield consistently low (or high depending on the limb selected) velocities until the critical density surface begins to contract, after which the velocities will be consistently high (low). Thus it is necessary to determine the motion of the center of the release and one of the above techniques is used. Positional uncertainties of at least 1 km result for cloud-observer distances of 250 to 300 km.

Unfortunately most releases do not retain their initial spherical shape. Indeed the vertical density gradient of the atmosphere is such that downward diffusion is inhibited relative to upward diffusion so that the bottom of the release becomes flattened. Ignoring this minor deformation, the presence of wind shears will also distort a spherical release into an ellipsoidal shape. A comparatively simple example of this is shown in Figure E.2. A spherical release depicted in Figure E.2a is subjected to a linear vertical shear of the horizontal wind shown in Figure E.2b. After a finite time (t) material at points indicated in Figure E.2a will be displaced proportionally to the wind speed at the same height. Corresponding letters of Figures E.2a and E.2c indicate the displacement relative to the center of the release. This distortion is time-dependent such that as time increases, the elongation becomes more pronounced. A

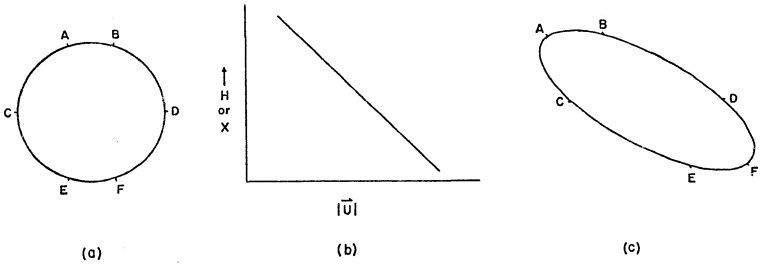

Figure E.2 Schematic temporal development of an initially spherical barium neutral cloud to an ellipsoidal shape by a wind shear. The spherical cloud (a) is acted upon by the sheared wind field (b) to produce the ellipsoidal cloud (c). As time progresses the ellipsoidal cloud becomes more elongated.

horizontal gradient which is linear with distance will produce a similar result. More complex wind fields can produce a considerably more complex neutral cloud structure. A good example of this elongation is shown in Figure E.3 which is from a 40 kgm release of barium at Poker Flat, Alaska. The center of the cloud apparently moved with a speed of 165 m sec^{-1} at 325° azimuth (true while the total cloud length increased at an average rate of 140 m sec^{-1} along 291° azimuth.

The effect of distortion is to increase positional uncertainties, even if the distortion is allowed for in the analysis. This problem has not been discussed in the literature. Quite often distortion of this nature is small and barely discernible in photographic images, but it can be substantial as shown in Figure E.3. The presence of elongation implies that a gradient exists in the wind field. Differentiation between horizontal and vertical gradients can be made if the release is situated appropriately with respect to the triangulation stations. In the case of a vertical gradient, a station located nearly normal to the direction of elongation will be able to detect a substantial tilt to the cloud. In the case of a pure horizontal gradient no such tilt is detectable. To separate combined horizontal and vertical gradient effects requires care be taken in triangulation.

It is important to note that elongation may be directed along any azimuth. If the elongation direction is approximately along a line to the observing station then little distortion will be apparent. Elongation is most easily identified and triangulation most easily accomplished when a release is approximately 45° zenith angle from each of three stations uniformly distributed in azimuth. When only two stations are used and

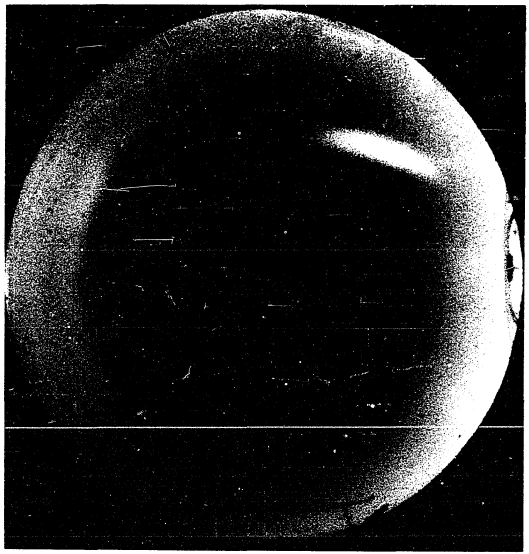

Figure E.3 Neutral barium cloud at late time illustrating exceptional shear. Release is the same as shown in the upper portion of Figure D.1.

the release is distant (a few times the station separation) from the stations, it is impossible to measure the elongation. The release may appear to be nearly circular and the position of the triangulated center is displaced up to a distance equal to one half the elongation towards the triangulation stations. If this were the case for the release shown in Figure E.3, then very substantial velocity errors would have been made. This type of analysis has only been reported once (Romick and Davis, 1971).

A quite different problem arises in the analysis of trail releases because of poor height resolution due to a lack of identifiable structure along the trail. Often, above 120 km, a trail release appears to be smooth. Early workers reprojected their data onto scale models for measurement (Manring et al., 1959; Jarrett et al., 1963). More recently, a technique has been employed in which the expected shape of the trail is computed for each station using an estimated velocity profile (Bedinger, 1972). Discrepancies between the computed trail image and the real image are removed iteratively by adjusting the estimated profile. The adjusted profile is assumed to represent the actual wind velocity profile when all discrepanciesare removed. A new technique interrupts the flow of the released material at short, frequent intervals resulting in a sequence of puffs. Each of these puffs can be individually triangulated (Golomb et al., 1972).

REFERENCES

Aggson, T. L., Probe measurements of electric fields in space, Atmospheric Emissions (ed.) B. McCormac, Van Nostrand Reinhold Co., New York, 305-316, 1967.

Akasofu, S.-I., The development of the auroral substorm, Planet. Space Sci., 12, 273-282, 1964.

Akasofu, S.-I., Polar and Magnetospheric Substorms, D. Reidel Pub. Co., Dordrecht, Holland, 1968.

Anger, C. D. and A. T. Y. Lui, Observations of 5577A and 3914A auroral emissions with the ISIS-2 scanning auroral photometer, presented at the Fall Annual Meeting, American Geophysical Union, San Francisco, December, 1972.

Armstrong, E. B., Doppler shifts in the wavelength of the OI λ6300A line in the night airglow, Planet. Space Sci., 17, 957-974, 1969.

Axford, W. I. and C. O. Hines, A unifying theory of high-latitude geophysical phenomena and geomagnetic storms, Can. J. Phys., 39, 1433-1464, 1961.

Bailey, G. J., R. J. Moffett and H. R. Rishbeth, Solution of the coupled ion and neutral air equations of the mid-latitude ionosphere F_2 layer, J. Atmos. Terr. Phys., 31, 253-270, 1969.

Bates, D. R., A suggestion regarding the use of rockets to vary the amount of atmospheric sodium, J. Geophys. Res., 55, 347-349, 1950.

Bedinger, J. F., Compendium of wind data from the vapor trail technique, GCA Technical Report 66-7-N, March, 1966.

Bedinger, J. F., Measurement of winds above 200 km, J. Geophys. Res., 75, 683-685, 1970.

Bedinger, J. F., Private communication to G. J. Romick, 1971.

Bedinger, J. F., Private communication to G. J. Romick, 1972.

Bedinger, J. F., S. N. Ghosh and E. R. Manring, Emission sodium ejected from rockets, Threshold of Space (ed) E. Zelikoff, Pergamon Press, London, 225-231, 1957.

Berkey, F. T., A Study of the Auroral Absorption Substorm, Ph.D. Dissertation, University of Alaska, Fairbanks, Alaska, 1972.

Berko, F. W., R. A. Hoffman, R. K. Burton and R. K. Holzer, Simultaneous particle and field observations of field-aligned currents, Goddard Space Flight Center Preprint X-646-73-45, 1973.

Bostrom, R., A model of the auroral electrojets, J. Geophys. Res., 69, 4983-4999, 1964.

Boyd, J. S., Private communication, 1973.

Boyd, J. S., A. E. Belon and G. J. Romick, Latitude and time variations in precipitated electron energy infered from measurements of auroral heights, J. Geophys. Res., 76, 7694-7700, 1971.

Breene, R. G., Line width, Handbuch der Physik (ed.) S. Flugge, Band XXVII, Springer-Verlag, Berlin, 1964.

Bryant, D. A., G. M. Courtier, G. Skovli, H. R. Lindalen, K. Aarsnes and K. Maseide, Electron density and electron flux in a glow aurora, J. Atmos. Terr. Phys., 32, 1695-1704, 1970.

Bryant, D. A., G. M. Courtier and G. Bennett, Electron intensities over two auroral arcs, Planet. Space Sci., 21, 165-177, 1973.

Cauffman, D. P. and D. A. Gurnett, Double probe measurements of convection electric fields with the Injun-5 satellite, J. Geophys. Res., 76, 6014-6027, 1971.

Challinor, R. A., The apparent rotation of the upper atmosphere, Planet. Space Sci., 16, 557-566, 1968.

Challinor, R. A., Neutral winds in the ionospheric F-region for an asymmetric global pressure system, Planet. Space Sci., 17, 1097-1106, 1969.

Challinor, R. A., Neutral-air winds in the ionospheric F-region for an asymmetric global pressure system, Planet. Space Sci, 18, 1485-1488, 1970a.

Challinor, R. A., The bahaviour of the arctic F-region in winter, J. Atmos. Terr. Phys., 32, 1959-1965, 1970b.

Chamberlain, J. W., Physics of the Aurora and Airglow, Academic Press, New York, 1961.

Chapman, S. and J. Bartels, Geomagnetism, Clarendon Press, Oxford, 1940.

Choy, L. W., W. Potter, P. Kintner and L. J. Cahill, Field-aligned particle currents near an auroral arc, J. Geophys. Res., 76, 8279-8298, 1971.

Cole, K. D., Electrodynamic heating and movement of the thermosphere, Planet. Space Sci., 19, 59-75, 1971.

Dalgarno, A., Corpuscular radiation in the upper atmosphere, Ann. Geophys., 20, 65-74, 1964.

Dalgarno, A. and F. J. Smith, The thermal conductivity and viscosity of atomic oxygen, Planet. Space Sci., 9, 1-2, 1962.

Davis, T. N. and D. D. Wallis, Observations of ionospheric motions using barium ion clouds, Space Res., 12, 935-949, 1972.

Deehr, C. S., A. Egeland and F. Soraas, Auroral morphology, The Radiating

Atmosphere, (ed.) B. McCormac, D. Reidel Pub. Co., Dordrecht, Holland, 125-149, 1971.

Deehr, C. S., R. J. Davidson and A. Egeland, Particle and auroral observations from the ESRO I / Aurorae satellite, ESRO Scientific Report SR-20, 1972.

DeVries, L. L., Analysis and interpretation of density data from the low-g accelerometer calibration system (logacs), Space Res , 12, 777-789, 1972.

Doupnik, J. R., P. M. Banks, M. J. Baron, C. L. Rino and J. Petriceks, Direct measurement of plasma drift velocities at high magnetic latitudes, J. Geophys. Res., 77, 4268-4271, 1972.

Duncan, R. A., Neutral winds and universal time control of the polar F-region, J. Atmos. Terr. Phys., 31, 1008-1009, 1969.

Eather, R. H., Auroral proton precipitation and hydrogen emissions, Rev. Geophys., 5, 207-285, 1967.

Edwards, H. D., J. F. Bedinger and E. R. Manring, Emission from a sodium cloud artificially produced by means of a rocket, The Airglow and Aurorae, (ed.) E. B. Armstrong and A. Dalgarno, Pergamon Press, London, 122-134, 1955.

Fedder, J. A. and P. M. Banks, Convection electric fields and polar thermospheric winds, J. Geophys. Res., 77, 2328-2340, 1972.

Feldstein, Y. I. and G. V. Starkov, Dynamics of the auroral belt and polar magnetic disturbances, Planet. Space Sci., 15, 209-229, 1967.

Feldstein, Y. I. and G. V. Starkov, Auroral oval planetary dynamics, J. Atmos. Terr. Phys., 33, 197-203, 1971.

Foppl, H., G. Haerendel, J. Loidl, R. Lust, F. Melzner, B. Meyer, H. Neuss, and E. Rieger, Preliminary experiments for the study of the interplanetary medium by the release of metal vapour in the upper atmosphere, Planet. Space Sci., 13, 95-114, 1965.

Frank. L. A. and D. A. Gurnett, Distributions of plasma and electric fields over the polar caps, J. Geophys. Res., 76, 6829-6846, 1971.

Geisler, J. E., Atmospheric winds in the middle latitude F-region, J. Atmos. Terr. Phys., 28, 703-720, 1966.

Geisler, J. E., A numerical study of the wind system in the middle thermosphere, J. Atmos. Terr. Phys., 29, 1469-1482, 1967.

Groves, G. V., Upper atmospheric wind studies by skylark rocket, Nature, 187, 1001-1002, 1960.

Golomb, D., D. F. Kitrosser and R. H. Johnson, Thermospheric structure over Churchill and Hawaii from chemical releases, Space Res., 12, 733-741, 1972.

Gurnett, D. A. and L. A. Frank, Observed relationships between electric fields and auroral particle precipitation, J. Geophys. Res., 78, 145-170, 1973.

Gustafsson, G., On the orientation of auroral arcs, Planet. Space Sci., 15, 277-294, 1967.

Haerendel, F., Electric fields and their effects in the ionosphere, Solar Terrestrial Physics/1969 Part IV, (ed.) Dyer, D Reidel Pub. Co., Dordrecht, Holland, 87-116, 1970.

Haerendel, G. and R. Lust, Electric fields in the ionosphere and

magnetosphere, Particle and Fields in the Magnetosphere, (ed.) B. McCormac, D. Reidel Pub. Co., Dordrecht, Holland, 213-228, 1970.

Haerendel, G., P. C. Hedgecock and S.-I. Akasofu, Evidence for magnetic field aligned currents during the substorms of March 18, 1969, J. Geophys. Res., 76, 2382-2395, 1971.

Hakura, Y., Tables and maps of geomagnetic coordinates corrected by the higher order spherical harmonic terms, Rep. Ionosph. Space Res. Japan, 19, 121-157, 1965.

Hanna, P. B. and C. D. Anger, Auroral colour variations, Planet. Space Sci., 19, 399-412, 1971.

Hanson, W. B., Structure of the ionosphere, Satellite Environment Handbook, (ed.) F. S. Johnson, Stanford University Press, Stanford, California 23-52, 1965.

Harang, L., The mean field of disturbance of polar geomagnetic storms, Terr. Mag. and Atmos. Elec., 51, 353-380, 1946.

Haser, L., Use of barium clouds to study magnetic and electric fields in the atmosphere, Aurora and Airglow, (ed.) B. McCormac, Reinhold Pub. Co., New York, 391-403, 1966.

Hays, P. B., Private communication, 1972.

Hays, P. B. and R. G. Roble, Direct observations of thermospheric winds during geomagnetic storms, J. Geophys. Res., 76, 5316-5321, 1971a.

Hays, P. B. and R. G. Roble, A technique for recovering Doppler line profiles from Fabry-perot interferometer fringes of very low intensity, Appl. Opt., 10, 193-200, 1971b.

Hays, P. B., R. A. Jones and M. H. Rees, Auroral heating and the composition of the neutral thermosphere, Planet. Space Sci., 21, 559-574, 1973.

Heaps, M. G., Circulation in the High Latitude Thermosphere due to Electric Fields and Joule Heating, Ph.D. Dissertation, Utah State University, Logan, Utah, 1972.

Heppner, J. P., A Study of Relationships Between the Aurora Borealis and the Geomagnetic Disturbance Caused by Electric Currents in the Ionosphere, Ph.D. Dissertation, California Institute of Technology, Pasadena, California, 1954.

Heppner, J. P., Magnetospheric convection patterns infered from high latitude activity, Atmospheric Emissions, (ed.) B. McCormac, Van Nostrand Reinhold, New York, 251-266, 1969.

Heppner, J. P., The Harang Discontinuity in the auroral belt ionospheric current, Geofys. Publik., 29, 105-120, 1972a.

Heppner, J. P., Electric field variations during substorms: OGO-6 measurements, Planet. Space Sci., 20, 1475-1498, 1972b.

Heppner, J. P., Polar cap electric field distributions related to the interplanetary magnetic field direction, J. Geophys. Res., 77, 4877-4887, 1972c.

Heppner, J. P., J. D. Stolarik and E. M. Wescott, Electric field measurements and the identification of currents causing magnetic disturbances in the polar cap, J. Geophys. Res., 76, 6028-6053, 1971a.

Heppner, J. P., J. D. Stolarik and E. M. Wescott, Field aligned continuity of the Hall current electrojets and other consequences

of density gradients in the auroral ionosphere, The Radiating Atmosphere, (ed.) B. McCormac, D. Reidel Pub. Co., Dordrecht, Holland, 407-426, 1971b.

Hines, C. O., Internal atmospheric gravity waves at ionospheric heights, Can. J. Phys., 38, 1441-1481, 1960.

Jacchia, L. G. and J. Slowey, The shape and location of the diurnal bulge in the upper atmosphere, Space Res., 7, 1077-1090, 1967.

Jarrett, A. H., G. J. McGratten and J.A. Rees, The measurement of high altitude wind velocities from vapour releases I- projector method, Planet. Space Sci., 11, 309-310, 1963.

Kamide, Y., Private communication, 1973.

Kato, S., Horizontal winds systems in the ionospheric E-region deduced from the dynamo theory of the Sq variation Part II, rotating earth, J. Geomagn. Geoelectr., 8, 24-37, 1956.

Kato, S., Horizontal wind systems in the ionospheric E-region deduced from the dynamo theory of the geomagnetic Sq variation Part IV, J. Geomagn. Geoelectr., 9, 107-115, 1957.

King-Hele, D. G., The rotational speed of the upper atmosphere determined from changes in satellite orbits, Planet. Space Sci., 12, 835-853, 1964.

King-Hele, D. G. and R. R. Allen, The rotational speed of the upper atmosphere, Space Sci. Rev., 6, 248-272, 1966.

Kisabeth, J. L. and G. Rostoker, Current flow in auroral loops and surges from ground based magnetic observations, J. Geophys. Res., in press.

Kockanski, A., Atmospheric motions from sodium cloud drifts, J. Geophys. Res., 69, 3651-3662, 1964.

Kockanski, A., Atmospheric motions from sodium cloud drifts at four locations, Mon. Wea. Rev., 94, 199-212, 1966.

Kohl, H. and J. W. King, Atmospheric winds between 100 and 700 km and their effects on the ionosphere, J. Atmos, Terr. Phys., 29, 1045-1062, 1967.

Kohl, H. Wind systems in the thermosphere, Space Res., 10, 550-560, 1970.

LaPoint. G. C., S. P. Geller, and T. N. Davis, TV-Track: a real time output system for object tracking, Rome Air Development Center Report, RADC-TR-70-273, November, 1970.

Leadabrand, R. L., M. J Baron, J. Petriceks and H. F. Bates, Chatanika, Alaska, Auroral-Zone Incoherent-Scatter Facility, Radio Sci., 7, 747-756, 1972.

Lincoln, J. V., Geomagnetic indices, Physics of Geomagnetic Phenomena, (ed.) S. Matsushita and W. H. Campbell, Academic Press, New York, 67-100, 1967.

Lincoln, J. V., Geomagnetic and solar data, J. Geophys. Res., 77, 2413, 3003, 3630, 4280, 1972.

Lloyd, K. H. and D. Golomb, Observations on the release of a cloud of barium atoms and ions in the upper atmosphere, AFCRL Environmental Research Paper, AFCRL-67-0144, 1967.

Maggs, J. E. and T. N. Davis, Measurements of the thickness of auroral structures, Planet. Space Sci., 16, 205-209, 1968.

Manring, E. R., J. F. Badinger and H. B. Pettit, Some wind determinations

in the upper atmosphere using artificially generated sodium clouds, J. Geophys. Res., 64, 587-591, 1959.

Maynard, N. C., Electric fields in the ionosphere and magnetosphere, Magnetosphere-Ionosphere Interactions, (ed.) K. Folkestad, Universitetsforlaget, Oslo, 155-169, 1972.

Mendillo, M. and M. D. Papagiannis, Estimate of the dependence of the magnetospheric electric field on the velocity of the solar wind, J. Geophys. Res., 76, 6939-6943, 1971.

Meriwether, J. W., Private communication, 1973.

Meriwether J. W., J. D. Stolarik, J. P. Heppner and E. M. Wescott, Neutral wind data from barium releases in high latitudes, presented at the 52nd Annual Meeting of the American Geophysical Union, Washington, D. C., April, 1971.

Meriwether, J. W., J. P. Heppner, J. D. Stolarik and E. M. Wescott, Neutral winds above 200 km at high latitudes, J. Geophys Res., in press.

O'Brien, B. J. and C. D. Laughlin, An extremely intense electron flux at 1000 km altitude in the auroral zone, J. Geophys. Res., 67, 2667-2672, 1962.

O'Brien, B. J. and H. Taylor, High-latitude geophysical studies with Injun 3- part 4, auroras and their excitation, J. Geophys. Res., 69, 45-63, 1964.

Olsen, H. C., A Study of Electric Fields and Related Phenomena from Observations of Barium Cloud Motions, M.Sc. Thesis, University of Alaska, Fairbanks, 1970.

Omholt, A., Studies on the excitation of aurora borealis II the forbidden lines of oxygen, Geofys. Publik., 21, 1-38, 1959.

Park, R. J. and P. A. Cloutier, Rocket-based measurement of Birkland durrents related to an auroral arc and electrojet, J. Geophys. Res., 76, 7714-7733, 1971.

Peteherych, S. and G. G. Shepherd, Interferometer measurements of daytime aurora and airglow, presented at the 52nd Annual Meeting of the American Geophysical Union, Washington, D. C., April 1971.

Piddington, J. H., The motions of ionized gas in combined magnetic, electric and mechanical fields of force, Monthly Notices of the Royal Astronom. Soc., 114, 651-663, 1954.

Potter, W. E., Rocket measurements of auroral electric and magnetic fields, J. Geophys. Res., 75, 5415-5432, 1970.

Ragsdale, G. C. and P. E. Wasko, Wind flow in the 80-400 km altitude region, NASA report TN D- 1573, March, 1963.

Rees, D., Ionospheric winds in the auroral zone, J. Brit. Interplanet. Soc., 24, 233-246, 1971.

Rees, M. H., Auroral ionization and excitation by incident energetic electrons, Planet. Space Sci., 11, 1209-1218, 1963.

Rees, M. H., Conjugate effects of atmospherically scattered auroral particles, Radio Sci., 3, 645-649, 1968.

Rees, M. H., Auroral electrons, Space Sci. Rev., 10, 413-441, 1969.

Rees, M. H., Effects of low energy electron precipitation on the upper atmosphere, The Polar Ionosphere and Magnetospheric Processes, (ed.) G. Skovli, Gordon and Breach Science Pub. Inc., New York, 137-149, 1970.

Rees, M. H. and J. C. G. Walker, Ion and electron heating by auroral electric fields, Ann. Geophys., 24, 193-199, 1968.

Richmond, A. D., Generation of winds in the auroral zone, presented at the 54th Annual Meeting of the American Geophysical Union, Washington, D. C. April, 1973.

Rieger, E., Measurement of electric fields in equatorial and medium latitudes during twilight using barium clouds, Max-Planck Institute Report MPI/PAE EXTRATERR 49/70, September, 1970.

Rishbeth, H., Thermospheric winds and the F-region: a review, J. Atmos. Terr. Phys., 34, 1-47, 1972.

Roble, R. G., A Theoretical and Experimental Study of the Stable Mid-latitude Red Arc, Ph.D. Dissertation, University of Michigan, 1969.

Roble, R. G. and R. E. Dickinson, Atmospheric response to heating within a stable auroral red arc, Planet. Space Sci., 18, 1489-1498, 1970.

Romick G. J. and A. E. Belon, The Determination of the Spatial Distribution of Auroral Luminosity, Geophysical Institute, University of Alaska, Report UAG-149, May, 1964.

Romick, G. J. and R. D. Sharp, Simultaneous measurements of an incident hydrogen flux and the resulting hydrogen Balmer alpha emission in an auroral arc, J. Geophys. Res., 72, 4791-4801, 1967.

Romick, G. J. and T. N. Davis, Neutral winds near 170 km in the auroral zone from analysis of barium release data, presented at the 52nd Annual Meeting of the American Geophysical Union, Washington, D. C., April, 1971.

Rosenberg, N. W., G. T. Best, F. P. Delgreco, M. M. Klein, M. A. McCleod, T. M. Noel and W. K. Vickery, AFCRL barium release studies, 1967, Project Secede Special Report #4, (ed.) S. Leonard, Stanford Research Institute, January, 1968.

Rostoker, G., Polar magnetic substorms, Rev. Geophys. Space Phys., 10, 157-211, 1972a.

Rostoker, G., Geomagnetic indices, Rev. Geophys. Space Res., 10, 935-950, 1972b.

Rostoker, G. and J. L. Kisabeth, The response of the polar electrojets in the evening sector to polar magnetic substorms, University of Alberta, Killum Earth Sciences Report #35, 1972.

Schaeffer, R. C., P. D. Feldman and W. G. Fastie, Photodissociative excitation of O('D) atoms in the day airglow, J. Geophys. Res., 76, 3168-3173, 1971.

Schaeffer, R. C., P. D. Feldman and E. C. Zipf, The dayglow [OI] λλ 6300A and 5577A lines in the early morning ionosphere, John Hopkins University Report #35, 1972.

Schlichting, H., Boundary Layer Theory, McGraw-Hill Book Co. Inc., New York, 6th edition, 1968.

Sharp, R. D., R. G. Johnson, M. F. Shea and G. B. Shook, Satellite measurements of precipitating protons in the auroral zone, J. Geophys. Res., 72, 227-237, 1967.

Sharp, R. D. and R. G. Johnson, Some average properties of auroral electron precipitation as determined from satellite observations, J. Geophys. Res., 73, 969-990, 1968.

Sharp. R. D., D. L. Carr and R. G. Johnson, Satellite observations of the average properties of auroral particle precipitations; latitudinal variations, J. Geophys. Res., 74, 4618-4630, 1969.

Shepherd, G. G., Private communication, 1973.

Silsbee, H. C. and E. H. Vestine, Geomagnetic bays, their occurrence frequency and current systems, Terr. Magn. Atmos. Electr., 47, 195-208, 1942.

Smith, L. B., An observation of strong thermospheric winds during a geomagnetic storm, J. Geophys. Res., 73, 4959-4963, 1968.

Stoffregen, W., H. Derblom, L. Ladell and H. Gunnarsson, The chemistry of artificial clouds in the upper atmosphere and their response to winds and fields, Uppsala Jonosfarobsevatorium Report # 17 Part B, Stockholm, 1971.

Stoffregen, W., Anomaly of the neutral wind at approximately 200 km height at high latitudes, Magnetosphere-Ionosphere Interactions, (ed.) K. Folkestad, Universitetsforlaget, Oslo, 1972.

Sugiura, M. and J. P. Heppner, The earth's magnetic field, Introduction to Space Science, (ed.) W. M. Hess, Gordon and Breach Sci. Pub., New York, 1-92, 1965.

Sugiura, M. and D. J. Poros, Provisional hourly values of equatorial Dst for January to June 1972, Goddard Space Flight Center preprint X-645-72-355, 1972.

Swift, D. W., Effective height-integrated conductivity of the ionosphere, J. Geophys. Res., 77, 1279-1285, 1972.

Swift, D. W., Direct comparison between satellite measurements of the electric field and the visual aurora, presented at the 54th Annual Meeting of the American Geophysical Union, Washington, D. C., April, 1973.

Taeusch, D. R., G. R. Caringnan and C. A. Reber, Neutral composition variation above 400 km during a magnetic storm, J. Geophys. Res., 76, 8318-8325, 1971.

Tarpley, J. D., The ionospheric wind dynamo, II Solar tides, Planet. Space Sci., 18, 1091-1103, 1970.

Townshend, J. B., Preliminary geomagnetic data from the College observatory [for the months of January, February, March, and April, 1972], NOAA/ERL, College, 1972.

Vest, R., A Three Dimensional Model of the Thermosphere with Auroral Heating, Ph.D. Dissertation, and Scientific Report # 412, Pennsylvania State University, 1973.

Walker, J. C. G. and M. H. Rees, Ionospheric electron densities and temperatures in aurora, Planet. Space Sci., 16, 459-475, 1968.

Watkins, B. J., H. F. Bates, A. E. Belon and R. D. Hunsucker, Electron density variations at Chatanika, Alaska, during the storm of August 04-09, 1972, World Data Center A, for Solar-Terrestrial Physics, Report UAG-28 Part II. Collected Data Reports on August 1972 Solar-Terrestrial Events, (ed.) H. E. Coffey, U. S. Department of Commerce, National Oceanic and Atmospheric Administration, 1973.

Watt, T. M., Incoherent scatter observations of the ionosphere over Chatanika, Alaska, J. Geophys. Res., 78, 2992-3006.

Wescott, E. M., J. D. Stolarik and J. P. Heppner, Electric fields in the vicinity of auroral forms from motions of barium vapor releases, J. Geophys. Res., 74, 3469-3487, 1969.

Wescott, E. M., J. D. Stolarik and J. P. Heppner, Auroral and polar cap electric fields from barium releases, Particles and Fields in the Magnetosphere, (ed.) B. McCormac, D. Reidel Pub. Co., Dordrecht, Holland, 229-239, 1970.

Whalen, B. A., J. R. Miller and I. B. McDiarmid, Energetic particle measurements in pulsating aurora, J. Geophys. Res., 76, 978-986, 1971.

Whalen, J. A., Auroral oval plotter and nomograph for determining corrected geomagnetic local time, latitude and longitude for high latitudes in the northern hemisphere, AFCRL Environmental Research Paper # 327 (AFCRL-70-0422), 1970.

Whitten, R. C., and I. G. Poppoff, Fundamentals of Aeronomy, John Wiley and Sons, New York, 1971.

Wiens, R. H. and A. Vallance Jones, Studies of auroral hydrogen emissions in West-Central Canada- III proton and electron auroral oval, Can. J. Phys., 47, 1493-1503, 1969.

Wu, S. T., S. C. Chang and R. E. Smith, Transient movement and Joule heating in the thermosphere, presented at the 54th Annual Meeting of the American Geophysical Union, Washington, D. C., April, 1973.

REFERENCE IS ALSO MADE TO

Canadian Ionospheric Data, Resolute Bay [for months of January, February, March, and April, 1972], Department of Communications, Ottawa, 1972.

COSPAR International Reference Atmosphere, North Holland Pub. Co., Amsterdam, 1965.

International Auroral Atlas, Edinburgh University Press, Edinburgh, 1963.